2015

Rotating Space Elevators: Classical and Statistical Mechanics

Steven Knudsen

Recommended Citation

Knudsen, Steven, "Rotating Space Elevators: Classical and Statistical Mechanics" (2015). *Graduate Theses, Dissertations, and Problem Reports*. 5995.
https://researchrepository.wvu.edu/etd/5995

Rotating Space Elevators:
Classical and Statistical Mechanics

Steven Knudsen

Dissertation submitted to the
Eberly College of Arts and Sciences
at West Virginia University
in partial fulfillment of the requirements
for the degree of

Doctor of Philosophy
in
Physics

Leonardo Golubovic, Ph.D., Chair
Earl Scime, Ph.D.
Wathiq Abdul-Razzaq, Ph.D.
Harry Gingold, Ph.D.
Daniel J. Pisano, Ph.D.
Loren Anderson, Ph.D.

Department of Physics and Astronomy

Morgantown, West Virginia
2015

Keywords: Space Elevator, Inertial Forces, Classical Mechanics, Statistical Physics, Space Travel, Nonlinear Dynamics, Instabilities and Transitions, Chaos

ABSTRACT

Rotating Space Elevators

Steven Knudsen

We investigate a novel and unique dynamical system, the Rotating Space Elevator (RSE). The RSE is a multiply rotating system of strings reaching beyond the Earth geo-synchronous satellite orbit. Objects sliding along the RSE string ("climbers") do *not* require internal engines or propulsion to be transported far away from the Earth's surface. The RSE thus solves a major problem in the space elevator technology which is how to supply the energy to the climbers moving along the string. The RSE is a *double* rotating floppy string. The RSE can be made in various shapes that are stabilized by an approximate equilibrium between the gravitational and inertial forces acting in the double rotating frame. The RSE exhibits a variety of interesting dynamical phenomena studied in this thesis.

Curriculum Vitae

STEVEN R. KNUDSEN

EDUCATION

Ph.D.	Physics, West Virginia University, Spring 2015 (expected)
M.S.	Physics, University of Maryland, 1990
B.S.	Physics, Wheaton College, IL, 1986

ACADEMIC EXPERIENCE

2006-present	Ph.D. Candidate, West Virginia University, Theoretical Physics: *Classical and Statistical Mechanics of Rotating Space Elevators,* Supervisor: Prof. Leonardo Golubović
2001-2006	Research Assistant, West Virginia University, Theoretical Condensed Matter Physics*: Molecular Dynamics Simulations of Solids Under External Stresses,* Supervisor: Prof. Martina Bachlechner
1988-1990	M.S. student; M.S. Thesis: *Decadal Variations of Heat Flux in the North Atlantic Ocean,* University of Maryland, Supervisor: Prof. James Carton
1988-1990	Teaching/Research Assistant, University of Maryland
1982-1986	Undergraduate student, Physics Major, Wheaton College, IL

PROFESSIONAL EXPERIENCE

2011-present	Senior Scientist, KeyLogic Systems, contracted to DOE/NETL, Morgantown, WV
2010-2011	Senior Analyst, Sextant Technical Services, contracted to DOE/NETL, Morgantown, WV
2007-2009	Instructor of Physics, Waynesburg University, Pennsylvania
2001-2006	(Senior) Member Research Staff, Institute for Scientific Research, Fairmont, WV.

MY RESEARCH INTERESTS AND ACHIEVEMENTS

Condensed Matter Physics: Molecular Dynamics Simulations of Condensed Matter Systems. I have studied solids interfaces under external stresses and interface fracture phenomena. I have described my results in this area in my Publication 1 and in my Conference presentation 1.

Dynamics of Physical Systems: Analytic, Computational, and Numerical Methods: Algorithm development; Large scale numerical simulations; Grid methods for continuum modeling. I have explored the dynamics of Rotating Space Elevators discussed in this thesis. I have described my results in this area in my Publications 2 and 3 and in my Conference presentations 2 through 6.

JOURNAL PUBLICATIONS

1. *"Molecular dynamics simulations of the mechanical strength of Si/ Si_3 N_4 interfaces"*, Martina E. Bachlechner, Jennifer Zhang, Ye Wang, Jarrod Schiffbauer, **Steven R. Knudsen,** Dimitris Korakakis, *Physical Review B* **72**, p. 094115 – 094124 (2005).

2. *"Classical and statistical mechanics of celestial scale spinning strings: Rotating space elevators"*, Leonardo Golubović and **Steven Knudsen**, *Europhysics Letters* **86,** 34001 (2009).

> The journal's scientific editor (Dr. Peter Reiman) selected our paper to be highlighted on the Euro Physics Letters web site, with free access to the paper in 2009. After its publishing in Europhysics Letters, our article on Rotating Space Elevators has been featured on 44 different web sites. In 2010, the paper entered the EPL *"Best of 2009"* Articles Collection featuring "the most popular, innovative and progressive work published in EPL in 2009" (quote from the letter of Dr. Graeme Watt, Executive Editor, EPL).

3. "*Rotating space elevators: Physics of celestial scale spinning strings*", **Steven Knudsen** and Leonardo Golubović, *European Physical Journal Plus* **129**, 242 (2014).
-- 24 pages long journal article

SELECTED Department of Energy PUBLICATIONS

1. *"Sharing Smart Grid Experiences through Performance Feedback"* (DOE/NETL Contract: DE-FE0004001, March 31, 2011), Jesse Goellner, Marija Prica, Joe Miller, Steve Pullins, John Westerman, Jess Harmon, Tom Grabowski, Bruce Renz, **Steven Knudsen**, Deborah Coen, and Chris Wyatt, NETL Publication, http://netl.doe.gov/smartgrid/docs/PFP%20for%20the%20Smart%20Grid_Final_v1.0_031511.pdf
2. *"Electric Power System Asset Optimization"* (DOE/NETL-430/061110, March 7, 2011), Paul Myles, Joe Miller, **Steven Knudsen**, and Tom Grabowski , NETL Publication, http://www.netl.doe.gov/energy-analyses/pubs/ElecAssetOptRep.pdf

NASA PUBLICATION

Canning, Francis, X. and Steven Knudsen, On Whether Angular Momentum in Electric and Magnetic Fields Radiates to Infinity, NASA/CR--2006-214124 (March 2006) http://gltrs.grc.nasa.gov/reports/2006/CR-2006-214124.pdf

CONFERENCE PRESENTATIONS

1. *"Mechanical Strength of Silicon/Silicon Nitride Interfaces: A Molecular-Dynamics Study"*, Martina E. Bachlechner, **Steven R. Knudsen,** Jennifer Zhang, Ye Wang, Jarrod Schiffbauer, Dimitris Korakakis, at the March Meeting of the American Physical Society, Montreal, Canada, March 2004
2. *"Rotating Space Elevator"*, **Steven Knudsen** and Leonardo Golubović, Dynamics Days 2008, conference held in Knoxville, Tennessee, January 2008.
3. *"Rotating Space Elevator: Nonlinear Dynamics and Statistical Physics",* **Steven Knudsen** and Leonardo Golubović, Dynamics days 2009, conference held in San Diego, California, January 2009.
4. *"Rotating Space Elevator: Classical and Statistical Physics of Cosmic Scale Spinning Strings"*, **Steven Knudsen** and Leonardo Golubović, March Meeting of the American Physical Society, Pittsburgh, Pennsylvania, March 2009.
5. *"Rotating Space Elevator: Classical and Statistical Physics of celestial scale Spinning Strings"*, **Steven Knudsen** and Leonardo Golubović, at the Gordon Conference on Nonlinear Science, Mountain Holyoke College, June 2009.
6. "*Rotating space elevators: Nonlinear dynamics of celestial scale spinning strings*", **Steven Knudsen** and Leonardo Golubovic, contributed conference talk given at the Annual Meeting of the Mid-Atlantic Section of the American Physical Society, Penn State University, October 2014.

Acknowledgement

I would like to express my deep gratitude to my advisor Dr. Leonardo Golubovic for providing me with the opportunity to do my research in a fascinating physics area. I am grateful to him for his guidance, patience, inspirations, and productive discussions.

I would like to thank Dr. Earl Scime, Dr. Wathiq Abdul-Razzaq, Dr. Harry Gingold, Dr. Boyd Edwards, Dr. Daniel J. Pisano, and Dr. Loren Anderson for taking time from their busy schedules to serve on my committee. Dr. Pisano in particular has stepped into the void left by Dr. Edwards when he accepted a position at University of Utah. I am grateful to Dr. David Lederman, interim Chair of the Physics and Astronomy Department, for his help in the final stages of this thesis. I thank Dr. Duncan Lorimer for providing me access to his computing cluster, and Julian Dymacek and Nate Garver-Daniels for their help with parallel programing. I enjoyed discussions on non-linear dynamics with Drs. Siegfried Bleher and Mark Koepke.

Finally, thanks to my great parents and my dear wife, for all the courage and happiness they have provided me. Also, thanks are due to my children, who have asked me when the space elevator will finally be built.

This research has been supported in part by WVHTC and NASA through the sub-grant WVHTC-W-NASA-IR-07-1367 of the Grant NNX06AE557: Innovative Research for Next Generation Space Exploration.

Content

Chapter 1 Introduction

Chapter 2 Rotating space elevators (RSE): celestial scale spinning strings

Chapter 3 **Dynamics of a free (untied) RSE**

List of Figures

Chapter 1:

Fig. 1: (a) Geometry of LSE. The coordinate system (R_1, R_2, R_3) rotates together with the Earth around the R_2-axis (not shown) pointing through the north pole N. Indicated is the geo-synchronous (together with the Earth) rotation of the LSE. The LSE bottom is tied to the Earth. Figure (b) depicts “Crank” space elevator which operates as a pulley (“conveyer belt”) used to lift and bring down attached climbers. Note that the Crank is essentially a double-stranded LSE.

Fig. 2: Elliptical version of RSE. The coordinate system (R_1, R_2, R_3) rotates together with the Earth around the R_2-axis (not shown) pointing through the north pole N. Indicated are the internal (nearly around the R_1-axis) and geo-synchronous (together with the Earth) rotations of the RSE. The RSE bottom is tied to the Earth. The RSE top executes only minute displacements $<< R_{earth}$.

Chapter 2:

Fig. 1: In (a), the elliptical RSE with minor semi-axis b= 0.5 Earth radii and major semi-axis a = 3.2107 Earth radii (so its top is about 0.8 Earth radii above the geo-stationary level). In (b), we show the USRSE (attached to a LSE) with T_{RSE} = 4.22 min (discussed in Sec. 2.3). In these figures we include also the equipotentials of the effective potential in Eq. (7). Sliding climbers oscillate between two turning points (indicated by straight arrows) that are on the same equipotential.

Fig. 2: From our simulations, the upper panel: The $R_1(t)$ coordinate of the climber sliding with no friction along the floppy RSE with the (initial) shape in Fig. 1(a) and TRSE=10.83 min. The maximum climber velocity relative to the string has magnitude about 29 km/s while the minimum speed is zero at the turning point. The lower panel: The $R_1(t)$ coordinate of the climber on the floppy RSE with initial shape in Fig. 1(b) with TRSE=4.22 min. See Sec. 2.4 for the analytic explanation of the nearly periodic character of climbers motion. The maximum climber velocity relative to the string is about 8 km/s, while the minimum speed is zero. Note: With a weak sliding friction, climbers would eventually stop near the RSE point minimizing the $U(s) = \Phi_{eff}(\vec{R}(s))$. From the equipotentials of the effective potential labeled in Fig. 1, one can see that this point occurs close to the RSE point maximizing its R_2 coordinate in Fig. 1.

Fig. 3: The upper panel: the magical mass distribution [i.e., line density obtained by Eq. (8)] of the RSE with the shape in Fig. 1(a) and $T_{RSE} = 10.83\,\text{min}$. The lower panel: the magical mass distribution (line density) of the RSE with the shape in Fig. 1(b) and $T_{RSE} = 4.22\ \text{min}$.

Fig 4: From our simulations: For the elliptic RSE in Fig. 1(a), the RSE top coordinates $R_1(t)$ in (a), $R_3(t)$ in (b), and, in (c), the evolution of the RSE angular momentum L_1 about the R_1-axis (in the frame rotating with the Earth), for $T_{RSE} = 10.83\,\text{min}$ and $T_{RSE} = 21.66\,\text{min}$. In (d), the evolution of the RSE profile (of one of its two branches) for $T_{RSE} = 21.66\,\text{min}$ over the first ten days. Here, for any RSE point P, the Y is its distance away from the (instantaneous) axis A connecting the RSE bottom and top, and X is the distance between the normal projection of P onto the axis A and the RSE bottom point (at $X = 0$).

Fig. 5: Evolution of the tension at the midpoint of the elliptic RSE in Fig. 1(a). Upper panel: T_{RSE} = 10.83 min, whence the tension oscillations remain small and the tension remains positive. Lower panel, T_{RSE} = 21.66 min, whence the tension oscillations become huge, and the tension assumes both positive and negative values.

Fig. 6: In (a) and (c), frequency power spectrum $P(f)$ of the RSE top coordinate $R_1(t)$ [f is in units of min^{-1}]. For $T_{RSE} = 10.83\,\text{min}$, $P(f)$ in (c) has a sharp (δ-function like) primary peak corresponding to the periodic-like motion of the RSE top (with a 360 min period) seen in (d). (a) For $T_{RSE} = 21.66\,\text{min}$ the primary peak of $P(f)$ is broad. This corresponds to a larger amplitude chaotic motion of the RSE top seen in (b), and in Fig. 4(a). Even for $T_{RSE} = 10.83\,\text{min}$, the top motion contains a fast chaotic component evidenced by the presence of a finite width secondary peak of $P(f)$ in (c). It's frequency corresponds to the time period of $T_{RSE}/2 \approx 5.4\,\text{min}$. These chaotic oscillations are seen in real time in panel (e) which magnifies panel (d) over a time sub-interval. We also note that the small upward drift of $R_1(t)$ seen over the 4000 min time interval displayed in (d) is actually a reflection of the presence of the slow pendular mode with the period of about 8000 min (see Fig. 7, upper panel) which is twice longer than the time interval displayed in (d).

Fig. 7: Upper panel, R_3 coordinate of the top of the elliptic RSE (with T_{RSE}=10.83min <T_{crit}) exhibiting a slow pendular mode with the period of about 8000 min. Lower panel, R_2 coordinate of the top of the same elliptic RSE exhibiting one day period small oscillations around a small nonzero average value. Thus, the RSE long axis is slightly tilted out of the Earth equatorial plane.

Fig. 8: (a) depicts small oscillations of RSE shape (thick line) about the initial shape (thin line). The RSE is somewhat like an object under a time periodic shear stress, with the period = T_{RSE}. Panel (a) is conceptual and it exaggerates the actual shape fluctuations seen in our simulations in

panels (b)-(d) of the elliptic RSE in Fig. 1(a) with T_{RSE}=10.83 min. The panels display the dynamics of $R_1(t)$ of the RSE point initially at $R_1(0)$=4.193 R_{earth}. The point executes relatively small oscillations with an amplitude smaller than 0.004R_{earth} and the apparent period = T_{RSE}=10.83 min. At early times these oscillations have character of beats with the beat period of about 100 min; see panel (b). At late times the regular pattern of beats de-coheres, yet the main repeat period of about 10 min is still apparent in these seemingly chaotic oscillations; see panel (c). The early-to-late time crossover is clearly visible in panel (d). In (e) we display the power spectrum $P(f)$ obtained from a long time sequence of $R_1(t)$. The dominant peak is indeed at the frequency $f=1/\ T_{RSE}$, however there are numerous weaker peaks seen at other frequencies as well. All the peaks are broad indicating chaotic system dynamics.

Fig. 9: In the upper panel, we plot the USRSE loop shapes obtained for several different values of T_{RSE}, all for the same value of the parameter $\tilde{K}\ = 1/4$. In the lower panel, we plot, versus T_{RSE}, the USRSE speed $\Omega_{RSE}|R_2(s)|_{\max}$ as well as the speed at infinity v_∞ of an object released from a sliding climber at $|R_2(s)|_{\max}$ on the lower branch of USRSE in Fig. 1(b) when this branch is in the plane of our Fig. 1. It is obtained from Eq. (17). The two speeds are given in units of the first cosmic speed v_1.

Appendix A

Fig. A1: Geo-synchronous frame versus double rotating frame (DRF). See the text for the notation used in the figure. Note that the two frames have the common axis 1, whereas the axes 2 and 3 of the DRF rotate relative to the axes 2 and 3 of the geo-synchronous frame.

Appendix B

Fig. B1: Geometry of planar RSE string in Double Rotating Frame.

Appendix D

Fig. D1: The potential $U(s)$ seen by a climber on the elliptic RSE with major semi-axis a =3.2107 R_{earth} and minor semi-axis b= 0.5 R_{earth}. For this RSE, equation (D11) predicts $\Omega_{\min}$= 3.72 v_1/R_{earth} . Upper panel gives the $U(s)$ for Ω_{RSE}= 7.8 v_1/R_{earth}. Right panel gives the $U(s)$ for Ω_{RSE}= 2.8 v_1/R_{earth}.

Chapter 3:

Fig. 1: (a) Elliptical version of RSE. The coordinate system (R_1, R_2, R_3) rotates together with the Earth around the R_2-axis (not shown) pointing through the north pole N. Indicated are the internal (nearly around the R_1-axis) and geo-synchronous (together with the Earth) rotations of the RSE. The RSE bottom is close to the Earth surface but it is *not* tied to it. The RSE top is at the distance D ("gap") above the geostationary satellite orbit (with the radius of 6.6108 Earth radii). In (b), the magical mass line density $\mu(s)$ versus the arc-length distance s from the RSE bottom [obtained by Eq. (8) of Ch. 2] of the elliptic RSE with the shape as in (a) for the RSE period of $T_{RSE} = 7.04\,\text{min}$, minor elliptical semi-axis $b = 0.17$ Earth radii, and the gap $D = 0.1564$ Earth radii. Note that the most of the RSE mass is largely concentrated in the top and bottom regions of the RSE.

Fig. 2: Untied RSE projection onto the equatorial plane (R_1, R_3) of the geosynchronous frame which rotates with the angular velocity Ω_{earth} with respect to the inertial frame (dashed axis). The RSE is conceptualized as an arrow with head being the RSE top and end of tail being the RSE bottom.

Fig. 3: The dynamics of the RSE center of mass in terms of its center of mass coordinates $r_{cm}(t)$ - $r_{cm}(0)$ in (a) and $\theta_{cm}(t)$ in (b), for the gap D=0.1564 Earth radii, $b = 0.16$ Earth radii, $T_{RSE} = 7.04\,\text{min}$. Both quantities exhibit small slow mode oscillations with a period longer than one day [see also Fig. 5]. The $\theta_{cm}(t)$ however also exhibits a slow steady drift. In (c) we plot $\dot{\theta}_{cm}(t)$ which oscillates around a nonzero average value corresponding to the RSE angular velocity (seen in the geosynchronous frame) of the RSE drift along the equator. In (d) we display the slow mode, with 1 day (exact) period, which is visible in the dynamics of the out-of-plane $(R_2)_{\text{cm}}$ coordinate of the RSE center of mass. Note that the out-of-plane RSE coordinates $(R_2)_{\text{cm}}$ oscillates around a nonzero time average reflecting the presence of a small tilt of the RSE out of the equatorial plane.

Fig. 4: In (a) and (c), the dynamics of the angles $\theta(t)$ and $\phi(t)$, for D=0.1564, $b = 0.16$ Earth radii, $T_{RSE} = 7.04\,\text{min}$. They oscillate with nearly the same period of about 79.4 min, as

evidenced by their power spectra in (b) and (d) that both exhibit strong peaks at the same frequency $f \approx 1/79.4\,\mathrm{min}$. Note however the existence of two nearby peaks due to which $\phi(t)$ and $\theta(t)$ exhibit beat like pattern with a repetition time of about 600 min. There are also much faster oscillations (with period of about 3.5min=$T_{\mathrm{RSE}}/2$) due to which the curves in (a) and (c) appear thick. Finally, note that the out-of-plane angle $\phi(t)$ oscillates around a nonzero time average reflecting the presence of a small tilt of the RSE out of the equatorial plane.

Fig. 5: Squared frequency of the slow mode seen in the dynamics of the RSE center of mass coordinates r_{cm} and θ_{cm} (the inset gives the mode time period in days). Here, $b = 0.16$ Earth radii, and $T_{RSE} = 3.52\,\mathrm{min}$. Simulation results are indicated by the stars (connected by the blue line). We also display the corresponding analytic result (black line); see the appendix to this chapter, Eqs. (A22) and (A34), and the slow mode discussions after Eq. (A38). Both the simulations and the analytic result indicate vanishing of the soft mode frequency as the gap D approaches the critical value $D_{hopping} \cong 0.2$ Earth radii.

Fig. 6: The dynamics of the radial distance (from the Earth center) of a sliding climber on the quasi-tied untied RSE with D=0.1564 Earth radii, $b = 0.16$ Earth radii, $T_{RSE} = 7.04\,\mathrm{min}$.

Fig. 7: The dynamics of the RSE center of mass in terms of its center of mass coordinates $r_{cm}(t)$ in (a) and $\theta_{cm}(t)$ in (b), for the hopping RSE with gap $D = 0.3164$ Earth radii, $b = 0.17$ Earth radii, $T_{RSE} = 7.04\,\mathrm{min}$.

Fig. 8: (Part I): Each panel gives a time sequence of RSE bottom and top projections onto the equatorial plane in the *inertial frame*, over the first 6000 min. of time evolution. Length unit used here is 1 Earth radius. In all panels $b = 0.17$ Earth radii, $T_{RSE} = 7.04\,\mathrm{min}$. The Earth is depicted as a small circle. The RSE is conceptualized as an arrow with head being the RSE top and end of tail being the RSE bottom. Displayed is one panel with $D < D_{hopping} \cong 0.2$ Earth radii, when the untied RSE is quasi-tied and nearly follows the Earth rotation. The remaining three panels are for the gaps D in the range between $D_{hopping} \cong 0.2$ and $D_{unbinding} \cong 2.11$ Earth radii when the untied RSE exhibits a hopping motion. In the last example the hopping period is longer than the displayed 6000 min. evolution.

Fig. 9: The ratio *Z(D)* in Eq. (1): the results from our simulations (dots) versus analytic result (solid line) obtained by eq. (A29) of the appendix to this chapter. The simulations are done with $b = 0.17$ Earth radii, $T_{RSE} = 7.04\,\text{min}$.

Fig. 10: Natural log of $\dot{r}_{cm} / v_1 = (dr_{cm} / dt) / v_1$ [with v_1, the first cosmic speed] versus the natural log of time (in days), for various values of the gap D around the unbinding threshold value $D_{unbinding} \cong 2.11$ Earth radii for which case the plot approaches the straight line with the slope -1/3, i.e. $\dot{r}_{cm} \sim t^{-1/3}$. Note that for $D > D_{unbinding} \cong 2.11$ Earth radii, the $\dot{r}_{cm}$ approaches at long times a constant value corresponding to escape velocity at infinity. The simulations are done with $b = 0.17$ Earth radii, $T_{RSE} = 7.04\,\text{min}$.

Appendix to Chapter 3

Fig. A1: (a) Dumbbell in the dynamical equilibrium state in geo-synchronous frame. The coordinate system (R_1, R_2, R_3) rotates together with the Earth around the R_2-axis (not shown) pointing through the north pole N. In (b), the degrees of freedom r_M and θ_M used in the Lagrangian in Eq. (A9). The dashed axis is static in the *inertial frame.*

Fig. A2: (a) Function Z versus $\overline{D} = D / R_E$; see eq. (A29). (b) Slow mode angular frequency (squared) versus $\overline{D} = D / R_E$; see eqs. (A21) and (A30). (c) Case $\overline{D} < \overline{D}_{hopping}$: form of the effective potential eq. (A27) for $\overline{D} = 0.05$. (d) Case $\overline{D}_{hopping} < \overline{D} < \overline{D}_{unbinding}$: form of the effective potential eq. (A27) for $\overline{D} = 0.95$. In all panels, $r_{geo} = 6.6108 R_E$.

Fig. A3: Dumbbell modes: (a) Slow in-equatorial plane mode, best seen in the center of mass coordinates $\theta_{cm}(t) \approx \theta_M(t)$ and $r_{cm}(t) \approx r_M(t)$; see fig. 2. (b) Fast in-equatorial plane mode, best seen in the bottom dynamics or the angle $\theta(t)$; see fig. 2. (c) Slow out-of-equatorial plane mode, best seen in the center of mass R_2 coordinate. (d) Fast out-of-equatorial plane mode, best seen in the bottom R_2 coordinate or the angle $\phi(t)$.

Chapter 1

Introduction

1.1 The conceptual development of the traditional space elevator

Dreams of traveling to the heavens have entranced men since the early times of civilization. The story of the “Tower of Babel” in Genesis 11 of the Bible connects the notion of human cooperation for space travel to “heaven” to the multiplying of human languages, which frustrates the effort. In modern history, the fable “Jack and the Beanstalk,” from 1807 [1], (and a burlesque version named *The Story of Jack Spriggins and the Enchanted Bean* from 1734) presents a young boy whose mother plants foolishly obtained seeds which then grow into a great tower that can even hold a giant! Neither of these stories addresses the physics questions of how the towers can remain upright under compressive and buckling (bending) forces.

It was therefore up to the famous Russian scientist Konstantin Tsiolkovsky in 1895 [2] to integrate the vision of the space elevator with the realities of physics. Tsiolkovsky was considered to be a rocket scientist, and the father of spaceflight and he had spent considerable time thinking about the limitations and alternatives of rocket flight. He was inspired by the Eiffel Tower in Paris to conceptualize a tower that reached from ground zero all the way into deep space, above the geosynchronous satellite orbit. This "celestial castle" would orbit the Earth in a geosynchronous fashion meaning that it would be directly overhead one spot on Earth's surface at all times. An object released at the tower's top would also have the orbital velocity necessary to remain in geosynchronous orbit. Thus, the Tsiolkovsky’s tower can be used to deploy satellites into orbits around the Earth. The centrifugal force acting on the tower due to Earth rotation has an interesting effect: The giant tower is under *tension* rather than compression, and therefore is not subject to the sorts of buckling that limits the height of skyscrapers. In the case of skyscrapers, the centrifugal force is negligible, but for the celestial size objects envisioned by Tsiolkovsky and his followers (both scientists [2-6], and science fiction writers [7,8]), the gravitational force and centrifugal force play equally significant roles. Because the internal force is a tension rather than compression, the space elevator can be a floppy non-rigid object ("string").

It wasn't until 1959 that someone suggested a feasible method for building the space elevator. Another Russian scientist, Yuri N. Artsutanov, conceived a scheme for building a space tower. Artsutanov suggested using a geosynchronous satellite as the base from which to construct the tower [2, 3]. According to Artsutanov, by using a counterweight, a cable would be lowered from geosynchronous orbit to the surface of Earth while the counterweight was extended from the satellite away from Earth, keeping the center of gravity of the cable motionless relative to Earth. Artsutanov published his idea in the Sunday supplement of Komsomolskaya Pravda in 1960. This construction scheme is still the standard as long as deployment is sufficiently slow [2, p. 71].

In 1975, Jerome Pearson [4] brought the idea of the space elevator to the scientific community in the U.S. In his careful and detailed design of a workable space elevator while at the U.S. Air Force Flight Dynamics Laboratory he outlined, mathematically and physically, the implications of a space elevator designed to have the constraint of constant stress (tension/cross sectional area) throughout, while maintaining an external force balance, see our Sec. 1.2. Artsutanov independently proposed the same idea [3]. The two balancing external forces in the earth frame are the centrifugal and gravitational forces. Pearson-Artsutanov constant stress elevator provides a simple way to handle the high tensions present in space elevators: The elevator can be designed for *any* given value of the constant stress, see Sec. 1.2. This value can be chosen to be smaller than the critical breakup stress of the material used. Hence, from the materials science point of view, real space elevators *can* be made. This spurred a lot of recent interest in building space elevators out of novel materials such as carbon nanotubes and diamond nano-threads [2]. Notably, Pearson has continued related work and (with his coworkers) has suggested practical designs for slingshots that can be placed on an artificial lunar mountain [5].

It is very easy to understand the advantages of the space elevator concept over conventional rocket propulsion. With chemical propulsion, a rocket carries its own fuel that it needs to overcome gravitational forces, leading to an intrinsic energy inefficiency. Because of earth's deep gravitational well, the load-to-fuel ratios are typically very small (e.g., $\sim 10^{-2}$ for the Apollo/Saturn V missions to Moon), so that essentially all fuel energy is used to accelerate the fuel itself. On the other side, within the space elevator concept, a spaceship climbs along the elevator by facilitating an internal electrical engine which uses externally supplied electric energy. Since there is no fuel carried by the climber, the supplied energy is 100% used to lift the climber. So, the space elevator concept is immensely more energy efficient than the rocket propulsion.

The problem however remains on how to externally supply the energy to the climber. Naively, one may think of running an electrical transmission line along the space elevator, until realizing just how long this structure is compared to transmission lines on earth, so that power losses will be close to 100%. To remedy for this, Edwards [2] proposes that laser power be beamed up the elevator from the ground to the climber. The beam energy would be absorbed by climbers and converted into electrical energy driving their engines.

For any of these schemes climbing is typically slow and it may take several months for the climber to travel along the space elevator from the Earth to the geosynchronous level. During such a long climb, the useful load (including possibly humans) would be exposed for a very long time to the dangerous cosmic radiation, which is especially strong in this range of altitudes above the Earth. To solve the problem of radiation bands near the equator, which can poison humans climbing into space, Gassend has proposed [6] space elevators that are not attached at the equator. Their purpose is to allow payloads to miss the dangerous cosmic radiation. Even without this problem with cosmic rays, typically long travel time itself is certainly not a satisfactory feature of space elevators, especially if a rapid deployment of objects into outer space is desired.

1.2 The Linear Space Elevator: A Mathematical Model

The Space Elevator is a colossal and tantalizing design and engineering project. The linear space elevator (LSE), which is attached to the Earth near the equator and stretches radially outward past the geosynchronous orbit (at 42,164 km away from the Earth's center), is the only design under serious consideration. The Liftport Group (www.liftport.com) and the Spaceward Foundation (www.spaceward.org) are fleshing out the details of such a design, which to stay in orbit must reach out past the geosynchronous level. The properties of materials for building an SE are of paramount importance because of large tension forces acting along SE string. In 2002, Brad Edwards [2] brought Artsutanov's suggestions, together with Pearson's insights and other sources, together to present the space elevator concept in a book, and dealt with the obstacles one by one. The main obstacle is the material strength of the tether, but carbon nanotubes have the theoretical strength necessary for the tapered design of Pearson [4]. With the improving technology of carbon nanotube composite materials, there is expectation that a strong enough material for the space elevator can be manufactured. Space debris continues to be a worrisome prospect, and indeed, some propose to clean debris from space in preparation for larger long-lived structures such as the space elevator.

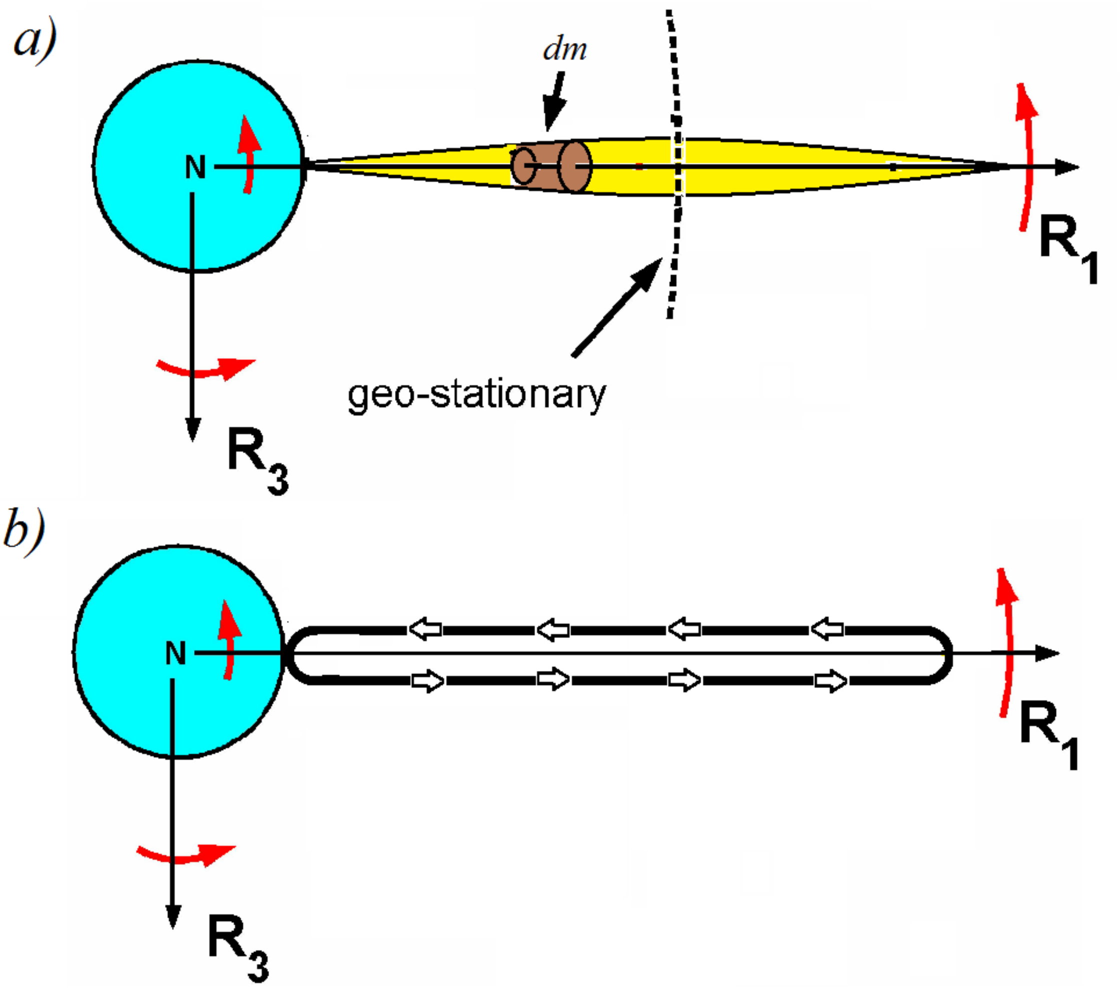

Fig. 1: (a) Geometry of LSE. The coordinate system (R_1, R_2, R_3) rotates together with the Earth around the R_2 -axis (not shown) pointing through the north pole N. Indicated is the geo-synchronous (together with the Earth) rotation of the LSE. The LSE bottom is tied to the Earth. Figure (b) depicts "Crank" space elevator which operates as a pulley ("conveyer belt") used to lift and bring down attached climbers. Note that the Crank is essentially a double-stranded LSE.

In this section we discuss the traditional linear space elevator (LSE), which slings objects into space using the Earth's rotation with the angular velocity Ω_{earth} . We will discuss the LSE in its equilibrium configuration in the frame rotating with the Earth, see Fig. 1(a). The LSE mass element *dm* at the distance R_1 from the Earth center is under influence of the combined gravitational and centrifugal force of the form,

$$dF = dm \;\; a_1(R_1)\,, \tag{1}$$

acting along the R_1 direction in Fig. 1. In Eq. (1),

$$a_1(R_1) = \Omega_{earth}^2 R_1 - \frac{GM_{earth}}{R_1^2}\,. \tag{2}$$

We note that $a_1(R_{geo})=0$ with R_{geo}=42,164 km, the geostationary orbit radius. In Eq. (2),

$$R_1 = R_{earth} + s\,,$$

with *s*, the LSE arc-length measured from its tying point with the Earth, at $R_1=R_{\text{earth}}$ in Fig. 1(a). In equilibrium, the force in Eq. (1) is balanced by the change of the tension force *T(s)* over the length *ds* of the mass element *dm*,

$$0 = dF + dT = dF + \frac{dT}{ds}ds\;\;. \tag{3}$$

By Eq. (1) and (3),

$$\frac{dT}{ds} = -a_1(R_1(s)) \;\; \mu(s)\,, \tag{4}$$

where we introduced the mass line density

$$\mu(s) = \frac{dm}{ds} = \rho \;\; A(s)\,, \tag{5}$$

with ρ, the bulk density of the LSE material and *A(s)*, the local cross-sectional area of the LSE string. By integrating Eq. (6), we find the equation,

$$T(s) = T(-0) - \int_{-0}^{s} ds' \;\; a_1(R_1(s')) \;\; \mu(s')\,, \tag{6}$$

giving the tension field *T(s)* [-0 signifies an arbitrarily small negative quantity, while +0 signifies an arbitrarily small positive quantity]. Physically, the integration constant *T(-0)* in Eq. (6) is the force pulling the LSE at its tying point with the Earth. A realistic LSE can have only a finite length $s_{\max}$. For any $s > s_{\max}$, $\mu(s) = 0$ and *T(s)=0*. Thus, by Eq. (6) with $s=s_{\max}+0$,

$$0 = T(s_{\max}+0) = T(-0) - \int_{-0}^{s_{\max}+0} ds' \;\; a_1(R_1(s')) \;\; \mu(s') \cdot$$

This gives the value of the *T(-0)* in Eq. (6), in the form

$$T(-0) = \int_{-0}^{s_{\max}+0} ds' \;\; a_1(R_1(s')) \;\; \mu(s') \cdot \tag{7}$$

By Eqs. (6) and (7), one easily obtains the LSE tension field,

$$T(s) = \int_{s}^{s_{\max}+0} ds' \;\; a_1(R_1(s')) \;\; \mu(s') \cdot \tag{8}$$

Note that the LSE tension field *T(s)* is entirely determined by the LSE mass distribution $\mu(s)$. For a floppy LSE, the form of $\mu(s)$ must be such that *T(s)* in Eq. (8) is positive for any *s* in the interval $0<s<s_{\max}$.

A significant LSE example is the “dumbbell” model, in which the LSE mass is concentrated in two points, “bottom” and “top”, at *s=0* and $s=s_{max}$, respectively. The bottom and top are assumed to be connected by a massless string. Thus,

$$\mu(s) = m_{bot} \;\; \delta(s) + m_{top} \;\; \delta(s - s_{\max}) \, . \tag{9}$$

For this model, Eqs. (7) and (9) yield,

$$T(-0) = m_{bot} a_1(R_{earth}) + m_{top} a_1(R_{top}) \, , \tag{10}$$

with $R_{\text{top}}=R_{\text{earth}}+s_{\max}$, whereas Eq. (8) yields,

$$T(s) = m_{top} a_1(R_{top}) \, , \tag{11}$$

for any s in the interval $0<s<s_{\max}$. Since $a_1(R_1)>0$ only for $R_1>R_{geo}$, the string tension in Eq. (11) is positive only if $R_{\text{top}}>R_{\text{geo}}$.

An interesting special case is when the pulling force $T(-0)$ is zero. Obviously, such an LSE will remain in equilibrium (stable or unstable) even if the LSE bottom is *untied* from the Earth. The condition $T(-0)=0$ can be realized by special choices of the mass distribution $\mu(s)$ in Eq. (7). For example, for the dumbbell model, by Eq. (10) with $T(-0)=0$, one obtains,

$$0 = m_{bot} a_1(R_{earth}) + m_{top} a_1(R_{top}), \tag{12}$$

indicating that the *untied* dumbbell model will be in equilibrium only if the masses of its bottom and top satisfy the Eq. (12), i.e., by Eq. (2),

$$0 = m_{bot}\left(\Omega_{earth}^2 R_{earth} - \frac{GM_{earth}}{R_{earth}^2}\right) + m_{top}\left(\Omega_{earth}^2 R_{top} - \frac{GM_{earth}}{R_{top}^2}\right). \tag{12'}$$

Eq. (12′) fixes the value of ratio $m_{\text{top}}/m_{\text{bot}}$. Interestingly, by Eq. (12), this ratio *diverges* when R_{top} approaches R_{geo} because in this limit $a_1(R_{\text{top}})$ approaches zero. We also note that this untied dumbbell model can be, under some circumstances, used to discuss our untied rotating space elevator (see our Ch. 3).

Returning to the discussion of LSE with a general form of the mass distribution $\mu(s)$, we note that for engineering purposes the major quantity is the tensile stress ("tensile pressure"), i.e., tension force per unit cross-sectional area of the LSE string,

$$p(s) = \frac{T(s)}{A(s)}. \tag{13}$$

By Eq. (5),

$$p(s) = \rho\, K(s), \tag{14}$$

with

$$K(s) = \frac{T(s)}{\mu(s)} . \tag{15}$$

With the above definition, the Eq. (4) can be expressed also as

$$\frac{d}{ds}[K(s)\ \ \mu(s)] = -a_1(R_1(s))\ \ \mu(s) \cdot \tag{16}$$

Eq. (16) can be easily used to discuss the constant (uniform) stress linear space elevator (USLSE) of Pearson and Artsutanov mentioned in Sec. 1.1. It is designed by assuming a constant $p(s)=p_0$, i.e., constant $K(s)=K_0=p_0/\rho$. For this special case, Eq. (16) reduces to

$$K_0 \frac{d}{ds}[\ln(\mu(s))] = -a_1(R_1(s)) \quad \cdot \tag{17}$$

Equation (17) is easily integrated to find the major result for USLSE,

$$\ln\left(\frac{\mu(s)}{\mu(0)}\right) = \ln\left(\frac{A(s)}{A(0)}\right) = \ln\left(\frac{T(s)}{T(0)}\right) = \frac{\Phi_{eff}(R_1(s)) - \Phi_{eff}(R_{earth})}{K_0} . \tag{18}$$

In Eq. (18), we introduced the effective potential,

$$\Phi_{eff}(R_1) = -\frac{1}{2}\Omega_{earth}^2 R_1^2 \ -\frac{GM_{earth}}{R_1} \tag{19}$$

which generates the $a_1(R_1) = \Omega_{earth}^2 R_1 - \frac{GM_{earth}}{R_1^2}$ via the usual relation $a_1(R_1) = -\frac{\partial \Phi_{eff}}{\partial R_1}$. The USLSE can be realized by tapered cable design, i.e., by using the variable cross-sectional cable area *A(s)* designed according the Eq. (18). By this equation, the *A(s)* exhibits a maximum at the geostationary distance R_{geo} at which $a_1(R_{geo}) = 0$, and the effective potential is at maximum. Simply by choosing the constant stress $p_o << p_{\max}$= the critical breakup stress for the material used, the USLSE can be made out of *any* material by using Eq. (18). However, with very small values of $p_0=\rho K_0$, the equation (18) yields very large values of *A(s)*. Because of this, high $p_{\max}$ materials, with higher permissible values of p_0, are preferred. In view of this, carbon nanotubes have been suggested as promising materials for space elevator design [2]. We stress that LSEs other than USLSE are generally troubled by high values of tensile stresses. In particular, the constant cross-sectional area RSE is not an USLSE and it suffers from large tensile stresses around geostationary height. We note that “crank” LSE (depicted in Fig 1(b)) is essentially a double stranded LSE with constant cross-sectional area. This LSE operates as pulley (Atwood machine) used to lift attached climbers [8].

We end this discussion by noting that the above useful concept of the uniform stress space elevator can be extended to our double rotating space elevators, as discussed in our chapter 2.

1.3 This Thesis subject: Double Rotating Space Elevator (RSE)

- Solution of the climbers energy supply problem

In this Thesis we discuss a novel class of nonlinear dynamical systems, Rotating Space Elevators (RSE). The RSE concept has not been discussed in the literature, with the exception of our study [9] that introduced this concept for the first time. The RSE are multiply rotating systems of strings. Remarkably, useful loads and humans *sliding* along the RSE strings do *not* require internal engines or propulsion to be rapidly transported (sled) into space far away from the Earth's surface. Thus, the RSE concept solves the major problem of energy supply to climbers that troubles the ordinary LSE concept.

The RSE is a *double* rotating floppy string typically having the shape of a loop [9]. Due to its special kind of motion (see below), the RSE becomes pre-tensioned due to gravitational and inertial forces. Due to the tension, the floppy RSE maintains its loopy shape.

The special RSE motion, ensuring the persistence of its shape, is a nearly a geometrical superposition of: (a) geosynchronous (one day period) rotation around the Earth, and (b) yet another rotational motion of the string which is typically much faster (with period ~ tens of minutes) and goes on around a line perpendicular to the Earth at its equator (see Fig. 2).

This second, *internal rotation* plays a very special role: It provides the dynamical stability of the RSE shape and, importantly, it also provides a mechanism for the climbing of objects free to slide along the RSE string.

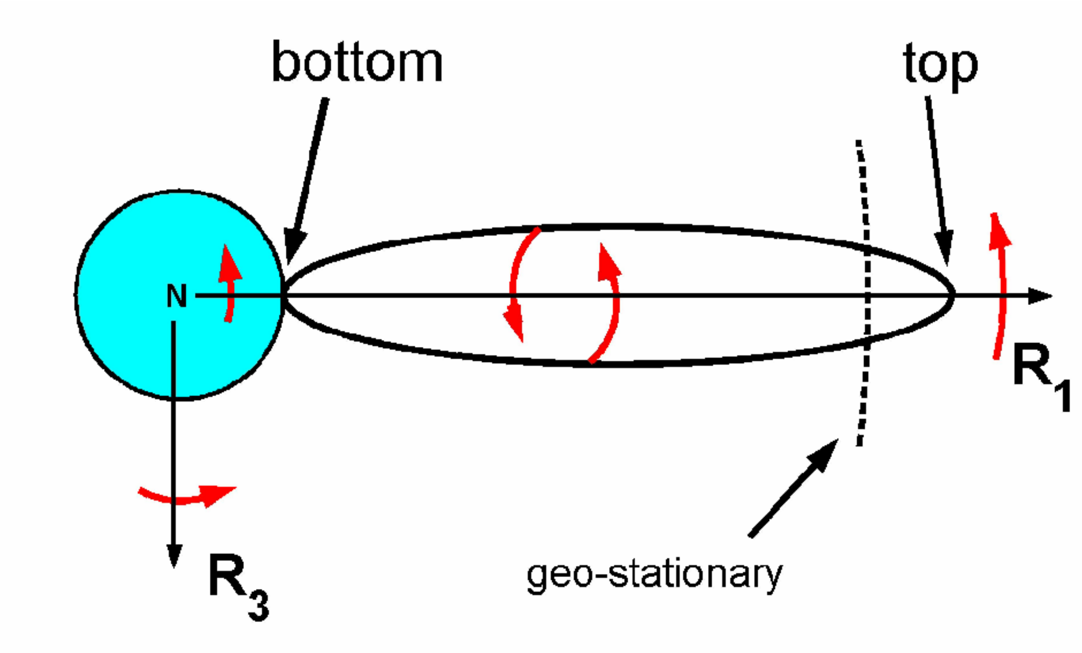

Fig. 2: Elliptical version of RSE. The coordinate system (R_1, R_2, R_3) rotates together with the Earth around the R_2-axis (not shown) pointing through the north pole N. Indicated are the internal (nearly around the R_1-axis) and geo-synchronous (together with the Earth) rotations of the RSE. The RSE bottom is tied to the Earth. The RSE top executes minute but dynamically significant displacements $<< R_{earth}$.

The RSE can be made in various shapes. By a special choice of mass distribution of the RSE cable, the simple double rotating geometrical motion can be made to represent an approximate yet exceedingly accurate solution to the exact equations of the RSE string dynamics. This is corroborated here by numerical simulations showing that, under some conditions, the RSE double rotation motion as well as nearly constant RSE shape both persist *indefinitely* in time.

The elliptical RSE (Fig. 2) exhibits very high tensile stresses at its points near mid-height. Therefore, other shapes will be described whose mass and tension distribution yield a Uniform Stress RSE (USRSE). We will argue in Ch. 2 that the USRSE can be made by using technologically available materials such as carbon nanotubes.

A brief nontechnical overview of this Thesis physics is outlined here. In chapter 2, we introduce the mathematical concept of Rotating Space Elevators. We show that the double rotating motion can be stabilized by a specially chosen (magical) mass distribution, i.e., mass line density $\mu(s)$ of the RSE string. Chapter 2 also contains case studies of tied (to the Earth) elliptical RSEs (ERSE). We find that if the ERSE's internal angular velocity is higher than a critical value, the ERSE maintains nearly constant shape and nearly double-rotating (yet weakly chaotic) motion conceptualized in Fig. 2. On the other side, if the ERSE's internal angular velocity is smaller than the critical value, the ERSE exhibits an interesting morphological transformation: Its motion becomes strongly chaotic, and the ERSE's initially elliptical loop crumples and eventually nearly completely narrows over a few weeks period. All these dynamic behaviors are explored by multi-week RSE dynamics simulations. In chapter 2 we also define the concept of the uniform stress RSE (USRSE) and simulate its dynamics.

We show that both ERSE and USRSE can be used to elevate climbers from the surface of the Earth to remote outer space locations in a simple way; see Ch. 2. The climbers do not need any internal engine to execute their motion. Rather, they *spontaneously* slide along the RSE string from the Earth to outer space locations. This unusual climber sliding motion is facilitated by the inertial force (centrifugal force) acting on climbers due to the RSE's internal rotation. In chapter 2 we also describe possible use of RSE to launch satellites and interplanetary spaceships.

Next we ask the question what will happen if one *unties* the ERSE in Fig. 2 from the Earth. This interesting question is investigated in chapter 3. Interestingly, we find that, under some conditions, the tying may not be needed at all to achieve the stable double rotating motion of ERSE. In fact, the magical mass distribution $\mu(s)$ derived in Ch. 2 does *not* assume that the loopy ERSE is tied, so it is in principle possible that an untied ERSE exhibits persistent shape and everlasting double rotating motion much like the tied RSE. To explore this intriguing possibility, in chapter 3 we study the dynamics of the untied elliptical RSE. Its actual behavior was found to depend on the length of its long semi-axis a (perpendicular to the Earth in Fig. 2). We find that there are two characteristic values of a, called a_{hopping} and $a_{\text{unbinding}}$. If $a < a_{\text{hopping}}$, the untied ERSE exhibits nearly the same dynamics as a tied ERSE. That is, its bottom and top points execute only very small oscillations about their initial positions. Thus, strikingly, untied ERSE bottom remains close to the Earth as if the RSE would be tied. On the other side, if $a > a_{\text{hopping}}$, the untied ERSE as a whole hops away and then it falls back to the Earth. The amplitude of this hopping (maximum height reached by the RSE bottom) increases with increasing a and it diverges as a approaches the $a_{\text{unbinding}}$. In this limit, as well as for any $a > a_{\text{unbinding}}$, the ERSE unbinds from the Earth much like an object with a speed above the second cosmic speed.

To streamline our discussions, a number of significant details is presented in the appendices to this thesis. Appendices A through F, to Chapter 2, include important details related to the RSE concepts and computational methods necessary for simulating the RSE dynamics.

Appendices A through F are described briefly as follows. Appendix A discusses inertial forces acting in double rotating frames. These results are further used to argue that the RSE can maintain a nearly constant shape if its line density $\mu(s)$ is chosen in a special way. The form of this “magical” $\mu(s)$ can be calculated for a given RSE shape. Thus, in the appendix B, we derive the magical $\mu(s)$ for the continuum model of RSE. In the appendix C, we derive the magical mass distribution for the discretized (finite element model) of RSE used in our simulation of the RSE dynamics. The discretized model used is essentially a chain of massive beads joined by massless Hookean springs.

The motion of the sliding climbers is discussed in more detail in the appendix D within the continuum RSE model. These climbers move in an oscillatory fashion by sliding between two turning points on the RSE. One of them is on the Earth and the other one is in the outer space. This kind of motion is however possible only if the angular velocity of RSE is higher than a certain critical angular velocity discussed in the appendix D.

Numerical algorithms used to model the RSE dynamics are discussed in the appendices E and F. We used a time discretized dynamics handled by the leapfrog algorithm outlined in the appendix E. Here we note that special care was needed to handle the velocity dependent Coriolis force. In the appendix F, we briefly describe the algorithm used to handle the interactions between the discretized RSE (=chain of linked beads) and a sliding climber. The essence of the algorithm is to separate the sliding climber motion into two parts. One part is the climber's sliding motion along the massless links between adjacent massive beads, whereas the other part is the close encounter ("collision") of the climber with a massive bead. Thus, in the discretized RSE model, the climber's motion is a sequence of sliding motions between beads alternating with collisions with individual beads. The resulting algorithm is quite subtle and formidable.

Appendix to Chapter 3 presents details of an analytical calculation of the dynamics of a dumbbell approximation to untied LSE/RSEs. The theory is used to analytically calculate eigen-mode frequencies of the untied ERSE for $a < a_{\text{hopping}}$ and to explain the hopping and unbinding transitions anticipated above. This analytic work also supplies additional confidence in our simulation numerical results.

Finally, in the last section of this Thesis, we summarize and discuss our main results.

1.4 References

[1] Jack and the Beanstalk, Wikipedia,

http://en.wikipedia.org/wiki/Jack_and_the_Beanstalk

[2] For an extensive review, see B. C. Edwards, and E. A. Westling, *"The Space Elevator: A Revolutionary Earth-to-Space Transportation System"* (BC Edwards, 2002). This book was motivated by the discovery of carbon nanotubes in the 1990s. More recently discovered strong materials, such as diamond nano-threads, may be even more promising for building space elevators.

[3] Y. Artsutanov, "V Kosmos na Electrovoze (in Russian, Into Space on a train)," Komsomolskaya Pravda, July 31, 1960. See also, V. Lvov, "Sky-Hook: Old Idea", Science **158** (1967) 946.

[4] J. Pearson, "The orbital tower: a spacecraft launcher using the Earth's rotational energy", Acta Astronautica **2** (1975) 785.

[5] J. Pearson, E. Levin, J. Oldson and H. Wykes, "Lunar Space Elevators For Cislunar Space Development", NIAC Phase I Final Technical Report, May 2, 2005, p. 12

[6] B. Gassend, "Non-Equatorial Uniform-Stress Space Elevators", http://gassend.net/publications/NonEquatorialUniformStressSpaceElevators.pdf, accessed 1/21/2014

[7] A. C. Clarke, "*The Fountains of Paradise*" (Harcourt Brace Jovanovich, 1978).

[8] A. C. Clarke, The Space Elevator: " 'Thought Experiment' or Key to the Universe? ", in *Advanced Earth Oriented Applied Space Technology,* Vol. **1**, 39 (Pergamon Press, London, 1981).

[9] L. Golubovic and S. Knudsen, "Classical and statistical mechanics of celestial scale spinning strings: Rotating space elevator", Europhysics Letters **86**, 34001 (2009).

Chapter 2

Rotating space elevators (RSE): celestial scale spinning strings

2.1 Introduction

Strings and membranes play prominent roles in modern day investigations in statistical physics [1,2], nonlinear dynamics [3], biological physics [4], and in applied physical sciences [5]. Technologically achievable celestial size strings are no exception to this [5,6]. Ever since an early dream of Tsiolkovsky [5], the vision of Space Elevator, a giant string connecting the Earth with heavens has intrigued diverse researchers as well as science fiction writers [5-8]. The space elevator reaches beyond the geosynchronous satellite orbit [5,6]. In its equilibrium state, the space elevator is straight and at rest in the non-inertial frame associated with the rotating planet thanks to a balance between the gravity and the centrifugal force acting on the long elevator string. A major shortcoming of this traditional linear space elevator (LSE) is that significant energy must be *locally* (by internal engines, propulsion, or laser light) supplied to climbers creeping along the LSE string to allow them to leave the gravitational potential trap of the Earth [5]. It may take several months to travel from the Earth to the geostationary level, through cosmic radiation strong in this range of altitudes. Such a long travel time itself is unsatisfactory feature of LSE, if a rapid deployment of objects into outer space is desired.

In this study we discuss a new venue in the physics of strings and membranes. We explore a novel class of nonlinear dynamical systems, Rotating Space Elevators (RSE). The RSEs are multiply rotating systems of strings. Remarkably, useful loads and humans *sliding* along RSE strings do *not* require internal engines or propulsion to be rapidly transported (sled) away from the Earth's surface into outer space, see Figs. 1 and 2. The nonlinear dynamics and statistical physics of RSE strings are shown here to be also interesting in their own right.

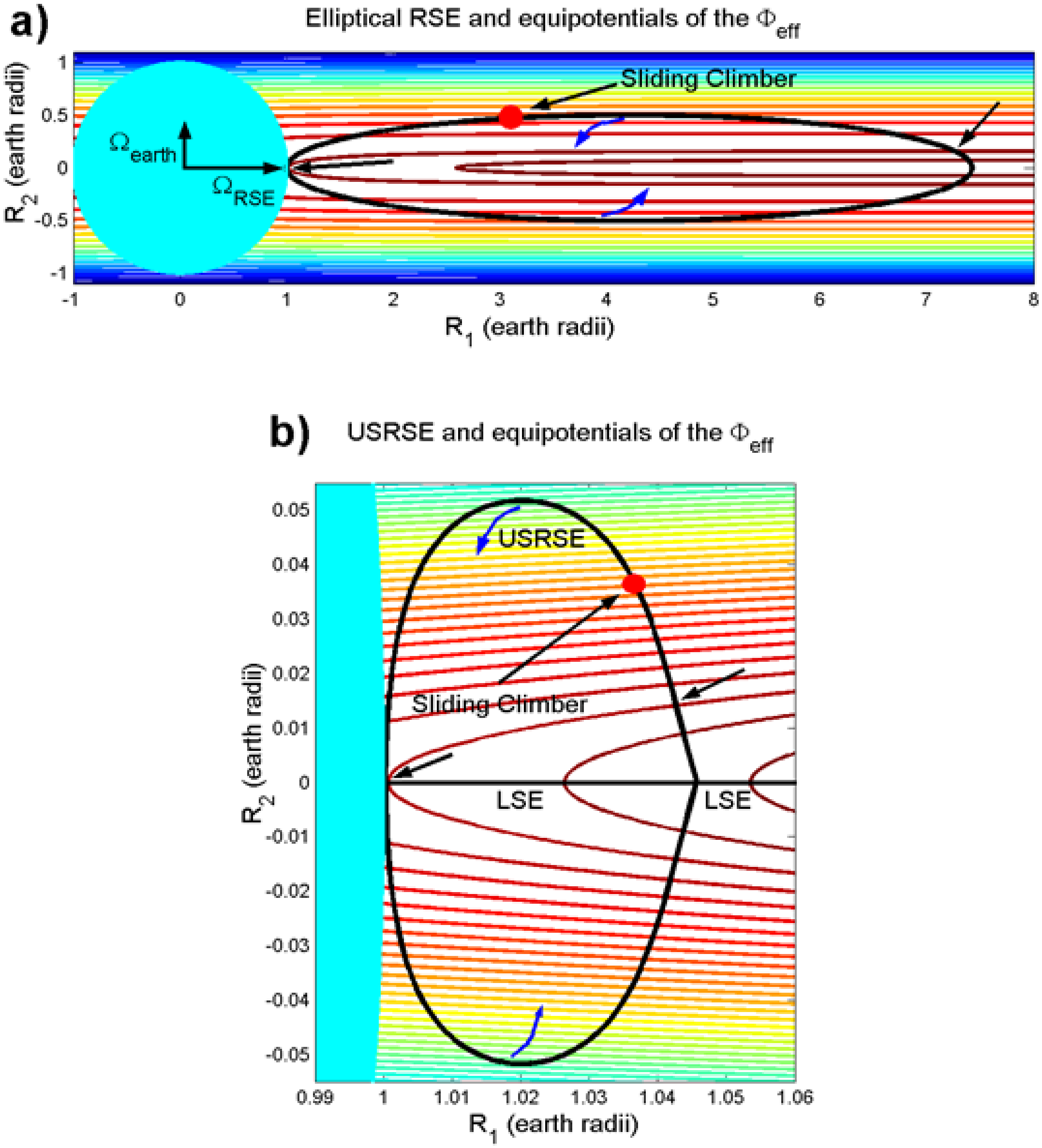

Fig. 1: In (a), the elliptical RSE with minor semi-axis *b*= 0.5 Earth radii and major semi-axis *a* = 3.2107 Earth radii (so its top is about 0.8 Earth radii above the geo-stationary level). In (b), we show the USRSE (attached to a LSE) with T_{RSE} = 4.22 min (discussed in Sec. 2.3). In these figures we include also the equipotentials of the effective potential in Eq. (7). Sliding climbers oscillate between two turning points (indicated by straight arrows) that are on the same equipotential.

Our RSE is a *double* rotating floppy string. In its quasi-periodic like state, the RSE motion is nearly a geometrical superposition of: (a) geosynchronous (one sidereal day period) rotation around the Earth, and (b) yet another rotational motion of the string which is typically much faster (with period=T_{RSE} ~ tens of minutes) and goes on around a line perpendicular to the Earth at its equator [the R_1 axis in Figs. 1(a) and (b)].

This second, internal rotation plays a very special role: It provides the dynamical stability of the RSE shape and, importantly, it also provides a mechanism for the climbing of objects free to slide along the RSE string. The RSE can be envisioned in various shapes; see Figs. 1(a) and (b). As discussed here, for a *given* RSE shape, by a special (magical) choice of the mass distribution of the RSE string, the simple double rotating geometrical motion can be (under some conditions) made to represent an approximate yet exceedingly accurate solution to the exact equations of the floppy RSE string dynamics.

In this Chapter, the peculiar RSE actions will be elucidated and documented in detail by numerical simulations, in Secs. 2.2 through 2.5. As important as these sections are the lengthy Appendices A through F at the end of this chapter. We will show that the major role in understanding the RSE action is played inertial forces [9]. The results discussed in detail in this chapter were described in a brief form in our Letter [10].

2.2 The physics and mathematics behind the RSE actions

In the inextensible limit, the Newtonian dynamics of the RSE floppy string is governed by the equation of motion

$$\mu(s)\frac{\partial^2 \vec{R}}{\partial t^2} = \frac{\partial}{\partial s} T(s,t) \frac{\partial}{\partial s} \vec{R} + \vec{f}_{ext} \tag{1}$$

Here, $\vec{R}(s,t)$ are 3-D space positions of string points parametrized by their arc-length distances s [i.e., $|\partial\vec{R}(s,t)/\partial s|=1$]. In Eq. (1), $\mu(s)$ is the local mass line density of the string, $T(s,t)$ is the local value of the tension field in the string, and $\vec{f}_{ext}$ stands for external forces (per unit length) acting on the string, such as the Earth gravity, for which

$$\vec{f}_{ext}^{\;grav} = \mu(s)\ \vec{a}_{grav},$$

with

$$\vec{a}_{grav} = -\frac{\partial\Phi_{grav}}{\partial\vec{R}}.$$

Here,

$$\Phi_{grav}(\vec{R}) = -\frac{GM_{earth}}{|\vec{R}|}$$

is the gravitational potential of the Earth's mass M_{earth}. Evolution of $T(s,t)$ is obtained by solving Eq. (1) combined with the local constraint $|\hat{t}(s,t)|=1$, with $\hat{t}(s,t)=\partial\vec{R}/\partial s$. In the presence of a sliding climber of mass m_{cl} at the arc-length distance $s(t)$, i.e., at the 3-D position $\vec{R}^{cl}(t)=\vec{R}(s(t),t)$, the external force density acting on the RSE, $\vec{f}_{ext}$ in Eq. (1) includes also the term

$$\vec{f}_{ext}^{\;cl} = -\delta(s-s(t))\ \vec{N},$$

where $\vec{N}$ is the normal force between the climber and the string; $\vec{N}\cdot\hat{t}=0$. The climber dynamics obeys the standard second Newton's law,

$$m_{cl}\frac{d^2\vec{R}^{cl}}{dt^2} = \vec{N} + \vec{F}_{ext},$$

with $\vec{F}_{ext}$ signifying (other than $\vec{N}$) external forces acting on the climber, such as the Earth's gravity,

$$\vec{F}_{ext}^{\ grav} = m_{cl}\ \vec{a}_{grav} = -m_{cl}\frac{\partial\Phi_{grav}}{\partial\vec{R}}.$$

Using the constraint $|\hat{t}(s,t)|=1$, from the above equations one finds

$$\ddot{s}(t) = \hat{t}\cdot\left(\frac{\vec{F}_{ext}}{m_{cl}} - \frac{\partial^2\vec{R}}{\partial t^2}\right), \tag{1'}$$

and

$$\vec{N} = -(\vec{F}_{ext})_{\perp} + m_{cl}\left(\frac{\partial^2\vec{R}}{\partial t^2}\right)_{\perp} + m_{cl}\frac{\partial\hat{t}}{\partial s}[\dot{s}(t)]^2 + 2m_{cl}\frac{\partial\hat{t}}{\partial t}\dot{s}(t),$$

with $(\vec{V})_{\perp} = \vec{V} - \hat{t}(\hat{t}\cdot\vec{V})$ for any vector $\vec{V}$.

In *a non-inertial* frame rotating with the angular velocity $\vec{\Omega}$, inertial forces have to be included into $\vec{f}_{ext}$ and $\vec{F}_{ext}$ in Eqs. (1) and (1′), yielding

$$\vec{f}_{ext} = \mu(s)\ (\vec{a}_{grav} + \vec{a}_{inert}),\ \vec{F}_{ext} = m_{cl}\ (\vec{a}_{grav} + \vec{a}_{inert}), \tag{2}$$

with [9]

$$\vec{a}_{inert} = \vec{\Omega}\times(\vec{R}\times\vec{\Omega}) + \vec{R}\times\frac{d\vec{\Omega}}{dt} + \frac{d\vec{R}}{dt}\times 2\vec{\Omega}. \tag{3}$$

In the geosynchronous frame (used in our simulations and the figures displayed here) rotating with the period = $2\pi/\Omega_{earth}$ = one day, Eq. (3) is employed with

$$\vec{\Omega} = \vec{\Omega}_{earth} = \hat{e}_2\Omega_{earth},$$

with unit vector $\hat{e}_2$ along the Earth polar axis and the equator in the (R_1, R_3) plane; see Figs. 1(a) and (b). In the simulations, at $t = 0$ the RSE is initially in the (R_1, R_2) plane. To initiate the double rotation motion, the RSE is given initial spin around the R_1-axis, with the angular velocity Ω_{RSE}. The RSE bottom point is tied to the Earth to provide access for the sliding climbers starting there their trip into outer space. Other than this, *the RSE moves purely under the influence of inertia and gravity.* In our simulations, the inextensible continuum string model Eq. (1) is replaced by a finite element polymer like model of point masses ("beads") linked by stiff Hookean springs, see appendix C. Other sophisticated details of our simulations are discussed in the appendices E and F at the end of this chapter.

An outstanding feature of the RSE double rotation motion is that it provides a natural mechanism which efficiently moves sliding *engine free* climbers from the Earth surface to remote outer space destinations. As evidenced by our simulations, a sliding climber starting at rest close to the Earth *spontaneously* oscillates between its initial position and a turning point in outer space; see Fig. 2. Nearly periodic character of the climber's motion is explained in Sec. 2.4. See also appendix D.

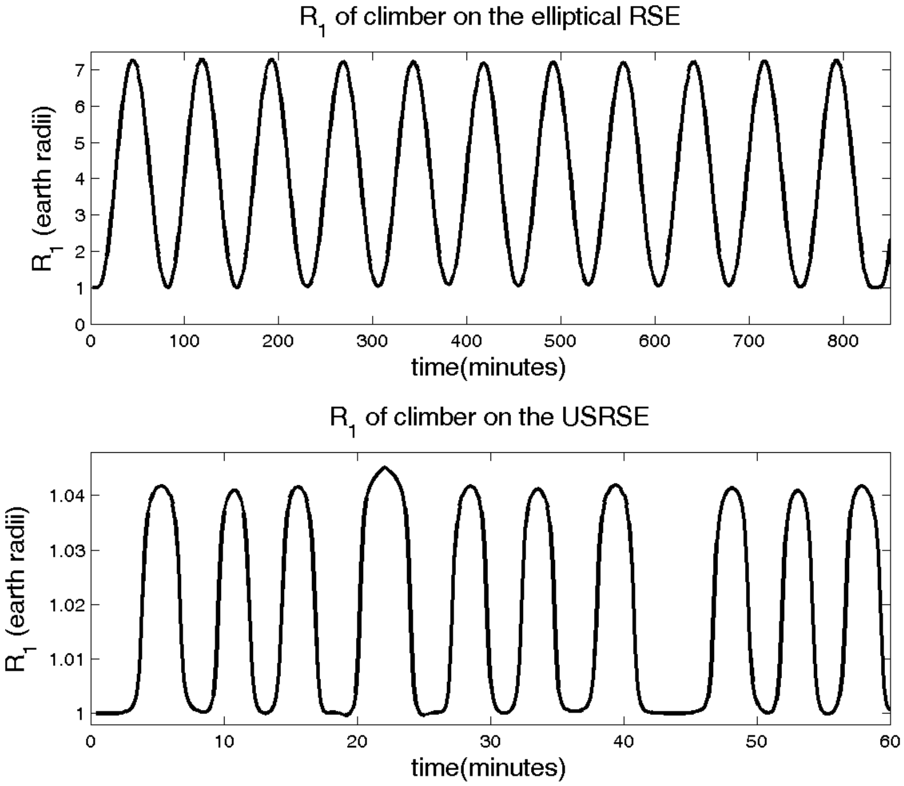
R_1 of climber on the elliptical RSE

R_1 of climber on the USRSE

Fig. 2: From our simulations, the upper panel: The $R_1(t)$ coordinate of the climber sliding with no friction along the floppy RSE with the (initial) shape in Fig. 1(a) and T_{RSE}=10.83 min. The maximum climber velocity relative to the string has magnitude about 29 km/s while the minimum speed is zero at the turning point. The lower panel: The $R_1(t)$ coordinate of the climber on the floppy RSE with initial shape in Fig. 1(b) with T_{RSE}=4.22 min. See Sec. 2.4 for the analytic explanation of the nearly periodic character of climbers motion. The maximum climber velocity relative to the string is about 8 km/s, while the minimum speed is zero. Note: With a weak sliding friction, climbers would eventually stop near the RSE point minimizing the $U(s) = \Phi_{eff}(\vec{R}(s))$. From the equipotentials of the effective potential labeled in Fig. 1, one can see that this point occurs close to the RSE point maximizing its R_2 coordinate in Fig. 1.

The second striking feature is an enduring stability of the RSE sizes and orientation and of its double rotation motion that we achieved by specially chosen form of the mass line density $\mu(s)$; see Eq. (8) below. This feature is documented by our simulations discussed in Sec. 2.5.

These two unique RSE features *both* emerge by considering the system in the (natural for the RSE) *double rotating frame* (DRF) obtained from the geosynchronous (single rotating) frame by adding to it the rotation around the R_1-axis in Figs. 1(a) and (b). The net angular velocity of the DRF is thus $\vec{\Omega}(t) = \vec{\Omega}_{RSE} + \vec{\Omega}_{earth}(t)$. Here, $\vec{\Omega}_{RSE} = \Omega_{RSE}\hat{e}_1$ corresponds to the rotation around the R_1-axis while $\vec{\Omega}_{earth}(t)$ is the Earth's angular velocity vector which in the DRF rotates with the angular velocity $-\Omega_{RSE}$ (and thus acquires a time-dependence). With this $\vec{\Omega}(t)$, in DRF Eq. (3) yields

$$\vec{a}_{inert} = -\frac{\partial \Phi_{inert}}{\partial \vec{R}} + \vec{a}_{res}\,, \tag{4}$$

with

$$\Phi_{inert}(\vec{R}) = -\frac{1}{2}\Omega^2_{earth}R_1^{\ 2} - \frac{1}{2}(\Omega^2_{RSE} + \frac{1}{2}\Omega^2_{earth})(R_2^2 + R_3^2), \tag{5}$$

being a *time-independent* effective potential generating inertial forces sensed in the DRF. The residual, $\vec{a}_{res}$ term in Eq. (4) includes velocity dependent terms that vanish for an object *at rest in the DRF,* as well as *fast time-dependent* oscillatory terms of $\vec{a}_{inert}$ (with frequencies Ω_{RSE} and $2\Omega_{RSE} >> \Omega_{earth}$) that have *zero* time average over one RSE period ($T_{RSE} = 2\pi / \Omega_{RSE}$). We discuss these important details in the Appendix A at the end of this chapter. For the here interesting situations with $\Omega_{RSE} >> \Omega_{earth}$

[$T_{RSE} \sim 10\min << T_{earth} = 2\pi / \Omega_{earth} =$ 1 sidereal day] the potential term in Eq. (4) dominates over the $\vec{a}_{res}$ term; see the discussions in the Appendix A. Thus, Eq. (2) reduces to

$$\vec{f}_{ext} \cong -\mu(s)\,\frac{\partial \Phi_{eff}}{\partial \vec{R}}\,, \quad \vec{F}_{ext} \cong -m_{cl}\,\frac{\partial \Phi_{eff}}{\partial \vec{R}}\,, \tag{6}$$

with the net effective potential,

$$\Phi_{eff}(\vec{R}) = \Phi_{grav}(\vec{R}) + \Phi_{inert}(\vec{R}) = -G\frac{M_{earth}}{|\vec{R}|} + \Phi_{inert}(\vec{R}). \tag{7}$$

The time *independence* of the $\Phi_{eff}(\vec{R})$ allows one to find a magical mass distribution $\mu(s)$ with which the RSE string will *indefinitely* maintain its initial shape by remaining at rest *in* the DRF. For a *given* flat RSE string shape specified by a 2-d curve $\vec{R}(s) = [R_1(s), R_2(s), R_3(s) = 0]$, this mass distribution can be found from Eq. (1) with $\partial^2\vec{R}/\partial t^2 = 0$ and $\vec{f}_{ext}$ as in Eq. (6). The resulting differential equations for $T(s)$ and $\mu(s)$ can be integrated exactly [see the Appendix B at the end of this chapter], yielding our magical mass line density $\mu(s)$,

$$\ln\left[\frac{\mu(s)}{\mu(0)}\right] = -\int_0^s ds' \, \frac{(\vec{a}_{net}(s')\cdot\hat{t}(s'))}{K(s')} + \ln\left[\frac{K(s=0)}{K(s)}\right]. \tag{8}$$

Here,

$$\vec{a}_{net} = -\frac{\partial\Phi_{eff}}{\partial\vec{R}}$$

is evaluated at the RSE point $[R_1(s), R_2(s)]$, whereas

$$K(s) = -\frac{(\vec{a}_{net}(s)\cdot\hat{n}(s))}{C(s)} = \frac{T(s)}{\mu(s)}. \tag{8'}$$

In Eq. (8′), $C(s)$ is the local RSE string curvature; $C(s) = d\theta / ds$ with $\theta(s)$, the angle between the tangent unit vector $\hat{t}(s) = \partial\vec{R} / \partial s$ and the $R_1 -$axis in Figs. 1(a) and (b). The unit vector $\hat{n}(s)$ makes the angle $\theta(s) + \pi / 2$ with the $R_1 -$axis. The magical mass distributions obtained by applying Eq. (8) to the (initial) RSE shapes which are studied in the simulations discussed in this chapter are shown in Fig. 3.

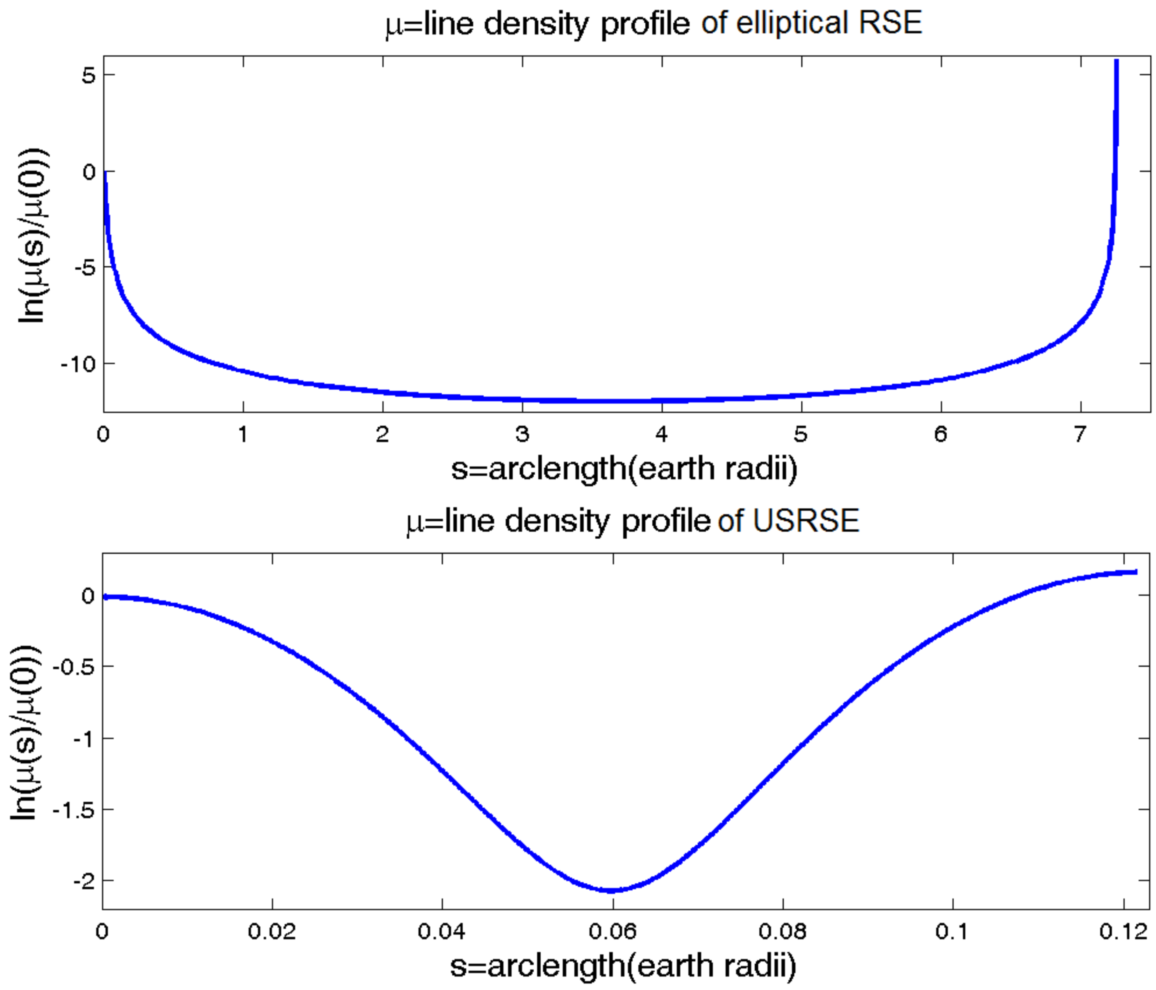

Fig. 3: The upper panel: the magical mass distribution [i.e., line density obtained by Eq. (8)] of the RSE with the shape in Fig. 1(a) and $T_{RSE} = 10.83\min$. The lower panel: the magical mass distribution (line density) of the RSE with the shape in Fig. 1(b) and $T_{RSE} = 4.22\ \min$.

As detailed in Sec. 2.5, the results of our simulations [which are free of the approximation Eq. (6) employed in Eq. (8)] indeed evidence (under the conditions discussed in Sec. 2.5) a remarkable stability of the RSE sizes and orientation provided by the magical mass distribution in Eq. (8). We note that $\mu(s) = \rho\ A(s)$, with ρ the density of the RSE material and $A(s)$ =the string cross-sectional area (that can be made to vary along the RSE by tapered cable design; see Ref. [5]). Thus, by Eq. (8′), the tensile stress

$$p(s) = \frac{T(s)}{A(s)} = \rho\ K(s) \tag{8″}$$

2.3 Uniform Stress RSE (USRSE)

The RSE shown in Fig. 1(b) is actually a *uniform stress* RSE (USRSE) for which the tensile stress $p(s)$ is s-independent. For an USRSE, by Eq. (8″), the $K(s) = K = const.$ With this condition, Eq. (8′) yields the second order differential equation

$$\frac{d^2R_2}{dR_1^{\ 2}} = -\frac{1}{K}\left[1+\left(\frac{dR_2}{dR_1}\right)^2\right]\left[a_2 - a_1\frac{dR_2}{dR_1}\right], \tag{8‴}$$

with $a_i = -\partial\Phi_{eff} / \partial R_i;\ \ i = 1,\ 2$. Our differential equation Eq. (8‴) can be used to obtain a USRSE shape for *any* given K and T_{RSE}. The equation is easily solved numerically by using Wolfram's Mathematica. Fig. 1(b) shows thus obtained USRSE shape for $T_{RSE} = 4.22\ \min$ and $K = \tilde{K}\ v_1^{\ 2}$. Here, $v_1 = (GM_{earth} / R_{earth})^{1/2} = 7.89 km/\sec =$ 1st cosmic speed [R_{earth} =the Earth radius], whereas $\tilde{K}$ is a dimensionless constant. For the USRSE in Fig. 1(b), we set $\tilde{K} = 1/4$, corresponding, by Eq. (8′′), to the USRSE tensile stress $p = \tilde{K}\rho\, v_1^2 = 20.24\ GPa$ if the USRSE is made of carbon nano-tubes (CNT) with $\rho \approx 1{,}300 kg/m^3$ [11]. Thus, pleasingly, the tensile stress p of this USRSE is smaller than the tensile strengths $p_{\max} \approx 60\ GPa$ of single-wall CNT, and $p_{\max} \approx 150\ GPa$ of multi-wall CNT, [11]. *So, this* USRSE *is technologically achievable with modern day materials.* By Eq. (8) with $K(s) = K = const.$, and by

$$-\vec{a}_{net} \cdot \hat{t} = (\partial\Phi_{eff} / \partial\vec{R}) \cdot (\partial\vec{R} / \partial s) = \partial\Phi_{eff}(\vec{R}(s)) / \partial s,$$

we find that the USRSE magical mass line density obeys the equation

$$\ln\left[\frac{\mu(s)}{\mu(s_1)}\right] = \ln\left[\frac{A(s)}{A(s_1)}\right] = \frac{\Phi_{eff}(\vec{R}(s)) - \Phi_{eff}(\vec{R}(s_1))}{K}, \qquad (8'''')$$

for any $(s,\ s_1)$. It is depicted in lower panel of Fig. 3 for the USRSE in Fig. 1(b) [with T_{RSE}=4.22 min, and $\tilde{K} = 1/4$], with $s_1 = 0$ corresponding to the USRSE bottom at the Earth. This line density profile can be technologically achieved by using tapered cable having the cross-sectional area $A(s)$ given by our Eq. (8′′′′). The USRSE in Fig. 1(b) is actually attached to a LSE which can be also designed to have a uniform stress $< p_{\max}$ [6]. The LSE line mass density has a discontinuity at the junction between the USRSE and the LSE (to balance the USRSE tension force pulling down the LSE along the R_1-axis). Away from the junction, the uniform stress LSE line mass density obeys Eq. (8′′′′) with $\vec{R}(s) = (R_1 = s, R_2 = 0, R_3 = 0)$ [6]. We note that unlike our technologically achievable USRSE in Fig. 1(b) with $p < p_{\max}$ (for CNT), the elliptic RSE in Fig. 1(a) has a *non*-uniform stress that actually exceeds the CNT tensile strength in the midsection of the RSE.

2.4 Climber dynamics along RSE

Nearly periodic motion of sliding climbers (seen in Fig. 2 from our simulations) proceeds along (nearly) constant shape lines, and it can be understood in terms of Eq. (6). By it, for a time-independent RSE shape $\vec{R}(s)$, the Eq. (1′) reduces to

$$\ddot{s} = -\hat{t}(s) \cdot \frac{\partial \Phi_{eff}}{\partial \vec{R}(s)} = -\frac{\partial \vec{R}(s)}{\partial s} \cdot \frac{\partial \Phi_{eff}}{\partial \vec{R}(s)} = -\frac{\partial \Phi_{eff}(\vec{R}(s))}{\partial s},$$

yielding the conservation law

$$\frac{1}{2}\left(\frac{ds(t)}{dt}\right)^2 + \Phi_{eff}[\vec{R}(s(t))] = const., \qquad (9)$$

isomorphic to the one describing oscillatory 1-d motion of a particle with the position $s(t)$ in the potential $U(s) = \Phi_{eff}(\vec{R}(s))$. Strikingly, in this potential, sliding climbers simply oscillate between two turning points, one of which is close to the Earth (starting point) whereas the other one is in outer space; see Figs. 1 and 2 [see the Appendix D for more details]. In fact, as shown in the Appendix D, the RSE bottom (the point $s = 0$) becomes a local maximum of the potential $U(s)$ (seen by sliding climbers) provided the RSE angular frequency Ω_{RSE} is bigger than the minimal frequency,

$$\Omega_{\min} = \frac{v_1}{R_{earth}}(1 + R_{earth}\,|\,C(s=0)\,|)^{1/2} = \frac{v_1}{R_{earth}}(1 + \frac{1}{\tilde{K}(s=0)})^{1/2}, \qquad (10)$$

with $\tilde{K}(s) = K(s)/v_1^2$. Due to this, for $\Omega_{RSE} > \Omega_{\min}$, i.e., $T_{RSE} < T_{\max} = 2\pi/\Omega_{\min}$, a climber initially at rest will start moving up no matter how close is its initial position to the RSE bottom $[R_1 = R_{earth}, R_2 = R_3 = 0)]$ in Figs. 1(a) and (b), at $s = 0$. For the elliptical RSE in Fig. 1(a) with the semi-axes $b = 0.5\ R_{earth}$, $a = 3.2107\ R_{earth}$, the climbing threshold RSE period $T_{\max}$ = 22.71 min. For an USRSE with $\tilde{K}(s) = 1/4$, by Eq. (10), $T_{\max} = 37.78$ min. This is bigger than the T_{RSE} of 4.22 min. of the USRSE in Fig. 1(b), yielding the oscillatory sliding climber dynamics seen in our simulations in Fig. 2, lower panel. We note that the USRSE point having the maximum distance R_2 away from the R_1 −axis in Fig. 1(b) has the speed $\Omega_{RSE} \cdot (R_2)_{\max} \cong v_1$ =1st cosmic speed (for the USRSE with T_{RSE}=4.22 min). Thus, the USRSE loop in Fig. 1(b) can be used for launching satellites. We will discuss potential applications of the RSE in Sec. 2.6.

It is significant to note that [by using differential Eq. (8′′′)] the USRSE loops can be designed with their bottoms anywhere above the Earth surface (e.g., above the dense atmospheric layer, to avoid significant air-resistance).

2.5 Morphological stability of tied RSE and crumpling transition

Our simulations reveal an interesting morphological phase transition of the RSE strings that occurs with changing the (initial) RSE angular frequency Ω_{RSE}, i.e., its period T_{RSE}. A similar transition has been observed both in the USRSE and the elliptical RSE. e.g., for the elliptical RSE in Fig 1(a), it occurs at a critical value for the RSE period $T_{crit} \approx 17\min$.

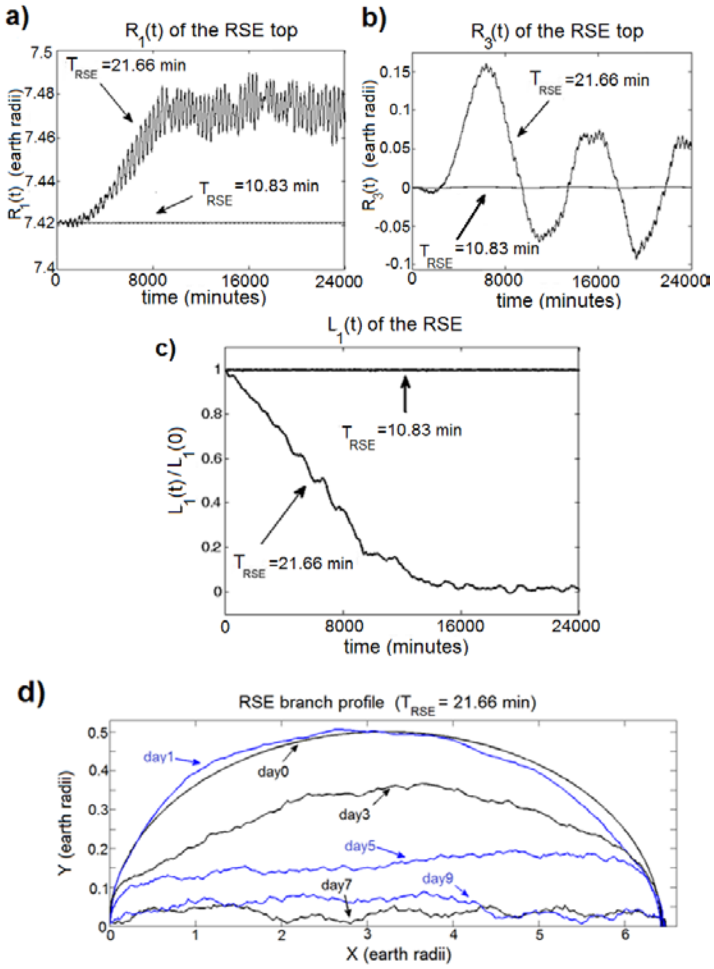

Fig 4: From our simulations: For the elliptic RSE in Fig. 1(a), the RSE top coordinates $R_1(t)$ in (a), $R_3(t)$ in (b), and, in (c), the evolution of the RSE angular momentum L_1 about the R_1-axis (in the frame rotating with the Earth), for $T_{RSE} = 10.83\,\text{min}$ and $T_{RSE} = 21.66\,\text{min}$. In (d), the evolution of the RSE profile (of one of its two branches), for $T_{RSE} = 21.66\,\text{min}$ over the first ten days. Here, for any RSE point P, the Y is its distance away from the (instantaneous) axis *A* connecting the RSE bottom and top, and X is the distance between the normal projection of P onto the axis *A* and the RSE bottom point (at $X = 0$).

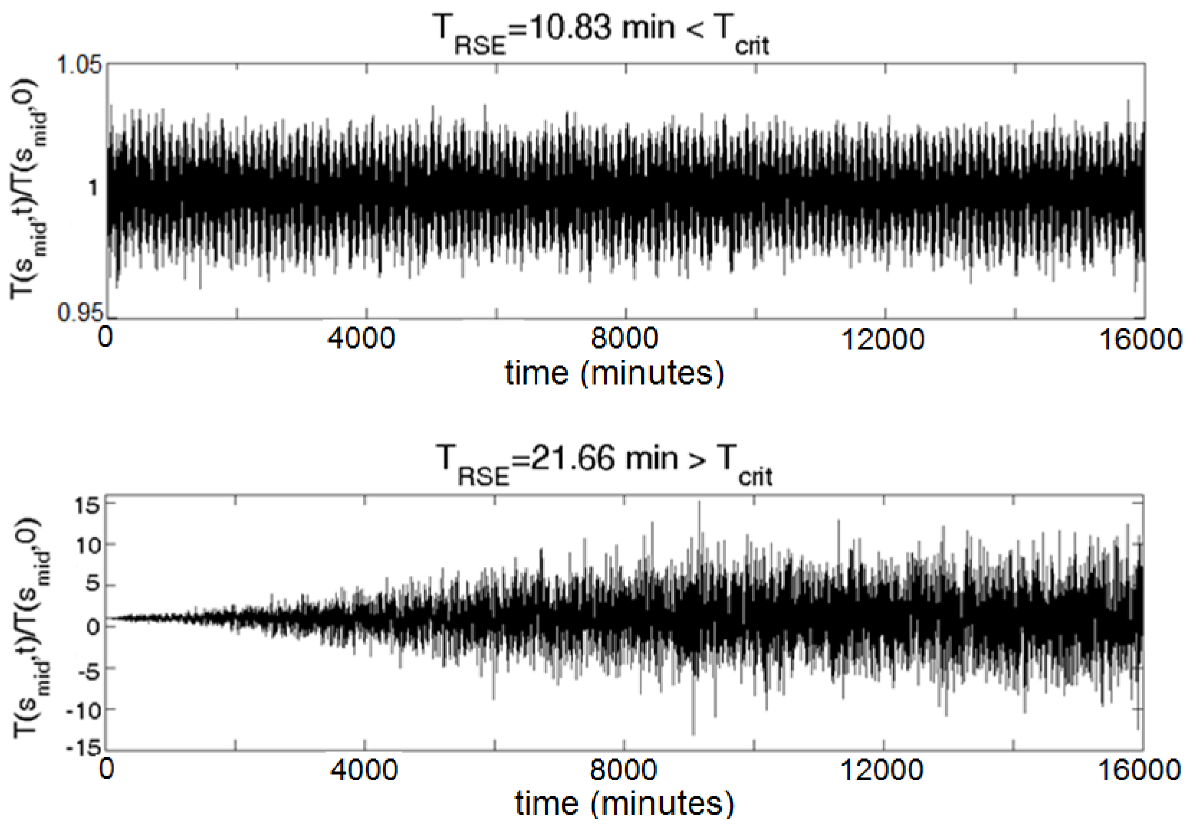

Fig. 5: Evolution of the tension at the midpoint of the elliptic RSE in Fig. 1(a). Upper panel: T_{RSE} = 10.83 min, whence the tension oscillations remain small and the tension remains positive. Lower panel, T_{RSE} = 21.66 min, whence the tension oscillations become huge, and the tension assumes both positive and negative values.

For the RSEs with periods $T_{RSE} < T_{crit}$, the tension field $T(s,t)$ remains everywhere positive. It exhibits only small oscillations around the initial tension $T(s,t=0)>0$ given by Eqs. (8) and (8′); see Fig. 5, upper panel, for T_{RSE}= 10.83 min. The RSE's shape and sizes are stable, as documented in Fig. 8, and in Figs. 4(a) and (b) with T_{RSE}= 10.83 min < T_{crit}=17 min [for the elliptic RSE depicted in Fig. 1(a)]. Note that the RSE top oscillations around its initial position are very small. On the other side, for $T_{RSE} > T_{crit}$, the RSE string (in both the elliptical RSE and the USRSE) undergoes a profound shape change and prominently chaotic long time dynamics: Tension field was found to develop a noise like pattern in which $T(s,t)$ assumes both positive and negative values; see Fig. 5, lower panel, for T_{RSE} =21.66 min. In effect, the RSE string *crumples* due to the buckling of the string sections that are under locally negative tensions $T(s,t)$, [12]. Macroscopically, the string crumpling manifests itself through a narrowing of the RSE initial shape, seen in Fig. 4(d) for the elliptical RSE with $T_{RSE} = 21.66\,\mathrm{min}$. The narrowing eventually turns the elliptical RSE into two nearly independently fluctuating linear type space elevators connecting the massive elevator top and bottom regions. Apparently chaotic dynamics of the two elevator's branches indicates onset of an ergodic-like (thermal equilibrium like) state analogous to that of the directed polymers [1,2] stretched between the RSE top and bottom. Related to the RSE narrowing is the behavior of the RSE angular momentum L_1 about the R_1-axis (in the frame rotating with the Earth as in Fig. 1); see Fig. 4(c) for the elliptical RSE with $T_{RSE} = 21.66\,\mathrm{min}$: The L_1 decays to near zero over a two week period. [In contrast to this, for $T_{RSE} > T_{crit}$, the USRSE narrows and loses its L_1 only partially.] As seen in Figs. 4 (a) and (b) at $T_{RSE} = 21.66\,\mathrm{min}$, these phenomena induce a destabilization of the elliptical RSE top. It systematically drifts away from its initial position (at 0.8 Earth radii above geostationary level) to a new slightly higher position around which the RSE top continues to oscillate in a chaotic fashion; see Figs. 4(a) and 6(c). The strongly chaotic character of the dynamics is documented by the temporal autocorrelation function of the RSE top displacement $u_1(t) = R_1(t) - \langle R_1 \rangle$, with <> labeling the time average of R_1. The time autocorrelation function is, as usual [13], defined by the time (ergodic) average,

$$C(\tau) = \langle u_1(t) u_1(t+\tau) \rangle = \lim_{T\to\infty} \frac{\int_{t_{\min}}^{t_{\min}+T-\tau} dt\ u_1(t) u_1(t+\tau)}{T-\tau},$$

which we calculated using a T=200,000 min long time sequence of u_1. The sequence represents the last 200,000 min. of a 300,000 min. long simulation. The first $t_{\min}$=100,000 min of the simulations were excluded to diminish possible effects of the transient processes of the RSE narrowing (see Fig. 4) and assure that the RSE is a nearly stationary regime. From Fig. 6(d) we see that $\lim_{\tau\to\infty} C(\tau) \to 0$, for $T_{RSE} = 21.66\,\mathrm{min}$. This is in accord with the chaotic motion of the RSE top seen for T_{RSE}=21.66 min in Fig. 6(c). Interestingly, the motion seen in Fig. 6(c) has a character of a train of bursts ("chaotic beats") each lasting about 5000 min. Within a burst, the motion is periodic like with repetition period of about 330 min. The presence of bursts gives rise to an interesting form of the auto-correlation function in Fig. 6(d) which is reminiscent of a motion of *damped* oscillator (with period of 330 min) exhibiting beats with beat period of about 5000 min.

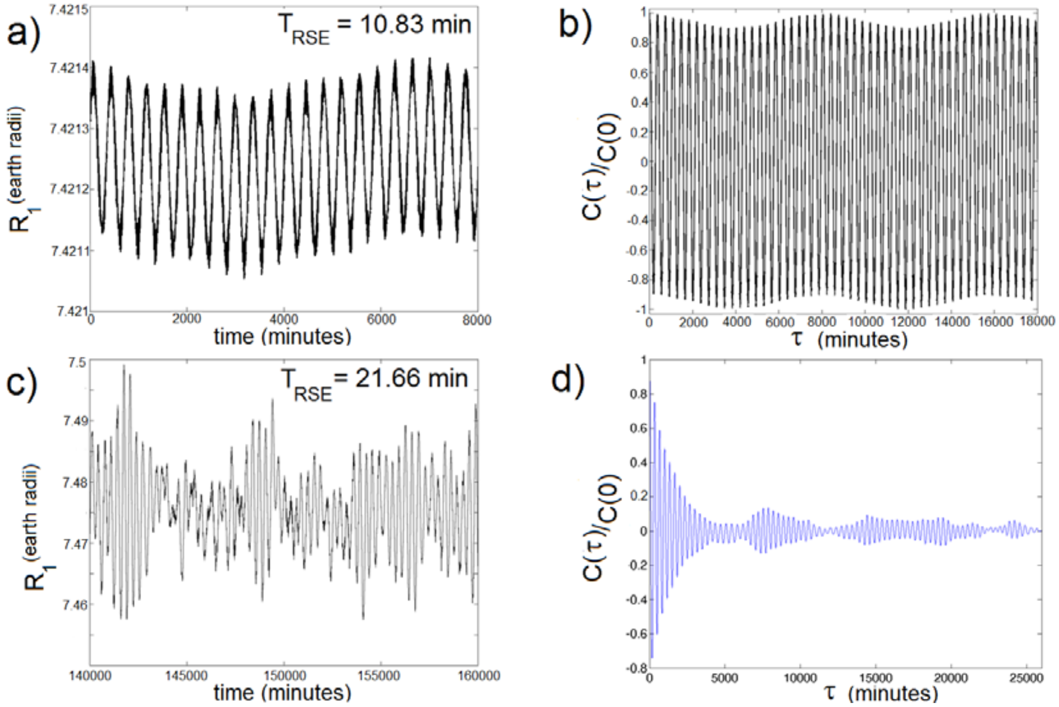

Fig. 6: Panel (a) displays a time sequence of the RSE top coordinate $R_1(t)$ for $T_{RSE} = 10.83\,\mathrm{min}$, while panel (b) displays corresponding time auto-correlation function (see the text). For this case, the auto-correlation function exhibits persistent oscillations reflecting regular non-chaotic motion seen in (a). This motion of $R_1(t)$ has period of 370 min. In addition, $R_1(t)$ also contains a weaker component with 8000 min period due to a coupling of $R_1(t)$ with $R_3(t)$ which executes a pendular motion with 8000 min period (see Fig. 7). Panel (c) displays a time sequence of the RSE top coordinate $R_1(t)$ for $T_{RSE} = 21.66\,\mathrm{min}$, while panel (d) displays corresponding time auto-correlation function (see the text). For this case, the auto-correlation function decays to zero reflecting the chaotic motion seen in (c). This motion of $R_1(t)$ seen in (c) is a train of bursts each lasting 5000 min. Within a burst, the motion is periodic like with period of about 330 min. The auto-correlation function in (d) is reminiscent of a motion of *damped* oscillator (with period of 330 min) exhibiting beats with beat period of about 5000 min.

In marked contrast to this, for $T_{RSE} < T_{crit}$, the string shapes of both the elliptic RSE and the USRSE remain nearly the same as in their initial configuration in Figs. 1(a) and (b), i.e., no RSE narrowing occurs. Related to this, as exemplified in Fig. 4 for the elliptical RSE with $T_{RSE} = 10.83\min$, the RSE angular momentum L_1 is nearly constant in time, whereas the RSE top executes only very small oscillations around its initial position.

For any $T_{RSE} < T_{crit}$, the motion of the RSE top is regular (non-chaotic), with two "macroscopically" visible slow modes: One of them is the top oscillation along the R_1 direction, see Figs. 6(a) and (b). This slow mode is essentially vibration of the length of the long elliptical RSE axis, with the period $T_{vib} \approx 370\min$ (seen in Fig. 6(a)) for the RSE in Fig. 1(b) with T_{RSE}=10.83 min. The other slow mode is essentially pendular (swinging) motion of the RSE top along the R_3 direction in the equatorial plane, with a long period $T_{pend} \approx 8000\min$, as can be (barely) seen in the Figure 4 (b) for T_{RSE}=10.83 min [for magnification, see Fig. 7, upper panel]. As seen in Figs. 4(a) and (b), both the pendular and vibrational modes are only weakly excited for $T_{RSE} < T_{crit}$. From the same figures, we can see that these modes get strongly amplified for $T_{RSE} = 21.66\min > T_{crit}$ when the RSE branches crumple and the RSE escapes into the strongly chaotic dynamical state with a narrowed, directed polymers-like morphology, as seen in Fig. 4(d). When this morphological transition happens, the RSE vibrational and pendular modes both assume a chaotic character seen in the RSE top motion at T_{RSE}=21.66 min in Figs. 4(a) and (b). We recall that the chaotic character of the top dynamics is reflected through the decay of temporal autocorrelations seen in the figure 6(d).

In addition to the above discussed two slow modes, which both go on in the equatorial (R_1-R_3) plane, for $T_{RSE} < T_{crit}$ the RSE top also executes small oscillations along the north-south (R_2) direction with one sidereal day period; see Fig. 7(b). Note that these oscillations proceed around a nonzero average value. Thus, the RSE long axis is slightly tilted out of the equatorial plane. This small tilt ($\sim \Omega_{earth} / \Omega_{RSE}$) is an effect of the $\vec{a}_{res}$ term in Eq. (2.4) [see App. A]. This term contains fast inertial forces with a zero time average [again, see App. A]. Yet, they still produce a small torque with a nonzero time average, which slightly tilts the RSE out of the

Earth equatorial plane. The torque can be shown to be proportional to the RSE angular momentum L_1 about the R_1-axis. Related to this, for $T_{RSE} > T_{crit}$ whence L_1 decays to zero at long times (recall of Fig. 5(c)), the small RSE tilt angle also decays to zero; see Fig. 7(c).

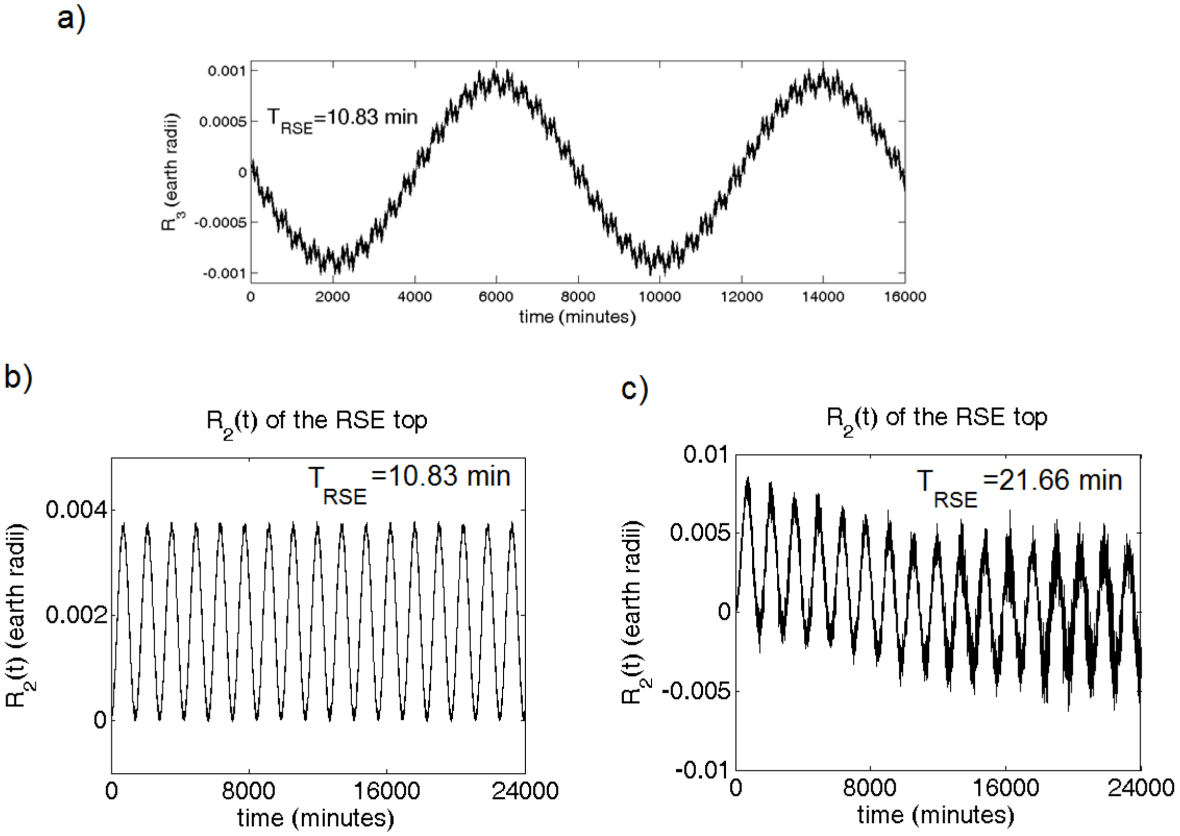

Fig. 7: In (a), R_3 coordinate of the top of the elliptic RSE (with T_{RSE}=10.83min <T_{crit}) exhibiting a slow pendular mode with the period of about 8000 min. In (b), R_2 coordinate of the top of the same elliptic RSE (with T_{RSE}=10.83min <T_{crit}) exhibiting one day period small oscillations around a small nonzero average value. Thus, the RSE long axis is slightly tilted out of the Earth equatorial plane. In (c), R_2 coordinate of the top of the narrowing RSE with T_{RSE}=21.66 min > T_{crit}. In this case, the average of R_2 (over one sidereal day period), slowly decreases to near zero value. Thus, the RSE tilt (out of the Earth equatorial plane) slowly decreases to zero value. This process parallels the decay of the RSE angular momentum seen in Fig. 5(c).

Let us discuss the RSE shape oscillations. For $T_{RSE} < T_{crit}$, these oscillations are weak and have the period = T_{RSE} . They are induced by the fast inertial accelerations contained in the a_{res} term in Eq. (4) of this chapter. This term is discussed in the appendix A. Main effect of this term is a weak RSE shape distortion due to the Coriolis force. It produces a shear like deformation of the RSE shape oscillating with the period = T_{RSE}, see Fig. 8(a). Due to it, the RSE points oscillate away from their initial positions with amplitude roughly proportional to their distance away from the R_1 axis in Fig. 1 of this chapter. Thus, the RSE appears somewhat like an object under a time periodic shear stress, see Fig. 8(a). These fast oscillations of the RSE shape are weak. In particular, these RSE shape oscillations do not significantly affect sliding climbers motion which is nearly periodic as seen in Fig. 2 of this chapter. Nearly periodic climbers dynamics can be understood by assuming a constant RSE shape, and by ignoring the fast inertial forces; see Sec. 2.4 and Appendix D. Main features of the climber dynamics can be thus understood purely in terms of the slow inertial forces and the gravitational force, both encoded in the effective potential in Eq. (7) of this chapter.

As seen in panel (b) of Fig. 8, the RSE shape oscillations have character of beats. For the RSE in Fig. 1(a), with T_{RSE}=10.83 min, the beat period, T_{beat} is about 115 min; see Fig. 8(b). The reason for the beats can be seen in Fig. 8(c) in which we display the power spectrum $P(f)$ obtained from a long time sequence of the coordinate $R_1(t)$ of a point on the RSE loop. The $P(f)$ exhibits a dominant peak at the frequency f'=0.09223 min^{-1} which is essentially the same as $f_{RSE}=1/T_{RSE}$. This peak represents the aforementioned oscillations driven by the Coriolis force; see appendix A. However, close to this peak of $P(f)$ there is a nearby peak at the frequency f''=0.10095 min^{-1} in Fig. 8(c), representing an eigen-mode of the RSE. Superposition of the oscillations associated with these two peaks gives rise to the beats seen in Fig. 8(b), with the beat period $T_{beat}=(f' - f'')^{-1}$=115min. In Fig. 8(d), we display time evolution of the RSE angular momentum $L_1(t)$ (around the R_1-axis). Notably, the $L_1(t)$ exhibits small oscillations having period equal to the period of the beats of $R_1(t)$ in Fig. 8(b). We stress that the power spectrum $P(f)$ contains a multitude of other peaks outside the frequency range displayed in Fig. 8(c). These other peaks are hundred or more times weaker than those displayed in (c). *All* the peaks of $P(f)$ were found to be of delta-function type, i.e., with the width $\sim 1/t_{max}$, where t_{max} is the length of the time sequence of $R_1(t)$ used to obtain the $P(f)$. Thus, the RSE shape executes a non-chaotic quasi-periodic dynamics.

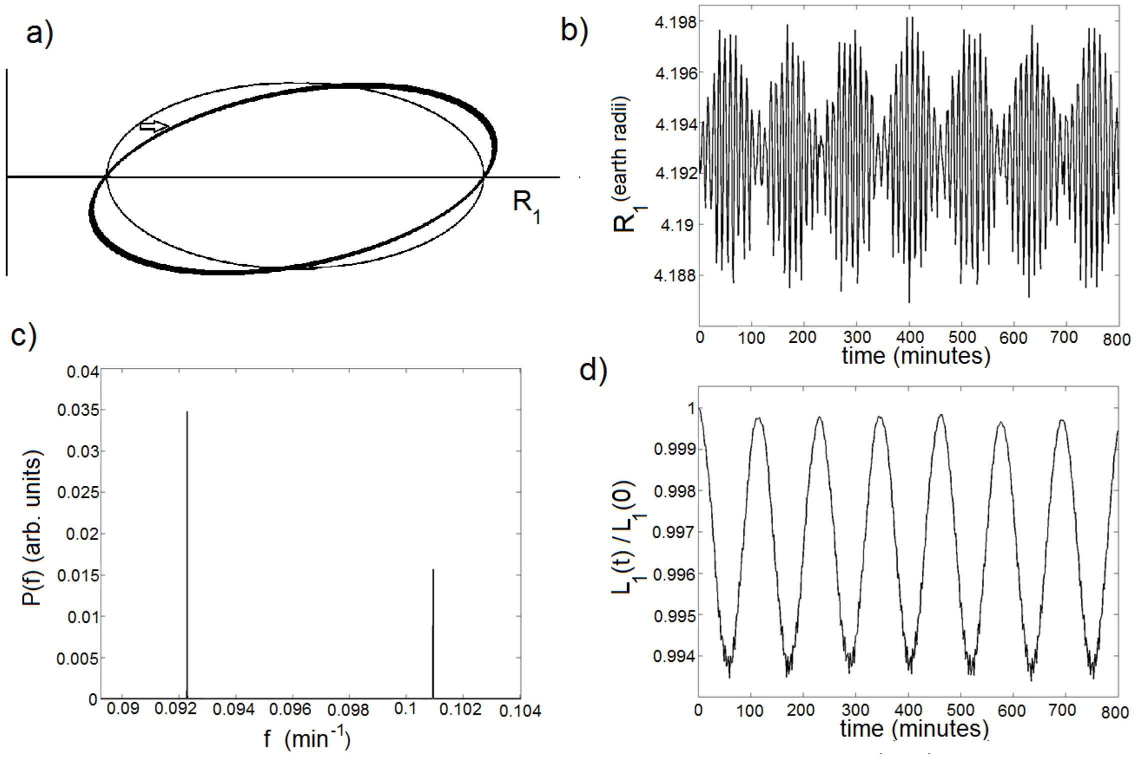

Fig. 8: (a) depicts small oscillations of RSE shape (thick line) about the initial shape (thin line). The RSE is somewhat like an object under a time periodic shear stress, with the period = T_{RSE}. Panel (a) is conceptual and it exaggerates the actual shape fluctuations seen in our simulations of the elliptic RSE in Fig. 1(a) with T_{RSE}=10.83 min; see panel (b). The panel displays the dynamics of $R_1(t)$ of the RSE point initially at $R_1(0)$=4.193 R_{Earth}. The point executes relatively small oscillations with a magnitude smaller than 0.005R_{earth} and the period = T_{RSE}=10.83 min. These oscillations have character of beats with the beat period T_{beat} of about 115 min; see panel (b). In (c) we display the power spectrum $P(f)$ obtained from a long time sequence of $R_1(t)$. The dominant peak is at the frequency f'=0.09223 min^{-1} which is essentially the same as $f_{RSE}=1/T_{RSE}$. However, there is nearby peak, at the frequency f''=0.10095 min^{-1}. Superposition of the oscillations associated with these two peaks gives rise to the beats seen in (b), with the beat period $T_{beat}=(f' - f'')^{-1}$=115min. In (d), we display time evolution of the RSE angular momentum L_1 (t) (around the R_1-axis). By (d), the L_1 (t) exhibits small oscillations having period equal to the period of the beats of $R_1(t)$ in (b). The power spectrum $P(f)$ contains a multitude of other peaks outside the frequency range displayed in (c). These other peaks are hundred or more times weaker than those displayed in (c).

2.6 Possible applications of RSEs to launch spaceships

By the results discussed in this chapter, RSEs are shown to be rapid outer space transportation systems that require no internal engines for the climbers sliding along the elevator strings. RSEs' action fundamentally employs basic natural phenomena -- gravitation and inertial forces. As noted before in Sec. 2.4, RSEs can be used to launch satellites. This RSE capability will be discussed in more detail in this section. In addition, the RSE strings can host space stations and research posts. Sliding climbers can be then used to transport useful loads and humans from the Earth to these outer space locations.

Satellites and spaceships carried by sliding climbers can be released (launched) along RSEs. Let us look at a climber that has started its motion at near rest at the RSE tying position with the Earth in Fig. 1 [there, $|\vec{R}(s=0)| = R_{earth}$]. Let us consider an object released from the climber when it reaches the RSE position $\vec{R}(s) = [R_1(s), R_2(s), R_3(s) = 0]$ in the DRF. The released object's speed in the DRF, that is its speed along the tangent at $\vec{R}(s)$ is *ds/dt*. This tangential velocity can be calculated by Eq. (9) of this chapter, yielding,

$$\frac{1}{2}\left(\frac{ds(t)}{dt}\right)^2 = \Phi_{eff}[\vec{R}(s(0)=0)] - \Phi_{eff}[\vec{R}(s(t))]. \tag{11}$$

Using here the Eqs. (5) and (7) of this chapter, we find,

$$\frac{1}{2}\left(\frac{ds(t)}{dt}\right)^2 = -G\frac{M_{earth}}{R_{earth}} + G\frac{M_{earth}}{|\vec{R}(s)|} + \frac{1}{2}\Omega^2_{earth}[R_1(s)]^2 + \frac{1}{2}(\Omega^2_{RSE} + \frac{1}{2}\Omega^2_{earth})[R_2(s)]^2. \tag{12}$$

Let us calculate the released object speed as observed in the *inertial frame.* Consider, for example, the situation in which the object is released when the elevator loop is in the plane of our Fig. 1 (then the R_2 axis of DRF points along the north-south direction), and let the object be released from a climber which is on the *lower branch* of RSE in Fig. 1. The RSE velocity at this point is in the direction of the Earth rotation and has the magnitude

$$v_{RSE} = \Omega_{RSE}\,|R_2(s)| + \Omega_{earth}R_1(s), \tag{13}$$

in the inertial frame. This velocity points into the plane of Fig. 1. In addition to this velocity, the released object has the above calculated tangential velocity *ds/dt* which is in the plane of Fig. 1. Thus, the total released object speed in the inertial frame, $v_{released}$ satisfies

$$v_{released} = \sqrt{(v_{RSE})^2 + (ds/dt)^2}\,. \tag{14}$$

By Eqs. (12-14),

$$\begin{aligned}&\frac{1}{2}(v_{released})^2\\ &= -G\frac{M_{earth}}{R_{earth}} + G\frac{M_{earth}}{|\vec{R}(s)|} + \frac{1}{2}\Omega^2_{earth}[R_1(s)]^2 + \frac{1}{2}(\Omega^2_{RSE} + \frac{1}{2}\Omega^2_{earth})[R_2(s)]^2\\ &+ \frac{1}{2}[\Omega_{RSE}\,|R_2(s)| + \Omega_{earth}R_1(s)]^2.\end{aligned}$$

Thus, the speed of the released object in the inertial frame satisfies the equation

$$\begin{aligned}&\frac{1}{2}(v_{released})^2\\ &= -G\frac{M_{earth}}{R_{earth}} + G\frac{M_{earth}}{|\vec{R}(s)|} + (\Omega^2_{RSE} + \frac{1}{4}\Omega^2_{earth})[R_2(s)]^2 + \Omega_{RSE}\Omega_{earth}\,|R_2(s)|\,R_1(s) + \Omega^2_{earth}[R_1(s)]^2,\end{aligned} \tag{15}$$

if the object is released when the elevator loop is in the plane of our Fig. 1, from a climber which is on the lower branch of RSE in Fig. 1. If this speed is large enough, the released object will unbind from the Earth, and reach the infinity with the speed v_∞ ("escape speed") that can be obtained from the equation

$$\frac{1}{2}(v_\infty)^2 = \frac{1}{2}(v_{released})^2 - G\frac{M_{earth}}{|\vec{R}(s)|}. \tag{16}$$

By Eqs. (15) and (16),

$$\begin{aligned}&\frac{1}{2}(v_\infty)^2\\&=-G\frac{M_{earth}}{R_{earth}}+(\Omega_{RSE}^2+\frac{1}{4}\Omega_{earth}^2)[R_2(s)]^2+\Omega_{RSE}\Omega_{earth}\,|\,R_2(s)\,|\,R_1(s)+\Omega_{earth}^2[R_1(s)]^2\\&=-(v_1)^2+(\Omega_{RSE}^2+\frac{1}{4}\Omega_{earth}^2)[R_2(s)]^2+\Omega_{RSE}\Omega_{earth}\,|\,R_2(s)\,|\,R_1(s)+\Omega_{earth}^2[R_1(s)]^2\\&=-(v_1)^2+[\Omega_{RSE}R_2(s)]^2\left[1+\left(\frac{\Omega_{earth}}{2\Omega_{RSE}}\right)^2+\frac{\Omega_{earth}R_1(s)}{\Omega_{RSE}R_2(s)}+\left(\frac{\Omega_{earth}R_1(s)}{\Omega_{RSE}R_2(s)}\right)^2\right].\end{aligned}\tag{17}$$

Above, we introduced the first cosmic speed $v_1=(GM_{earth}/R_{earth})^{1/2}=7.89km/\sec$. Again we stress that the Eq. (17) applies if the object is released when the elevator loop is in the plane of our Fig. 1, from a climber which is on the lower branch of RSE in Fig. 1. This situation is practically significant because the enhancement of the released object speed provided by the rotation of the Earth is at its best (for the RSE rotating around the R_1 axis in the direction indicated in Fig. 1). For the interesting (for RSE systems) situations with $\Omega_{RSE}>>\Omega_{earth}$ [see the discussions in Sec. 2.2, after Eq. (5)], the results in Eqs. (13), (15) and (17) reduce to approximate yet more illuminating results,

$$v_{RSE}\approx\Omega_{RSE}\,|\,R_2(s)\,|,\tag{13'}$$

$$\frac{1}{2}(v_{released})^2\approx-G\frac{M_{earth}}{R_{earth}}+G\frac{M_{earth}}{|\,\vec{R}(s)\,|}+\Omega_{RSE}^2[R_2(s)]^2,\tag{15'}$$

while the escape speed ("speed at infinity") approximately satisfies the simple equation,

$$\frac{1}{2}(v_\infty)^2\approx-(v_1)^2+[\Omega_{RSE}R_2(s)]^2.\tag{17'}$$

The approximations (13′),(15′), and (17′) are tantamount to ignoring the Earth rotation (setting Ω_{earth}=0] in the exact results in Eqs. (13), (15), and (17). Because of this, the above approximate results are significant also because they (approximately) apply to the objects released from the RSE at whatever orientation of the rotating RSE plane relative the R_1-R_2 plane in Fig. 1. [We stress that $|R_2(s)|$ in the above equations is the distance between the release point and the R_1 axis.]

The approximations (13′), (15′), and (17′) give a better, clear insight into the actions of the RSE. Thus, by Eq. (17′), we see that the released object will unbind from the Earth to an interplanetary travel [$(v_\infty)^2 > 0$] if the RSE speed at the point of release (=$\Omega_{RSE}|R_2(s)|$) is bigger than the first cosmic speed v_1. By the Eq. (17′), we also easily see that, for a given RSE, the highest possible escape speed v_∞ is achieved if the object is released from a sliding climber at the RSE point with the maximum value of R_2. For example, for the elliptic RSE in the figure 1(a), this point is the midpoint of the RSE, with $|R_2|_{max}$=0.5R_{earth} at R_1=(1+a) R_{earth}=4.2107 R_{earth}. At this point, with T_{RSE}=10.83 *min*, one has $\Omega_{RSE}|R_2(s)|$=3.9v_1. With this value, the Eq. (17′) predicts the value of the highest possible escape speed (speed at infinity) from this RSE to be $(v_\infty)_{\max} \approx 5.3310 v_1$. We recall that this is just an approximation but a good one. To see this, one can calculate the escape velocity by using the exact Eq. (17) [if the object is released when the elevator loop is in the plane of our Fig. 1, from a climber which is on the lower branch of RSE in Fig. 1(a)]. One thus obtains $v_\infty = 5.51997\ v_1 \approx 5.52 v_1$, only slightly bigger than the above approximate result based on Eq. (17′). More caution is needed in using the approximation if the $\Omega_{RSE}|R_2(s)|$ is exactly (or approximately) equal to v_1. In this case, Eq. (17′) predicts zero (or near zero) speed at infinity. Recall however that the approximate Eq. (17′) is based on ignoring small effects of the Earth rotation. Also recall that, that the Earth rotation enhances the released object speed in the case when the Eq. (17) applies [if the object is released when the rotating elevator loop is in the plane of our Fig. 1, from a climber which is on the lower branch of RSE in Fig. 1]. Thus, for the marginal case with $\Omega_{RSE}|R_2(s)|$=v_1, whence the approximation Eq. (17′) predicts $v_\infty = 0$, the exact equation (17) would yield an $(v_\infty)^2 > 0$, meaning that the object unbinds with a small escape velocity at infinity. A situation like this is (incidentally) realized in the USRSE in the Fig. 1(b), with T_{RSE}=4.22 min. For its point with the maximum value of R_2 ($|R_2|_{max}$=0.052 R_{earth} at R_1 =1.02R_{earth}) we find $\Omega_{RSE}|R_2(s)|$=1.04v_1 (which is only slightly above v_1). The approximate Eq. (17′) would then yield $v_\infty \approx 0.4040 v_1$, whereas the use of the exact Eq. (17) gives $v_\infty = 0.54303 v_1$ for this case [if the object is released when the elevator loop is in the plane of our Fig. 1, from a climber which is on the lower branch of USRSE in Fig. 1(b)]. Apparently from these numbers, the use of the exact formula is recommended if the $\Omega_{RSE}|R_2(s)|$ is exactly (or approximately) equal to v_1.

We recall that the actual shape of a USRSE loop is determined by solving the differential equation (8′′′), and thus it depends on the value of T_{RSE}=2π/Ω_{RSE}. In Fig. 9, we plot the USRSE shapes obtained for several different values of T_{RSE} , all for the same value of the parameter $\tilde{K} = 1/4$ (corresponding to the string tensile stress $p = 20.24\ GPa$ if the USRSE is made of carbon nano-tubes, see Sec. 2.3). In Fig. 9, we also plot, versus T_{RSE}, the USRSE speed $\Omega_{RSE}|R_2(s)|_{\max}$ as well as the speed at infinity v_∞ of an object released from a climber at $|R_2(s)|_{\max}$ on the lower branch of USRSE in Fig. 1(b) when this branch is in the plane of our Fig. 1. With a known RSE shape, this speed can be calculated from Eq. (17). Note that v_∞ vanishes at a characteristic value of T_{RSE}.

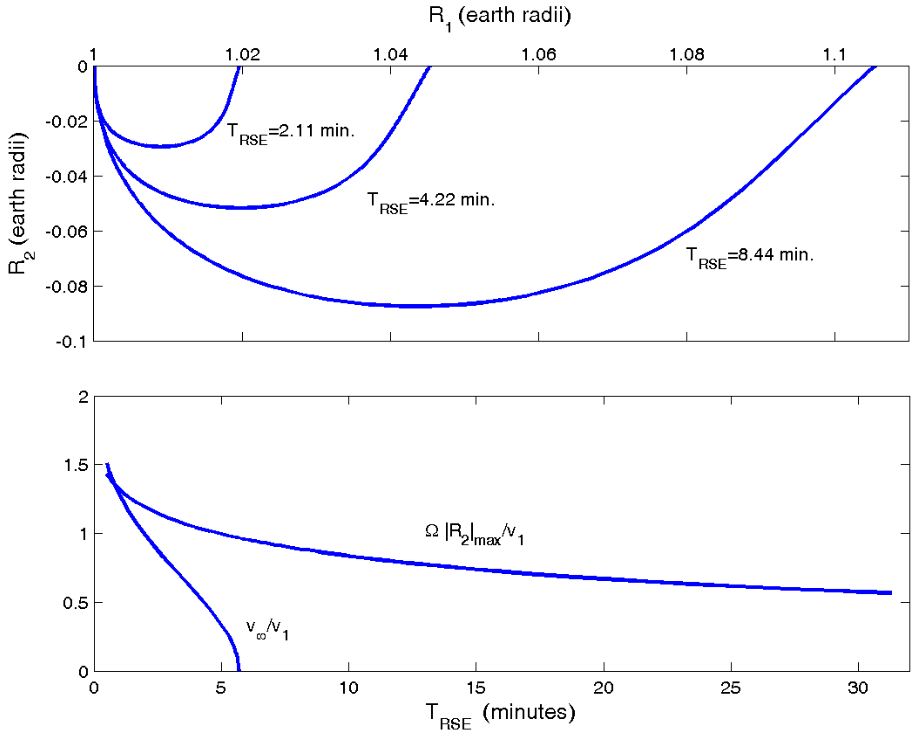

Fig. 9: In the upper panel, we plot the USRSE loop shapes obtained for several different values of T_{RSE} , all for the same value of the parameter $\tilde{K} = 1/4$. In the lower panel, we plot, versus T_{RSE}, the USRSE speed $\Omega_{RSE}|R_2(s)|_{\max}$ as well as the speed at infinity V_∞ of an object released from a sliding climber at $|R_2(s)|_{\max}$ on the lower branch of USRSE in Fig. 1(b) when this branch is in the plane of our Fig. 1. It is obtained from Eq. (17). The two speeds are given in units of the first cosmic speed v_1.

In the above discussions, we have assumed zero friction between the sliding climber and the RSE string, whence the Eq. (10) applies. The friction may be indeed reduced to a near zero value, for example, by applying a magnetic levitation. With a weak sliding friction present, climbers would eventually (after executing many under-damped oscillations) stop near the RSE point minimizing the effective potential seen by the climber in DRF, $U(s) = \Phi_{eff}(\vec{R}(s))$. From the equipotentials labeled in Fig. 1, one can see that this point occurs very close to the RSE point maximizing its R_2 coordinate in Fig. 1. As noted earlier, the USRSE point having the maximum distance R_2 away from the R_1-axis in Fig. 1(b) has the speed $\Omega_{RSE} \cdot |R_2|_{\max} \cong v_1$=1st cosmic speed (for the USRSE with T_{RSE}=4.22 min and $\tilde{K} = 1/4$, see Sec. 2.3) Thus, the USRSE loop in Fig. 1(b) can be used for launching satellites. Such a satellite would be carried from the surface of the Earth by a sliding climber. Because of the friction, the climber would eventually stop close to the USRSE point having the maximum distance away from the R_1-axis in Fig. 1(b). At this point, the stopped climber rotates with the RSE with the speed $\cong v_1$=1st cosmic speed. Thus, the climber can simply release the carried satellite directly into a nearly circular low Earth orbit.

For concreteness, in the discussions of this chapter, we commonly assumed that the RSE or USRSE bottom point is on the surface of the Earth. The air-resistance (ignored in our discussions) would certainly tend to slow down the RSE rotation. This effect can be compensated simply by applying an external torque, say, close to the RSE tying point to the Earth. The air resistance will also tend to slow the sliding climbers carrying space-crafts for launching. However, this effect may be not so significant because the climbers' velocity is small in the initial stage of their travel while they still move through the dense atmospheric level. Moreover, the RSE concept itself provides some radical solutions that can be used to diminish the air resistance (if needed). For example, by using differential Eq. (8'''), the USRSE loops can be designed with their bottoms anywhere above the Earth surface, e.g., above the dense atmospheric layer, to diminish air-resistance.

2.7 Summary

In summary, the RSEs are rapid outer space transportation systems that require no internal engines for the climbers sliding along the elevator strings. RSE strings exhibit interesting nonlinear dynamics and statistical physics phenomena. RSEs' action fundamentally employs truly basic natural phenomena -- gravitation and inertial forces, not more than that. Satellites and spacecrafts carried by sliding climbers can be released (launched) along RSEs. RSE strings can host space stations and research posts. Sliding climbers can be then used to transport useful loads and humans from the Earth to these outer space locations.

2.8 References

[1] *"Statistical Mechanics of Membranes and Surfaces"*, edited by D. R. Nelson, T. Piran, and S. Weinberg (World Scientific, 1988); D. R. Nelson, *"Defects and Geometry in Condensed Matter Physics"* (Cambridge, 2002), see Ch. 5.

[2] M. Kardar, *"Statistical Physics of Fields"* (Cambridge, 2007).

[3] L. Golubović, D. Moldovan, and A. Peredera, Phys. Rev. Lett. **81** (1998) 3387 ; L. Golubović, D. Moldovan, and A. Peredera, Phys. Rev. E **61** (2000) 1703; D. Moldovan and L. Golubović, Phys. Rev. Lett. **82** (1999) 2884 ; D. Moldovan and L. Golubović, Phys. Rev. E **60** (1999) 4377.

[4] B. Maier and J. O. Rädler, Phys. Rev. Lett. **82** (1999) 1911; M. B. Hochrein, J. A. Leierseder , L. Golubović , and J. O. Rädler, Phys. Rev. Lett. **96** (2006) 038103.

[5] For an extensive review, see B. C. Edwards, and E. A. Westling, *"The Space Elevator: A Revolutionary Earth-to-Space Transportation System"* (BC Edwards, 2002). See also, V. Lvov, Science **158** (1967) 946.

[6] J. Pearson, Acta Astronautica **2** (1975) 785.

[7] A. C. Clarke, *"The Fountains of Paradise"* (Harcourt Brace Jovanovich, 1978).

[8] A. C. Clarke, "The Space Elevator: 'Thought Experiment' or Key to the Universe?", in *Advanced Earth Oriented Applied Space Technology,* Vol. **1**, 39 (Pergamon Press, London, 1981).

[9] L. D. Landau and E. M. Lifshitz, *"Mechanics"*, Course in Theoretical Physics, Vol. 1 (Pergamon Press, London, 1976), Ch. VI. 39.

[10] L. Golubović, and S. Knudsen, Europhys. Lett. **86,** 34001 (2009).

[11] M.F. Yu *et al.*, Phys. Rev. Lett. **84**(2000) 5552; M.F. Yu *et al.*, Science **287**(2000) 637. See also, http://en.wikipedia.org/wiki/Carbon_nanotube.

[12] See the studies in [3] for discussions of the buckling dynamics of semi-flexible strings (polymers) and membranes under negative tension (compression).

[13] J. S. Sprott, *"Chaos and Time-Series Analysis"* (Oxford, 2008).

Appendix A: Fast and slow inertial forces in double rotating frame

In this appendix, we discuss the form of inertial forces experienced in the (natural for the RSE) *double rotating frame* (DRF). The DRF is obtained from the geosynchronous (single rotating) frame by adding to it the rotation around the R_1-axis in Figs. 1(a) and (b). See also the figure A1 in this Appendix. The angular velocity of the DRF is thus

$$\vec{\Omega}(t) = \vec{\Omega}_{RSE} + \vec{\Omega}_{earth}(t). \tag{A1}$$

Here, $\vec{\Omega}_{RSE} = \Omega_{RSE}\hat{e}_1$ corresponds to the rotation around the R_1-axis, whereas $\vec{\Omega}_{earth}(t)$ is Earth angular velocity vector which in the DRF rotates with the angular velocity $-\Omega_{RSE}$ (and thus acquires a time-dependence, as shown below), see Fig. A1. We will show here that, with the $\vec{\Omega}(t)$ in Eq. (A1), the Eq. (3) yields the Eq. (4) of Ch. 2, i.e.,

$$\vec{a}_{inert} = -\frac{\partial \Phi_{inert}}{\partial \vec{R}} + \vec{a}_{res}\,, \tag{A2}$$

with (as stated in Eq. (5) of Ch. 2)

$$\Phi_{inert}(\vec{R}) = -\frac{1}{2}\Omega_{earth}^2 R_1{}^2 - \frac{1}{2}(\Omega_{RSE}^2 + \frac{1}{2}\Omega_{earth}^2)(R_2^2 + R_3^2)\,, \tag{A3}$$

being a *time-independent* effective potential generating inertial forces sensed in the DRF. As displayed in our equations below, the residual, $\vec{a}_{res}$ term in Eq. (4), i.e. (A2), includes velocity dependent terms that vanish for an object *at rest in the DRF,* as well as *fast time-dependent* oscillatory terms of $\vec{a}_{inert}$ (with frequencies Ω_{RSE} and $2\Omega_{RSE}$) that have *zero* time average over one RSE period ($T_{RSE} = 2\pi/\Omega_{RSE}$). To derive the above important results, we will combine Eq. (A1) with Eq. (3) of Ch. 2, i.e.,

$$(\vec{a}_{inert})_{DRF} = \vec{\Omega}(t)\times(\vec{R}\times\vec{\Omega}(t)) + \vec{R}\times\frac{d\vec{\Omega}(t)}{dt} + \frac{d\vec{R}}{dt}\times 2\vec{\Omega}(t). \tag{A4}$$

In Eq. (A1), as noted above,

$$\vec{\Omega}_{RSE} = \Omega_{RSE}\hat{e}_1\,, \tag{A5}$$

whereas

$$\vec{\Omega}_{earth}(t) = \Omega_{earth} \cos(\Omega_{RSE} t)(\hat{e}_2)_{DRF} - \Omega_{earth} \sin(\Omega_{RSE} t)(\hat{e}_3)_{DRF} \ , \qquad \text{(A6)}$$

as can be easily deduced from Fig. A1. In the figure, as well as in the equations displayed here, the unit vectors associated with the thee axis of DRF are labeled as

$$(\hat{e}_1)_{DRF},\ (\hat{e}_2)_{DRF},\ (\hat{e}_3)_{DRF} \ , \qquad \text{(A7)}$$

whereas the unit vectors associated with the thee axis of ordinary geo-synchronous frame (rotating with Earth) are labeled simply as

$$\hat{e}_1,\ \hat{e}_2\ ,\ \hat{e}_3\ . \qquad \text{(A8)}$$

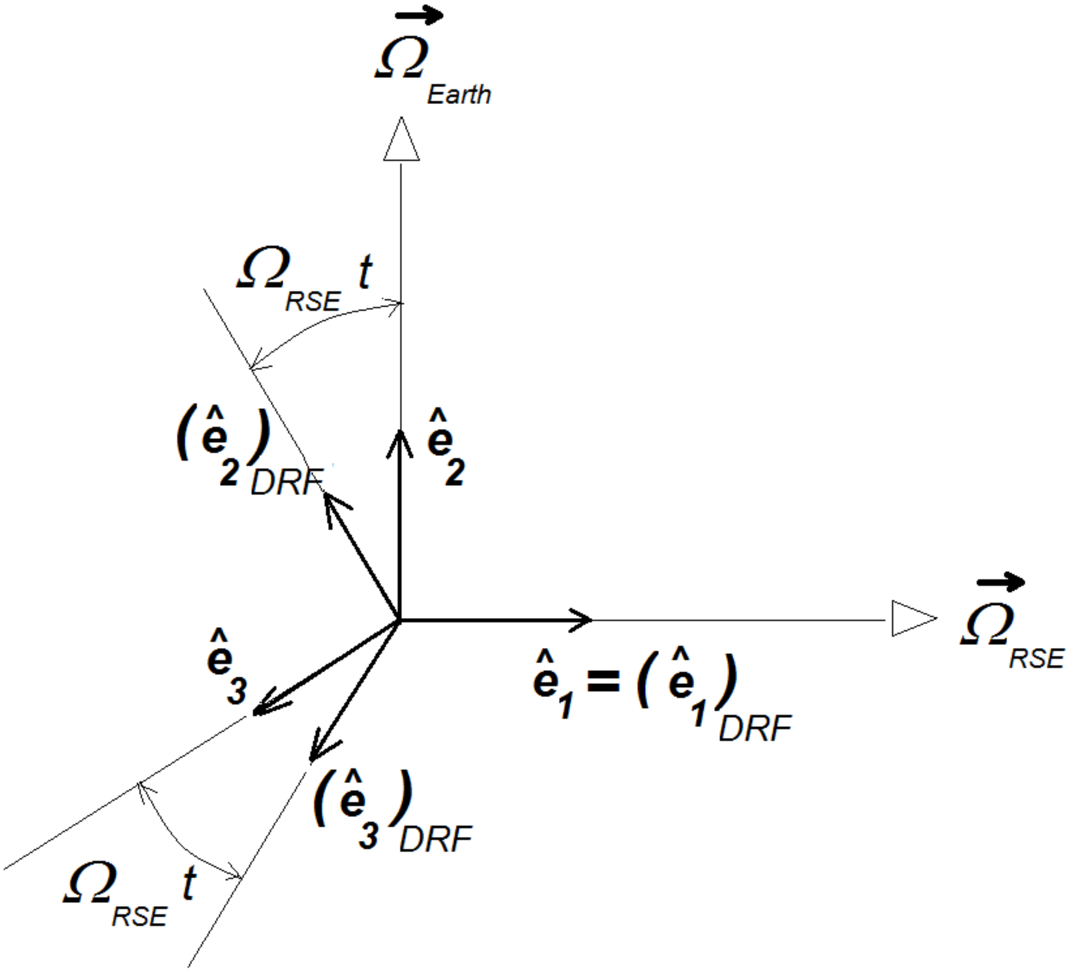

Fig. A1: Geo-synchronous frame versus double rotating frame (DRF). See the text for the notation used in the figure. Note that the two frames have the common axis 1, whereas the axes 2 and 3 of the DRF rotate relative to the axes 2 and 3 of the geo-synchronous frame.

We note that, in Eqs. (A4), as well as in Eq. (A3), the position vector is expressed in terms of its components in the DRF frame, that is,

$$\vec{R} = R_1(\hat{e}_1)_{DRF} + R_2(\hat{e}_2)_{DRF} + R_3(\hat{e}_3)_{DRF} \ . \qquad \text{(A9)}$$

Combining Eqs. (A1), (A5), (A6) with Eq. (A4), yields (after a longer algebra) the major result stated in Eq. (A2) [i.e., Eq. (4) of Ch. 2]. It has the form,

$$(\vec{a}_{inert})_{DRF} = (\vec{a}_{inert})_{slow} + \vec{a}_{res} \, , \qquad \text{(A2')}$$

with

$$\begin{aligned}(\vec{a}_{inert})_{slow} &= -\frac{\partial \Phi_{inert}}{\partial \vec{R}} \\ &= \Omega^2_{earth} R_1 \ (\hat{e}_1)_{DRF} + \left(\Omega^2_{RSE} + \frac{\Omega^2_{earth}}{2} \right) R_2 \ (\hat{e}_2)_{DRF} + \left(\Omega^2_{RSE} + \frac{\Omega^2_{earth}}{2} \right) R_3 \ (\hat{e}_3)_{DRF} \end{aligned} \ ,$$

(A10)

whereas the residual, $\vec{a}_{res}$ term in Eq. (A2) [i.e., Eq. (4) of Ch. 2] has the form,

$$\vec{a}_{res} = a_{res,1}(\hat{e}_1)_{DRF} + a_{res,2}(\hat{e}_2)_{DRF} + a_{res,3}(\hat{e}_3)_{DRF} \ . \qquad \text{(A11)}$$

In Eq. (A11),

$$a_{res,1} = a_{res,1}{}^0 + a_{res,1}{}^1 + a_{res,1}{}^2 \qquad \text{(A12)}$$

With

$$a_{res,1}{}^0 = -2\Omega_{earth}[\sin(\Omega_{RSE}t)\dot{R}_2 + \cos(\Omega_{RSE}t)\dot{R}_3] \qquad \text{(A12a)}$$

$$a_{res,1}{}^1 = -2\Omega_{RSE}\Omega_{earth}[\cos(\Omega_{RSE}t)R_2 - \sin(\Omega_{RSE}t)R_3] \qquad \text{(A12b)}$$

$$a_{res,1}{}^2 = 0 \qquad \text{(A12c)}$$

while,

$$a_{res,2} = a_{res,2}{}^0 + a_{res,2}{}^1 + a_{res,2}{}^2 \qquad \text{(A13)}$$

with,

$$a_{res,2}{}^{0} = 2\Omega_{earth}\sin(\Omega_{RSE}t)\dot{R}_1 + 2\Omega_{RSE}\dot{R}_3 \tag{A13a}$$

$$a_{res,2}{}^{1} = 0 \tag{A13b}$$

$$a_{res,2}{}^{2} = \frac{\Omega_{earth}^2}{2}[-\cos(2\Omega_{RSE}t)R_2 + \sin(2\Omega_{RSE}t)R_3] \tag{A13c}$$

and, finally,

$$a_{res,3} = a_{res,3}{}^{0} + a_{res,3}{}^{1} + a_{res,3}{}^{2} \tag{A14}$$

with,

$$a_{res,3}{}^{0} = 2\Omega_{earth}\cos(\Omega_{RSE}t)\dot{R}_1 - 2\Omega_{RSE}\dot{R}_2 \tag{A14a}$$

$$a_{res,3}{}^{1} = 0 \tag{A14b}$$

$$a_{res,3}{}^{2} = \frac{\Omega_{earth}^2}{2}[\sin(2\Omega_{RSE}t)R_2 + \cos(2\Omega_{RSE}t)R_3]\,. \tag{A14c}$$

By inspecting the Eqs. (A12) through (A14), we see that the residual, $\vec{a}_{res}$ term in Eq. (4), i.e. (A2), includes: (i) velocity dependent terms that vanish for an object *at rest in the DRF; (ii) fast explicitly time-dependent* oscillatory terms (with frequencies Ω_{RSE} and $2\Omega_{RSE}$) that have *zero* time average over one RSE period ($T_{RSE} = 2\pi/\Omega_{RSE}$). For the here interesting situations with $\Omega_{RSE} >> \Omega_{earth}$ [$T_{RSE} \sim 10\min << T_{earth} = 2\pi/\Omega_{earth} = 1$ sidereal day], the fast terms are expected to average out, so the slow potential term displayed in (A10) dominates over the $\vec{a}_{res}$ term displayed in the Eqs. (A11) though (A14).

This expectation is corroborated by our numerical simulations of RSE dynamics discussed in Chapter 2 [see Sec. 2.5]. Here, it is relevant to recall that the RSE structure is designed by using the magical mass distribution (line density) introduced in Ch. 2 [see Eq. (8) in Sec. 2.2 and appendix B]. It ensures the exact equilibrium between the slow inertial forces [induced by the slow inertial acceleration in Eq. (A10)] and the gravitational forces acting on mass elements of the RSE. The $\vec{a}_{res}$ displayed in Eqs. (A11) through (A14) induces very small oscillations around this equilibrium. By Eqs. (A11) through (A14), the time periods of these forced small oscillations are = T_{RSE} and $T_{RSE}/2$. From Eq. (A12b) we see that the inertial force drives the oscillations with the period =T_{RSE}. By the Eq. (A12b) we can however see that this driving force vanishes for $R_2=0$ and $R_3=0$, that is, along the R_1 axis. Thus, this acceleration is significant for the RSE points which are away from the RSE axis of internal rotation [which nearly coincides with the R_1 axis due to smallness of the top displacements seen in Figs. 4(b) and 7]. Thus, the oscillations with the period=T_{RSE} are the strongest at the RSE point with the maximum value of R_2 in Fig. 1 of Ch. 2. For the case of the elliptic RSE in Fig. 1(a), this is the midpoint of the RSE. Recall of the Fig. 8 in Ch. 2, in which display the $R_1(t)$ of a RSE point on the elliptic RSE with T_{RSE} = 10.83 min. The presence of the oscillations with the 10.83 min period is well visible in this figure. RSE points oscillate with the same period by amplitudes roughly proportional to their distance away from the R_1 axis. Due to this feature, the RSE deforms somewhat like an object under a periodic shear stress, see Fig. 8(a) of Ch. 2.

These fast oscillations of the RSE shape are weak. A consequence of this is the nearly periodic climber dynamics on the RSE seen in Fig. 2 of Ch. 2. It can be understood by assuming a constant RSE shape, and by ignoring the fast inertial forces in Eqs. (A11) through (A14); see Sec. 2.4 and Appendix D. Main features of the climber dynamics can be understood purely in terms of the slow inertial forces and the gravitational force both encoded in the effective potential in Eq. (7) of chapter 2.

From our discussions, it is clear that the DRF has the upmost conceptual significance for understanding the RSE actions and behavior, both in terms of its shape stability and its ability to support the climbers motion. It is instructive to note that the DRF naturally reduces to the standard geo-synchronous frame in the limit $\Omega_{RSE}=0$, see Fig. A1. In this limit, the DRF inertial acceleration Eq. (A2′) [displayed in Eqs. (A10) through (A14)] reduces to the common geo-synchronous frame inertial acceleration,

$$\vec{a}_{inert} = \Omega^2_{earth}(R_1\ \hat{e}_1 + R_3\ \hat{e}_3) + 2\Omega_{earth}(-\dot{R}_3\ \hat{e}_1 + \dot{R}_1\ \hat{e}_3)\ . \tag{A15}$$

Here, the first term is the standard centrifugal acceleration whereas the second term is the standard Coriolis acceleration due to earth rotation. We recall that the figures displayed in Ch. 2 depict the simulations results as seen in the geo-synchronous frame. However, we did most of our simulations both in the geo-synchronous frame [whence the inertial acceleration in Eq. (A15) applies], and, to check our results, also in the DRF [whence the inertial acceleration has the form as in Eq. (A2′)]. These two frames are related by the simple rotation seen in Fig. A1, so it is easy to relate the RSE configuration as seen in the geo-synchronous frame to the same configuration as seen in the DRF.

Appendix B: Magical mass distribution: Continuum form

In Sec. 2.2, we anticipated that the time independence of the effective potential Φ_{eff} in Eq. (7) allows one to find a magical mass distribution $\mu(s)$ with which the RSE string will *indefinitely* maintain its initial shape by remaining at rest *in* the Double Rotating Frame (DRF). In this appendix, we derive and solve differential equations governing tension $T(s)$ and mass line density $\mu(s)$ of a RSE of a given shape. The result will be the magical continuum mass line density $\mu(s)$ in Eq. (8), i.e.,

$$\ln\left[\frac{\mu(s)}{\mu(0)}\right]=-\int_0^s ds'\ \frac{(\vec{a}_{net}\cdot\hat{t})_{s'}}{K(s')}+\ln\left[\frac{K(s=0)}{K(s)}\right] \tag{B1}$$

With

$$K(s)=-\frac{(\vec{a}_{net}\cdot\hat{n})_s}{C(s)}=\frac{T(s)}{\mu(s)} \tag{B2}$$

Eqs. (B1) and (B2) apply for the case of a planar RSE specified by a 2-d curve $\vec{R}(s)=[R_1(s),R_2(s),R_3(s)=0]$ depicted in Fig. B1.

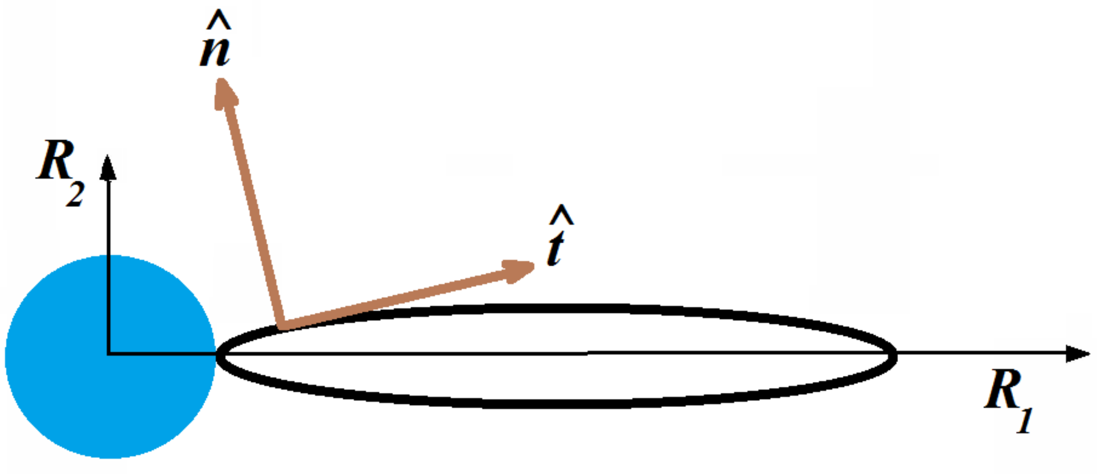

Fig. B1: Geometry of planar RSE string in Double Rotating Frame.

In Eqs. (B1) and (B2), the *C(s)* is the local string curvature, while the 2-d vector

$$\vec{a}_{net} = -\frac{\partial \Phi_{eff}}{\partial \vec{R}} = \left(-\frac{\partial \Phi_{eff}}{\partial R_1}, -\frac{\partial \Phi_{eff}}{\partial R_2} \right), \tag{B3}$$

is evaluated from the effective potential Eq. (7) at the RSE point $[R_1(s), R_2(s)]$,

$$\Phi_{eff}(\vec{R}) = \Phi_{grav}(\vec{R}) + \Phi_{inert}(\vec{R}) = -G\frac{M_{earth}}{\sqrt{R_1^2 + R_2^2}} - \frac{1}{2}\Omega_{earth}^2 R_1^{\ 2} - \frac{1}{2}(\Omega_{RSE}^2 + \frac{1}{2}\Omega_{earth}^2)R_2^2 \quad . \tag{B4}$$

To derive Eqs. (B1) and (B2), we consider an RSE which is in equilibrium, i.e., at rest in DRF in the presence of gravitational and slow inertial forces [see Eq. (A10)] both encoded in the effective potential. For this steady RSE state, in Eq. (1) of Ch. 2 one has $\partial^2 \vec{R} / \partial t^2 = 0$ while the $\vec{f}_{ext}$ is given by Eq. (6). Thus, Eq. (1) yields,

$$0 = \frac{\partial}{\partial s} T(s) \frac{\partial}{\partial s} \vec{R} + \mu(s)\, \vec{a}_{net}, \tag{B5}$$

i.e., $0 = \frac{\partial}{\partial s}[T(s)\hat{t}(s)] + \mu(s)\, \vec{a}_{net}$ (B6)

with $\hat{t}(s) = \partial \vec{R} / \partial s$, the tangent unit vector making an angle $\theta(s)$ with the $R_1 -$ axis , see Fig. B1. Thus, $\hat{t}(s) = [\cos(\theta(s)), \sin(\theta(s))]$. By Eq. (B6),

$$0 = \frac{\partial T}{\partial s}\hat{t} + T\frac{\partial \hat{t}}{\partial s} + \mu(s)\, \vec{a}_{net} \,. \tag{B7}$$

For the planar RSE string, it will be convenient to introduce the normal unit vector $\hat{n}(s) = [-\sin(\theta(s)), \cos(\theta(s))]$ perpendicular to the string, i.e., to $\hat{t}(s)$, see Fig. B2. By noting that

$$\frac{\partial \hat{t}(s)}{\partial s} = [-\sin(\theta), \cos(\theta)]\frac{\partial \theta}{\partial s} = C\,\hat{n},$$

with

$$C = \frac{\partial \theta}{\partial s} \ ,$$

the local string curvature, Eq. (B7) reduces to

$$0 = \frac{\partial T}{\partial s}\hat{t} + TC\hat{n} + \mu(s)\,\vec{a}_{net} \, . \tag{B8}$$

Using $\hat{t}^2 = \hat{n}^2 = 0, \ \hat{t} \cdot \hat{n} = 0,$ Eq. (B8) is easily projected onto the $\hat{t}$ and $\hat{n}$ directions to yield,

$$\frac{dT}{ds} + \mu(\vec{a}_{net} \cdot \hat{t}) = 0 \ , \tag{B9}$$

and

$$T \cdot C + \mu(\vec{a}_{net} \cdot \hat{n}) = 0 \, . \tag{B10}$$

By rearrangement of equation (B10),

$$\mu = -T \frac{C}{(\vec{a}_{net} \cdot \hat{n})} \, . \tag{B11}$$

Eqs. (B11) and (B9) yield the differential equation for the tension field,

$$\frac{dT(s)}{ds} - T(s)\,C(s)\left(\frac{(\vec{a}_{net} \cdot \hat{t})}{(\vec{a}_{net} \cdot \hat{n})}\right)_s = 0 \, , \tag{B12}$$

equivalent to the equation,

$$\frac{d}{ds}\ln(T(s)) = C(s)\left(\frac{(\vec{a}_{net} \cdot \hat{t})}{(\vec{a}_{net} \cdot \hat{n})}\right)_s = \Psi(s) \, , \tag{B13}$$

which is easily integrated,

$$\ln\left(\frac{T(s)}{T(0)}\right) = \int_0^s ds'\,\Psi(s') \ . \tag{B14}$$

Thus, we obtain the RSE tension field in the form,

$$\frac{T(s)}{T(0)} = \exp\left[\int_0^s ds' C(s') \left(\frac{(\vec{a}_{net} \cdot \hat{t})}{(\vec{a}_{net} \cdot \hat{n})} \right)_{s'} \right] . \tag{B15}$$

The line mass density is now simply obtained from (B11) and (B15) as

$$\mu(s) = -\frac{C(s)}{\left(\vec{a}_{net} \cdot \hat{n}\right)_s} T(s=0) \exp\left[\int_0^s ds' C(s') \left(\frac{(\vec{a}_{net} \cdot \hat{t})}{(\vec{a}_{net} \cdot \hat{n})} \right)_{s'} \right]. \tag{B16}$$

By Eq. (B11),

$$\mu(0) = \mu(s=0) = -\frac{C(s=0)}{\left(\vec{a}_{net} \cdot \hat{n}\right)_{s=0}} T(s=0) , \tag{B17}$$

so the continuum solution for the magical line mass density can be written

$$\frac{\mu(s)}{\mu(0)} = \exp\left[\int_0^s ds' C(s') \left(\frac{(\vec{a}_{net} \cdot \hat{t})}{(\vec{a}_{net} \cdot \hat{n})} \right)_{s'} \right] \frac{\dfrac{C(s)}{\left(\vec{a}_{net} \cdot \hat{n}\right)_s}}{\dfrac{C(s=0)}{\left(\vec{a}_{net} \cdot \hat{n}\right)_{s=0}}} . \tag{B18}$$

By introducing the quantity,

$$K(s) = -\frac{(\vec{a}_{net} \cdot \hat{n})_s}{C(s)} , \tag{B19}$$

Eq. (B18) can be rewritten as,

$$\frac{\mu(s)}{\mu(0)} = \exp\left[\int_0^s ds' C(s') \left(\frac{(\vec{a}_{net} \cdot \hat{t})}{(\vec{a}_{net} \cdot \hat{n})} \right)_{s'} \right] \frac{K(s=0)}{K(s)} , \tag{B20}$$

Eq. (B20) is easily seen to be equivalent to Eq. (B1), i.e., Eq. (8) of chapter 2. By Eqs. (B19) and (B11), it is also easy to see that

$$K(s) = \frac{T(s)}{\mu(s)} , \tag{B21}$$

as stated in Eq. (B2), i.e., Eq. (8′) of chapter 2. This completes our derivation of Eqs. (8) and (8′). We would like to stress that the quantity *K(s)* is simply proportional to the local tensile stress *p(s)=T(s)/A(s),* with *A(s)* the local cross-sectional area of the RSE string. Indeed, by noting that $\mu(s) = \rho A(s)$, with ρ, the density of the RSE material, Eq. (B21) implies

$$K(s) = \frac{p(s)}{\rho}, \tag{B22}$$

as stated in Eq. (8′′) of chapter 2. Note that, by Eqs. (B22) and (B2),

$$p(s) = K(s)\rho = -\frac{(\vec{a}_{net} \cdot \hat{n})_s}{C(s)}\rho \quad . \tag{B23}$$

Thus, the local tensile stress *p(s)* depends only on the local string geometrical details $[C(s), \hat{n}(s)]$ and the local value of the acceleration $\vec{a}_{net}(\vec{R}(s))$.

Appendix C: Magical mass distribution: Its discretized form and Hookean spring & bead finite element model for RSE

In this appendix we describe the discretized model for RSE dynamics used in our numerical simulations. We model the RSE as a chain of massive beads tethered by massless Hookean springs. In a non-inertial frame, the Newtonian equation of motion of the n-th bead, with the position $R_n(t)$ and mass m_n has the form,

$$m_n \frac{d^2\vec{R}_n}{dt^2} = T_n\hat{t}_n - T_{n-1}\hat{t}_{n-1} + m_n(\vec{a}_n^{(inert)} + \vec{a}_n^{(grav)}) , \tag{C1}$$

with $a_n^{(inert)}$ discussed in appendix A and,

$$\vec{a}_n^{(grav)}(\vec{R}_n) = -\frac{GM_{earth}\vec{R}_n}{|\vec{R}_n|^3} . \tag{C2}$$

In Eq. (C1), $\hat{t} = (\vec{R}_{n+1} - \vec{R}_n)/|\vec{R}_{n+1} - \vec{R}_n|$ and T_n is the tension force in the n-th Hookean spring,

$$T_n = B_n\left\{|\vec{R}_{n+1} - \vec{R}_n| - r_n\right\}. \tag{C3}$$

Here, B_n is the spring constant and r_n is the relaxed spring length. The values of m_n and the spring parameters (B_n , r_n) are discussed in the following.

Initial positions of the massive beads, $\vec{R}_n(t=0)$ are set to be along the planar RSE lines in Fig. 1. In the spirit of appendix B, the discretized RSE will be designed with “magical” masses m_n such that the RSE is in equilibrium, i.e., at rest in DRF under the influence of the gravitational and slow inertial forces [see Eq. (A10)]. Thus, by Eq. (C1) with $d^2\vec{R}_n/dt^2 = 0$,

$$0 = T_n\hat{t}_n - T_{n-1}\hat{t}_{n-1} + m_n(\vec{a}_n)_{net} . \tag{C4}$$

Here, as in Eq. (B3) of appendix B,

$$(\vec{a}_n)_{net} = -\frac{\partial \Phi_{eff}}{\partial \vec{R}}\bigg|_{\vec{R}=\vec{R}_n(0)} \quad , \tag{C5}$$

where Φ_{eff} is the effective potential displayed in Eq. (B4). It encodes gravitational and slow inertial acceleration. We note that Eq. (C4) is a discretized analog of the equation (B6) for the continuum RSE model. Much like the Eq. (B6), the equation (C4) can be solved for magical masses m_n and tensions T_n. To end this, we first write the acceleration vector in terms of its 2-d components,

$$(\vec{a}_n)_{net} = (\vec{a}_n)_1 \hat{e}_1 + (\vec{a}_n)_2 \hat{e}_2 \quad . \tag{C6}$$

To proceed, we introduce "co-acceleration" vectors defined via,

$$\vec{A}_n = -(\vec{a}_n)_2 \hat{e}_1 + (\vec{a}_n)_1 \hat{e}_2 \quad . \tag{C7}$$

Note that the co-acceleration and acceleration vectors are perpendicular to each other,

$$\vec{A}_n \cdot (\vec{a}_n)_{net} = 0 \, . \tag{C8}$$

Multiplying the vector equation (C4) by the co-acceleration vector and using Eq. (C8) yields the relation,

$$T_n = T_{n-1} \frac{\hat{t}_{n-1} \cdot \vec{A}_n}{\hat{t}_n \cdot \vec{A}_n} \quad . \tag{C9}$$

Next, we multiply the vector equation (C4) by the acceleration vector and solve it for the bead magical mass m_n . With the assistance of Eq. (C9), we finally obtain,

$$m_n = \frac{T_{n-1}}{|(\vec{a}_n)_{net}|^2} \cdot \frac{(\hat{t}_n \cdot \vec{A}_n)(\hat{t}_{n-1} \cdot (\vec{a}_n)_{net}) - (\hat{t}_n \cdot (\vec{a}_n)_{net})(\hat{t}_{n-1} \cdot \vec{A}_n)}{\hat{t}_n \cdot \vec{A}_n} \quad . \tag{C10}$$

The pair of equations Eqs. (C9) and (C10) constitute a marching algorithm for determining magical masses m_n and initial (at $t=0$) tensions T_n along the RSE for given initial positions of the massive beads, $\vec{R}_n(t=0)$. To determine the Hookean spring parameters in Eq. (C3), we assume that the n-th spring is stretched by a small fraction δ_n of its relaxed length, that is,

$$|\vec{R}_{n+1}(0)-\vec{R}_n(0)| = r_n + \delta_n r_n = (1+\delta_n) r_n \,. \tag{C11}$$

By Eqs. (C11) and (C3), we obtain the spring parameters as,

$$r_n = \frac{|\vec{R}_{n+1}(0)-\vec{R}_n(0)|}{1+\delta_n} \,, \tag{C12}$$

and,

$$B_n = \frac{T_n}{\delta_n r_n} = \frac{(1+\delta_n)}{\delta_n} \frac{T_n}{|\vec{R}_{n+1}(0)-\vec{R}_n(0)|} \,. \tag{C13}$$

In our simulations, we used stiff Hookean springs with a small values of δ_n such as $\delta_n = 10^{-2}$ or $\delta_n = 10^{-3}$. In this stiff spring limit, our results were found to be largely independent on the actual value of δ_n.

Appendix D: Minimal RSE angular velocity for climbing

In this appendix, we discuss in more detail analytic predictions on sliding climber motion based on the simple conservation law in Eq. (9) of Ch. 2. We also outline the derivation of Eq. (10) giving the minimal RSE angular velocity $\Omega_{\min}$ needed to have the climbers sliding from the Earth *(*at *s=0)* to remote outer space locations along the RSE arc-length *s*. In the context of Eq. (9), that is,

$$\frac{1}{2}\left(\frac{ds(t)}{dt}\right)^2 + \Phi_{eff}[\vec{R}(s(t))] = const. \qquad \text{(D1)}$$

the climber motion is isomorphic to familiar conservative 1-d dynamics (along the arc-length *s*) of a particle with the position *s(t)* in the potential seen by the climber, $U(s) = \Phi_{eff}(\vec{R}(s))$. It is thus in principle possible to qualitatively discuss the climbers motion. To end this, we first need to obtain the form of $U(s) = \Phi_{eff}(\vec{R}(s))$. The RSE is nearly planar in DRF, i.e., it is specified by a 2-d curve $\vec{R}(s) = [R_1(s), R_2(s), R_3(s) = 0]$ as depicted in Fig. B1 of appendix B. The effective potential at a RSE point is given by Eq. (B4) of appendix B, so the potential seen by the climber is,

$$U(s) = \Phi_{eff}(\vec{R}(s)) = -G\frac{M_{earth}}{\sqrt{(R_1(s))^2 + (R_2(s))^2}} - \frac{1}{2}\Omega_{earth}^2 (R_1(s))^2 - \frac{1}{2}(\Omega_{RSE}^2 + \frac{1}{2}\Omega_{earth}^2)(R_2(s))^2 .$$

(D2)

Here, R_1 and R_2 need to be expressed as functions of the arc-length *s*. It can be done numerically for any given shape of RSE. In figure D1, we plot thus obtained form of *U(s)* for an elliptic RSE, for two different angular velocity Ω_{RSE} of the RSE. At the *higher* Ω_{RSE} in Fig. D1 (upper panel), the *U(s)* has an unstable maximum at *s=0* (i.e., at the Earth surface). Thus, by Eq. (D1) and Fig. D1 (upper panel), a climber starting at rest close to Earth (at $s = s_{earth} \approx 0$) will oscillate between its starting position and another turning point (at $s = s_{space}$) which is deep in the outer space [$U(s_{earth}) = U(s_{space})$; see also figure 1(a)]. On the other side, at the *lower* Ω_{RSE} in Fig. D1 (lower panel), the *U(s)* has a stable minimum at *s=0* (i.e., at the Earth surface). Thus, by Eq. (D1) and

Fig. D1, a climber starting at rest close enough to Earth will remain close to the Earth by executing small oscillations about *s=0*. The figure D1 thus evidences the existence of a minimal RSE angular velocity $\Omega_{\min}$ needed to have the climbers sliding from the Earth *(s=0)* to remote outer space locations.

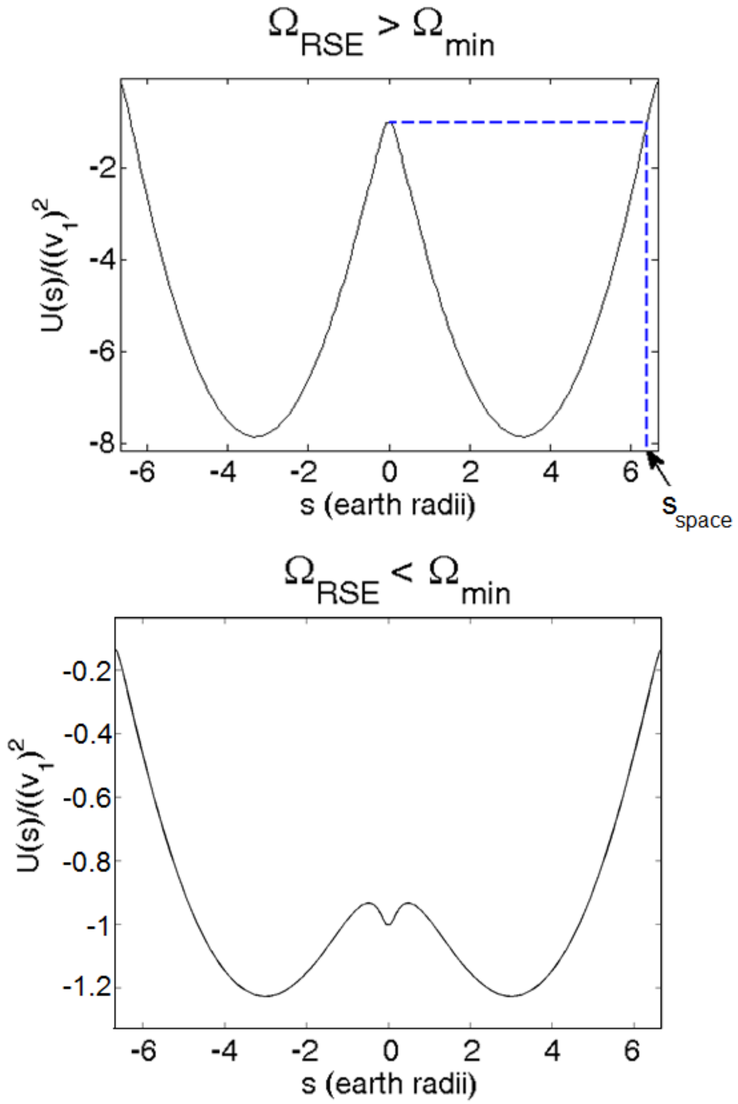

Fig. D1: The potential *U(s)* seen by a climber on the elliptic RSE with major semi-axis a =3.2107 R_{earth} and minor semi-axis b= 0.5 R_{earth}. For this RSE, equation (D11) predicts Ω_{min}= 3.72 v_1/R_{earth} . Upper panel gives the *U(s)* for Ω_{RSE}= 7.8 v_1/R_{earth}. Lower panel gives the *U(s)* for Ω_{RSE}= 2.8 v_1/R_{earth}.

Such an $\Omega_{\min}$ exists in any RSE (in particular, also in the USRSE, as noted in Ch. 2). To show this and calculate $\Omega_{\min}$ we consider the potential in Eq. (D2) around *s=0*. For a small arc-length *s*, the RSE shape is nearly parabolic (see Fig. 1), and one has the expansions,

$$R_2(s) = s + O(s^3)\ , \tag{D3}$$

$$R_1(s) = R_{earth} + \frac{C}{2}s^2 + O(s^4)\,, \tag{D4}$$

with *C* labeling the magnitude of the RSE curvature at *s=0*. Next, we insert the expansions in Eqs. (D3) and (D4) into Eq. (D2) and expand it in powers of *s*. Thus we find,

$$U(s) = \Phi_{eff}(\vec{R}(s)) = U(0) + \frac{1}{2}U''(0)\ s^2 + O(s^4)\,, \tag{D5}$$

with,

$$U''(0) = \Omega_{\min}^2 - \Omega_{RSE}^2\,. \tag{D6}$$

Here,

$$\Omega_{\min}^2 = \frac{\dfrac{GM_{earth}}{R_{earth}}(1+CR_{earth}) - (R_{earth}\Omega_{earth})^2(\dfrac{1}{2}+CR_{earth})}{R_{earth}^2}\ . \tag{D7}$$

Note that $U''(0)$ in Eq. (D5) changes sign when the Ω_{RSE} crosses $\Omega_{\min}$, marking the transition from two shapes of $U(s)$ displayed in Fig. D1. Thus, the $\Omega_{\min}$ in Eq. (D7) is the minimal RSE angular velocity $\Omega_{\min}$ needed to have the climbers sliding from the Earth *(s=0)* to outer space locations. Better sense for the result in Eq. (D7) is gained by introducing the first cosmic speed $v_1 = (GM_{earth}/R_{earth})^{1/2} = 7.89 km/s$ of a satellite in a circular orbit with the radius $= R_{earth}$. In terms of it,

$$\Omega_{\min}^2 = \frac{v_1^2(1+CR_{earth}) - (R_{earth}\Omega_{earth})^2\left(\dfrac{1}{2}+CR_{earth}\right)}{R_{earth}^2}\ . \tag{D8}$$

Thus, we obtain $\Omega_{\min}$ in the form,

$$\Omega_{\min} = \frac{v_1}{R_{earth}}\sqrt{1 + CR_{earth} - \left(\frac{R_{earth}\Omega_{earth}}{v_1}\right)^2\left(\frac{1}{2} + CR_{earth}\right)}. \tag{D9}$$

Next, we note that the speed of a point on the equator, $R_{earth}\Omega_{earth} = 0.463 km/s$, is by the factor of 17.039 smaller than the first cosmic speed $v_1 = 7.89 km/s$. Thus, $(R_{earth}\Omega_{earth}/v_1)^2 = 1/17.039^2 = 3.444\times 10^{-3}$, so to a good approximation one can ignore the effects of the Earth rotation encoded in the second term under the square root in Eq. (D9). Thus, we obtain a simple result for $\Omega_{\min}$, in the form,

$$\Omega_{\min} = \frac{v_1}{R_{earth}}\sqrt{1 + CR_{earth}}\ , \tag{D10}$$

equivalent to our Eq. (10) of chapter 2, by recalling that $C = |C(s=0)|$. For example, for the elliptical RSE as in Fig. 1, with major semi-axis of length *a* and minor semi-axis of length *b*, one has $C = a/b^2$, so Eq. (D10) reduces to,

$$\Omega_{\min} = \frac{v_1}{R_{earth}}\sqrt{1 + \frac{aR_{earth}}{b^2}}\ . \tag{D11}$$

Using Eq. (D11), one can easily understand the potential shapes seen in Fig. D1 (see the figure caption text). As noted in Eq. (10), the result in Eq. (D10) can also be written as

$$\Omega_{\min} = \frac{v_1}{R_{earth}}\sqrt{1 + \frac{1}{\tilde{K}(s=0)}}, \tag{D12}$$

with $\tilde{K}(s) = K(s)/v_1^2$. This follows from Eq. (8′) of Ch. 2, by applying it to the RSE point at *s=0* where $R_1(s=0) = R_{earth}, R_2(s=0) = R_3(s=0) = 0$. At this point $C = |C(s=0)| = -C(s=0)$ and $(\vec{a}_{net}\cdot\hat{n})_{s=0} = GM_{earth}/R_{earth}^2 - \Omega_{earth}^2 R_{earth}$ [see Fig. B1, App. B, for the choice of the direction of the unit vector $\hat{n}$]. Using this in combination with Eq. (8′), yields,

$$K(s=0) = \frac{GM_{earth} / R_{earth}^2 - \Omega_{earth}^2 R_{earth}}{-C(s=0)} = \frac{v_1^2 - (\Omega_{earth} R_{earth})^2}{CR_{earth}} \quad . \tag{D13}$$

By recalling again that $(R_{earth}\Omega_{earth} / v_1)^2 = 1/17.039^2 = 3.444 \times 10^{-3} << 1$, by Eq. (D13) one finds,

$$K(s=0) \approx \frac{v_1^2}{CR_{earth}} \quad . \tag{D14}$$

Hence, $CR_{earth} \approx (K(s=0)/v_1^2)^{-1} = (\tilde{K}(s=0))^{-1}$, and Eq. (D12) follows from Eq. (D10). This observation completes our derivation of Eq. (10) of chapter 2.

Finally, we note that the climbing condition $\Omega_{RSE} \geq \Omega_{\min}$ is equivalent to the condition $T_{RSE} \leq T_{\max} = 2\pi / \Omega_{\min}$. By Eq. (D10),

$$T_{\max} = \frac{T_1}{\sqrt{1 + CR_{earth}}} \quad , \tag{D15}$$

with

$$T_1 = 2\pi R_{earth} / v_1 = 84.49 \min , \tag{D16}$$

being the orbital period of a satellite in a circular orbit with the radius = R_{earth}.

Appendix E: Numerically stable algorithm for time-discretized RSE dynamics

In this appendix we describe the numerically stable algorithm we used to solve the discretized model for RSE dynamics discussed in appendix C. We recall that the RSE is modeled as a chain of massive beads tethered by massless Hookean springs. In a non-inertial frame, the Newtonian equation of motion of the n-th bead has the from as in Eq. (C1). By this equation, in combination with the results for non-inertial frames in App. A, the equation of motion for the bead's position has the general form,

$$\frac{d^2\vec{r}}{dt^2}=\frac{d\vec{r}}{dt}\times\vec{B}+\vec{a}_{other} \quad . \tag{E1}$$

On the right hand side, the velocity dependent term emerges from Coriolis type terms of the inertial acceleration in Eq. (C1); see App. A. It is analogous to familiar Lorentz force acceleration in a magnetic B-field, as suggested by the notation used in Eq. (E1). The second term in Eq. (E1), $\vec{a}_{other}$ contains all other velocity independent contributions that can be expressed as functions of instantaneous beads' positions. To numerically solve the equation (E1) we discretized it in time as follows:

$$\frac{\vec{r}(t+\Delta t)-2\vec{r}(t)+\vec{r}(t-\Delta t)}{(\Delta t)^2}=\frac{\vec{r}(t+\Delta t)-\vec{r}(t-\Delta t)}{2\Delta t}\times\vec{B}+\vec{a}_{other} \ . \tag{E2}$$

In the zero time step limit, $\Delta t \to 0$, Eq. (E2) reduces to Eq. (E1). Note that on the right hand side, we used the simplest *time-step symmetric* discretization for the first time derivative. The use of non-symmetric forms ("right" or "left" first derivatives; see Eq. (E5) below) is problematic because (for any finite Δt) it fails to reproduce the correct motion in non-zero magnetic fields. For example, in a uniform B-field, particles spiral rather than execute the familiar circular (cyclotron) motion. Such numerical pathologies are avoided by using an algorithm which *maps into itself* upon the change of sign of the time step, $\Delta t \to -\Delta t$. It is easy to see that our algorithm in Eq. (E2) has this symmetry property. A simple exercise of analytically solving the difference equation (E2) shows that this time discretization reproduces the well-known circular motion in a uniform B-field even with a finite time step Δt . For this simple exercise, the time step reversal symmetry of the algorithm assures that the eigen-frequencies of the time-discretized dynamics are real. Our actual RSE problem is more complex than this simple exercise because it is non-linear due to the presence of the $\vec{a}_{other}$ term in Eq. (E1). Yet, our extensive tests of the algorithm, done by simulating RSE with various values of Δt, show no sign of any numerical instability.

In practice, the algorithm Eq. (E2) is used to iteratively obtain $\vec{r}(t+\Delta t)$, from the values of the positions at times t and $t-\Delta t$. Fortunately, though not simple, the Eq. (E2) is still only linear in $\vec{r}(t+\Delta t)$ so it can be solved for it. Some complexity however emerges because of having the $\vec{r}(t+\Delta t)$ within the cross product on the right hand side of Eq. (E2). After a lengthy algebra, we obtain a lengthy expression for $\vec{r}(t+\Delta t)$. It turns out that the $\vec{r}(t+\Delta t)$ satisfies the equation,

$$\frac{\vec{r}(t+\Delta t)-2\vec{r}(t)+\vec{r}(t-\Delta t)}{(\Delta t)^2}=\frac{\vec{a}_- -\frac{\Delta t}{2}(\vec{B}\times\vec{a}_-)+\left(\frac{\Delta t}{2}\right)^2\vec{B}(\vec{B}\cdot\vec{a}_-)}{1+\left(\frac{\Delta t}{2}\right)^2(\vec{B})^2}, \tag{E3}$$

with,

$$\vec{a}\_(t)=\vec{v}\_(t)\times\vec{B}(t)+\vec{a}_{other}(t). \tag{E4}$$

where,

$$\vec{v}_-(t)=\frac{\vec{r}(t)-\vec{r}(t-\Delta t)}{\Delta t}. \tag{E5}$$

Note that Eqs. (E2) and (E3) have the same left hand sides. Note however that $\vec{r}(t+\Delta t)$ enters only the left-hand side of Eq. (E3), which is thus trivially solvable for the $\vec{r}(t+\Delta t)$ used in our simulations.

For completeness we briefly outline the idea we used to solve Eq. (E2) for $\vec{r}(t+\Delta t)$ and obtain Eq. (E3). Note that the Eq. (E2) is of the form,

$$\vec{X} + \vec{b} \times \vec{X} = \vec{Y} . \tag{E6}$$

Eq. (E6) can be solved for the vector $\vec{X}$ by looking for it in the form of a linear superposition of the three vectors $\vec{Y}, \vec{b}, \vec{Y} \times \vec{b}$. Using this idea in combination with the familiar vector triple product formula, we obtain,

$$\vec{X} = \frac{\vec{Y} - \vec{b} \times \vec{Y} + \vec{b}\,(\vec{b} \cdot \vec{Y})}{1 + (\vec{b})^2} \ . \tag{E7}$$

This result is used to solve Eq. (E2) for $\vec{r}\,(t + \Delta t)$ and obtain our result in Eq. (E3).

Appendix F: Numerical modeling of climbers' dynamics

Eq. (C1) of Appendix C gives the dynamics of the discretized RSE in the absence of sliding climbers. If a sliding climber is present on the massless bond between adjacent beads at the positions $\vec{R}_{n+1}, \vec{R}_n$, the climber 3d position can be generally expressed as $\vec{R}_{cl} = \vec{R}_n + q_{cl,n} \cdot (\vec{R}_{n+1} - \vec{R}_n)$ where $q_{cl,n}(t)$ is conveniently introduced generalized coordinate; $0 < q_{cl,n}(t) < 1$. With this parametrization, one can directly express the Lagrangian of the RSE+climber system in terms of all beads 3d positions and $q_{cl,n}$. We used the associated second order Euler-Lagrange equations to model the composite RSE+climber system. Special care is however needed to treat the transitions of the climber between adjacent massless bonds when the climber "collides" with the bead at $\vec{R}_n$. After the collision, $q_{cl,n}$ starts at zero. To integrate the second order equation for $q_{cl,n}(t)$ one also needs the value of $\dot{q}_{cl,n}$ just after the collision. It can be obtained by treating the encounter between the climber and the bead as an elastic collision, with bead+climber linear momentum and kinetic energy conserved.

Using these recipes, Dr. Golubovic arrived at a powerful algorithm capable to treat the RSE dynamics with (any number of) sliding climbers. Details of this algorithm as well as more extensive study of climbers' dynamics will be presented in our separate study with Dr. Golubovic [F1]. In this thesis we limited our discussions to the limit of very light climbers which only weakly affect RSE shape. Heavy enough climbers may however cause the shape instabilities of elliptical RSE and USRSE strings [F1]. For the stability, one needs to have a small enough climber to elevator mass ratio [F1].

References to Appendix F:

[F1] Steven Knudsen and Leonardo Golubovic, in preparation.

Chapter 3

Dynamics of Free Rotating Space Elevators

3.1 Introduction

In this chapter we investigate the question: what will happen if one *unties* the bottom of an elliptic rotating space elevator (ERSE) from the Earth, see Fig. 1 here. Such an untied RSE string is essentially completely free and it moves purely under the influence of gravity and its own inertia. Interestingly, here we find that, under some conditions, the tying to the Earth may not be needed at all to achieve the stable double rotating motion of ERSE. In fact, the dynamic equilibrium achieved by the magical mass distribution $\mu(s)$ derived in Ch. 2 does *not* assume that the loopy ERSE is tied. Thus, it is in principle possible that an untied ERSE exhibits persistent shape and everlasting double rotating motion. *Moreover, such an untied RSE may maintain its position in the geosynchronous frame rotating with the Earth much like a tied RSE*. To explore this fascinating possibility, here we study the dynamics of the untied elliptical RSE. We will show that its actual behavior crucially depends on the distance D between the geostationary level and the RSE top, called as "gap" in Fig. 1(a). In the following section, we find that there are two important characteristic values of the gap, $D_{hopping}$ and $D_{unbinding}$. If the gap $D < D_{hopping}$, untied ERSE exhibits nearly the same dynamics as a tied ERSE. That is, its bottom and top points execute only minute motions about their initial positions. Thus, strikingly, untied ERSE bottom remains close to the Earth as if the RSE would be tied to the Earth. On the other side, if the gap $D > D_{hopping}$, the untied ERSE as a whole hops up and then it falls back to the Earth. The maximum height reached by the RSE during this hopping increases with increasing D and it diverges as the gap D approaches the $D_{unbinding}$. In this limit, as well as for any gap $D > D_{unbinding}$, the ERSE unbinds from the Earth to infinity, much like an object with a speed above the second cosmic speed. In the following sections we present and discuss these findings in detail.

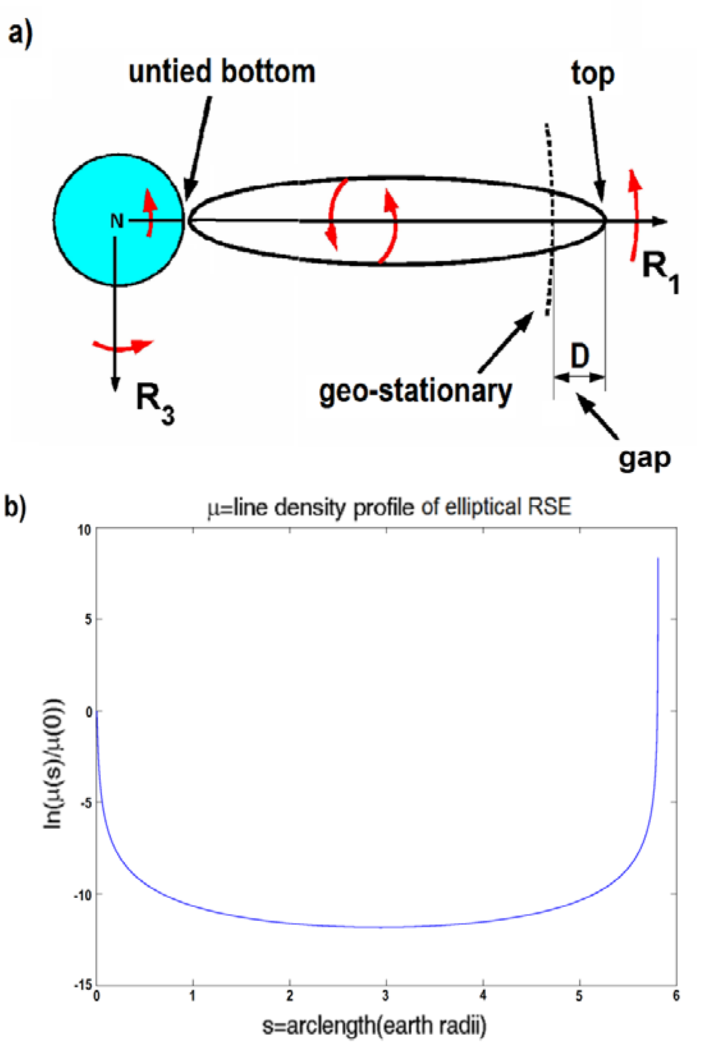

Fig. 1: (a) Elliptical version of RSE. The coordinate system (R_1, R_2, R_3) rotates together with the Earth around the R_2-axis (not shown) pointing through the north pole N. Indicated are the internal (nearly around the R_1-axis) and geo-synchronous (together with the Earth) rotations of the RSE. The RSE bottom is close to the Earth surface but it is *not* tied to it. The RSE top is at the distance *D* ("gap") above the geostationary satellite orbit (with the radius of 6.6108 Earth radii). In (b), the magical mass line density $\mu(s)$ versus the arc-length distance s from the RSE bottom [obtained by Eq. (8) of Ch. 2] of the elliptic RSE with the shape as in (a) for the RSE period of $T_{RSE} = 7.04\,\text{min}$, minor elliptical semi-axis $b = 0.17$ Earth radii, and the gap $D = 0.1564$ Earth radii. Note that the most of the RSE mass is largely concentrated in the top and bottom regions of the RSE.

3.2 Simulations of untied RSE: Quasi-tied motion, Hopping Transition and Unbinding Transition

In this section we outline the results of our simulations of the untied elliptic RSE as in Fig 1(a). We simulated these RSEs for three different values of the RSE minor semi-axis, $b = 0.16,\ 0.17,\ 0.18$ Earth radii, for two different values of period of the of the RSE internal rotation (around the R_1 axis in Fig. 1(a)) $T_{RSE} = 7.04\,\text{min}$ and $T_{RSE} = 3.52\,\text{min}$. From the simulations, we find that the dominant role is played by the RSE gap D, i.e., the distance between the RSE top and the geostationary level in Fig. 1(a) which is varied (for a fixed b and T_{RSE}) in the systems simulated in this study. In the simulations, at $t = 0$ the RSE loop is initially in the (R_1, R_3) plane (equatorial plane) of the *geosynchronous* frame in Fig. 1(a). To initiate the double rotation motion, the RSE is given initial spin around the R_1-axis, with the angular velocity $\Omega_{RSE} = 2\pi / T_{RSE}$. Unlike the study presented in Ch. 2, the RSE bottom point is *not* tied to the Earth. Thus, *the RSE moves purely under the influence of inertia and the Earth gravity.* Other details of our simulations are the same as in Ch. 2. The essential ingredient is the magical mass distributions, i.e., string mass line density which ensures that the double-rotating string configuration in Fig. 1(a) is an approximate dynamical equilibrium. As discussed in Ch. 2, this distribution can be obtained for strings of various shapes by applying Eq. (8) to the (initial) RSE shapes. In Fig. 1(b), we display thus obtained magical mass distribution for the elliptic RSE with $T_{RSE} = 7.04\,\text{min}$, $b = 0.17$, and $D = 0.1564$. Note that most of the RSE mass is concentrated in the top and bottom regions. Like in Ch. 2, floppy nearly inextensible RSE string is modeled by a finite element (polymer like) model of point masses ("beads") linked by stiff Hookean springs, see appendix C of Ch. 2. As in Ch. 2, the simulations are performed in the geosynchronous frame rotating with the angular velocity of the earth $\Omega_{earth} = 2\pi / T_{day}$ with $T_{day} = 1\ \mathit{sidereal\ day}$, as conceptualized in Fig. 1(a).

In Fig. 2, we introduce several significant geometrical parameters used to characterize the untied RSE position and orientation, in terms of the RSE projections onto the equatorial plane (R_1, R_3) of the geosynchronous frame. These are the azimuthal angle of the RSE's center of mass (CM), θ_{cm}, and the angle θ which is defined as the angle between bottom-to-top direction [projected onto the equatorial plane] and the Earth center-to-CM direction [projected onto the equatorial plane].

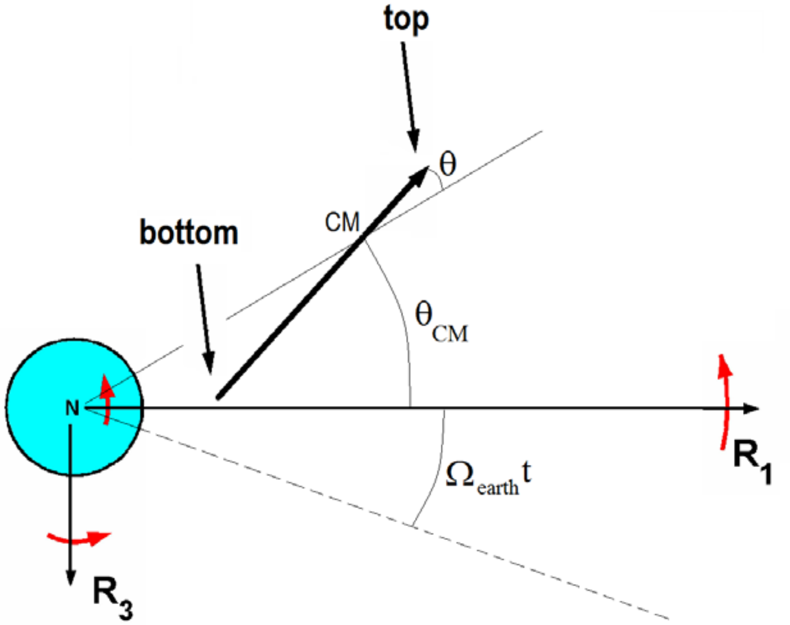

Fig. 2: Untied RSE projection onto the equatorial plane (R_1, R_3) of the geosynchronous frame which rotates with the angular velocity Ω_{earth} with respect to the inertial frame (dashed axis). The RSE is conceptualized as an arrow with head being the RSE top and end of tail being the RSE bottom.

These two angles are of paramount importance here. Note that, by Fig. 2, small values of θ and θ_{cm} correspond to the situations with the untied RSE "standing up" at a nearly fixed position on the Earth, as if it would be tied to the Earth (like it was in Ch. 2). Such a *quasi-tied* RSE should also exhibit only small variations of the length scales such as the distance from the center of the Earth to the CM, called as r_{cm} in the following.

From our simulations at $T_{RSE} = 3.52\,\text{min}$ we find that the RSE does indeed exhibit such a quasi-tied motion *proviso* the top-to-geostationary initial distance, i.e, the gap D [recall of Fig. 1(a)] is smaller than a critical value $D_{hopping} \cong 0.2$ Earth radii. In the *same* D-range, the quasi-tied behavior was also found in the simulation with the *larger* $T_{RSE} = 7.04\,\text{min}$. In this case however we find a small D-subdomain in which the RSE undergoes a narrowing instability similar to that discussed in Ch. 2. For example, for $b = 0.16$ Earth radii, this subdomain is between $D \approx 0.10$ and $D \approx 0.14$ Earth radii.

Striking quasi-tied behavior of the untied RSE, seen for $D < D_{hopping}$, is documented in the figures here. Thus, in Fig. 3(a) we see that the CM distance $r_{cm}(t)$ exhibits only very small oscillations so the height of RSE above the Earth surface does not change significantly. Furthermore, in Fig. 4(a), we see that the angle $\theta(t)$ [recall of Fig. 2] also exhibits only very small oscillations; hence the untied RSE "stands up". However, in Figs. 3(b,c), we see another interesting feature exhibited by the angle $\theta_{cm}(t)$ [recall of Fig. 2] and its derivative $\dot{\theta}_{cm}(t)$ which manifest not only small oscillations but also a systematic drift of the untied RSE around the Earth. Note that the $\dot{\theta}_{cm}(t)$ in Fig. 3(c) oscillates around a nonzero average value $\approx -3\times10^{-8} rad/\text{min}$, for D=0.1564 Earth radii, $b = 0.16$ Earth radii, $T_{RSE} = 7.04\,\text{min}$. Thus, the untied RSE bottom doesn't remain at rest over a fixed location on the rotating Earth. Rather, it slowly hovers around the Earth. By the figure 3 data (with D=0.1564 Earth radii), it would take about 394 years for this untied RSE to drift once around the Earth. That is, the RSE bottom would drift along the equator by about 100 km per year, i.e., about 19 cm/min. This is fairly slow.

Let us now discuss the small oscillations and stability of this "quasi-tied" yet free RSE. From the simulations we see that the system exhibits two notable oscillation modes: i) a "slow mode", with a period longer than 1 day, primarily seen in the dynamics of the center of mass coordinates $r_{cm}(t)$ and $\theta_{cm}(t)$ displayed in Fig. 3 (see also Fig. 5), and ii) a "fast" mode with a period of about 79 min, which is seen in Fig. 4(a) as a pendular motion of the angle $\theta(t)$ [recall of Fig. 2]. The time period, i.e., frequency of the fast mode was found not to depend significantly on the value of the gap D. On the other side, the slow mode exhibits a pronounced softening as the gap D approaches a critical value $D_{hopping} \cong 0.200$. This is documented in Fig. 5

which shows that the square of the slow mode frequency vanishes as the gap D approaches the critical value $D_{hopping} \cong 0.2$ Earth radii. In this figure we display both our simulations results and our analytic results (discussed in the Appendix to this chapter) for the soft mode frequency. Both of them indicate the complete softening of the slow mode at $D_{hopping} \cong 0.2$. Since the square of the slow mode frequency becomes negative for $D > D_{hopping}$ one should expect the quasi-tied RSE state becoming unstable for $D > D_{hopping}$. This is indeed confirmed by the simulations discussed in the following.

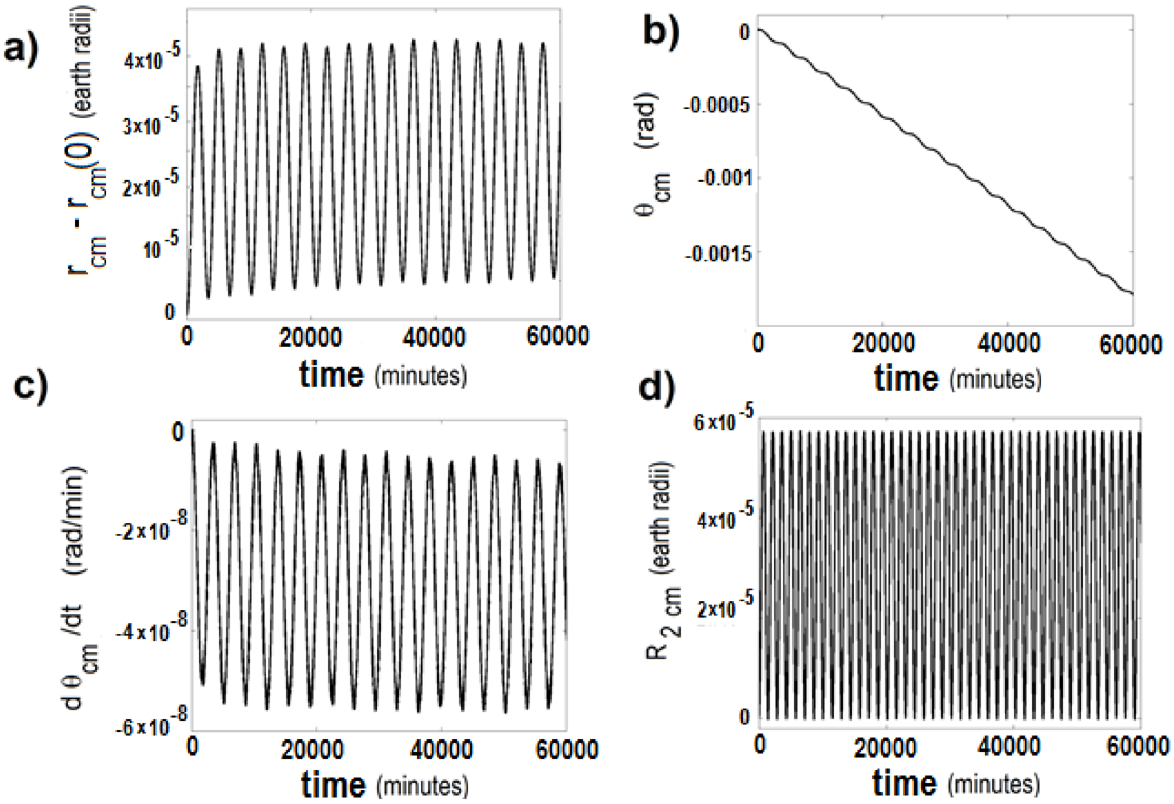

Fig. 3: The dynamics of the RSE center of mass in terms of its center of mass coordinates $r_{cm}(t) - r_{cm}(0)$ in (a) and $\theta_{cm}(t)$ in (b), for the gap *D*=0.1564 Earth radii, $b = 0.16$ Earth radii, $T_{RSE} = 7.04\,\text{min}$. Both quantities exhibit small slow mode oscillations with a period longer than one day [see also fig. 5]. The $\theta_{cm}(t)$ however also exhibits a slow steady drift. In (c) we plot $\dot{\theta}_{cm}(t)$ which oscillates around a nonzero average value corresponding to the RSE angular velocity (seen in the geosynchronous frame) of the RSE drift along the equator. In (d) we display the slow mode, with 1 sidereal day (exact) period, which is visible in the dynamics of the out-of-plane $(R_2)_{cm}$ coordinate of the RSE center of mass. Note that the out-of-plane RSE coordinates $(R_2)_{cm}$ oscillates around a nonzero time average reflecting the presence of a small tilt of the RSE out of the equatorial plane.

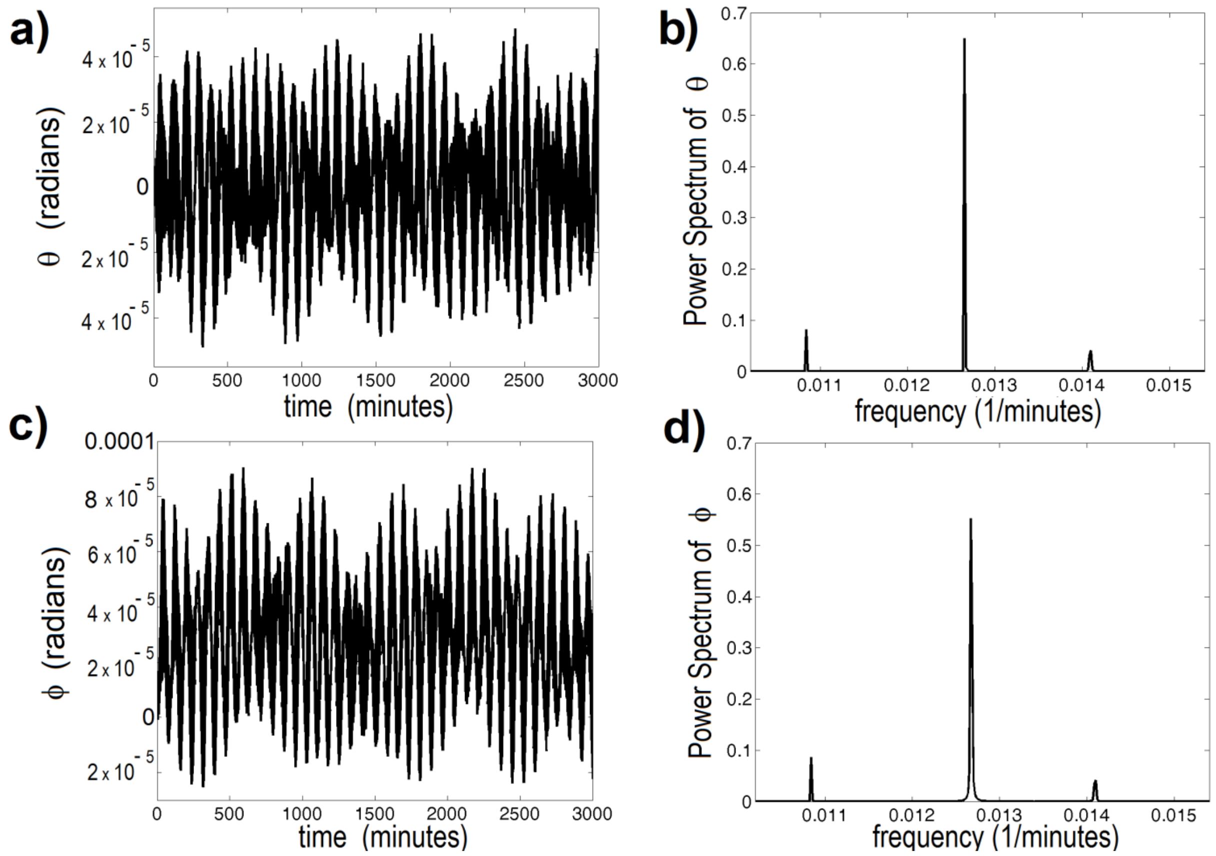

Fig. 4: In (a) and (c), the dynamics of the angles $\theta(t)$ and $\phi(t)$, for D=0.1564, $b = 0.16$ Earth radii, $T_{RSE} = 7.04\,\mathrm{min}$. They oscillate with nearly the same period of about 79.4 min, as evidenced by their power spectra in (b) and (d) that both exhibit strong peaks at the same frequency $f \approx 1/79.4\,\mathrm{min}$. Note however the existence of two nearby peaks due to which $\phi(t)$ and $\theta(t)$ exhibit beat like pattern with a repetition time of about 600 min. There are also much faster oscillations (with period of about 3.5min=T_{RSE}/2) due to which the curves in (a) and (c) appear thick. Finally, note that the out-of-plane angle $\phi(t)$ oscillates around a nonzero time average reflecting the presence of a small tilt of the RSE out of the equatorial plane.

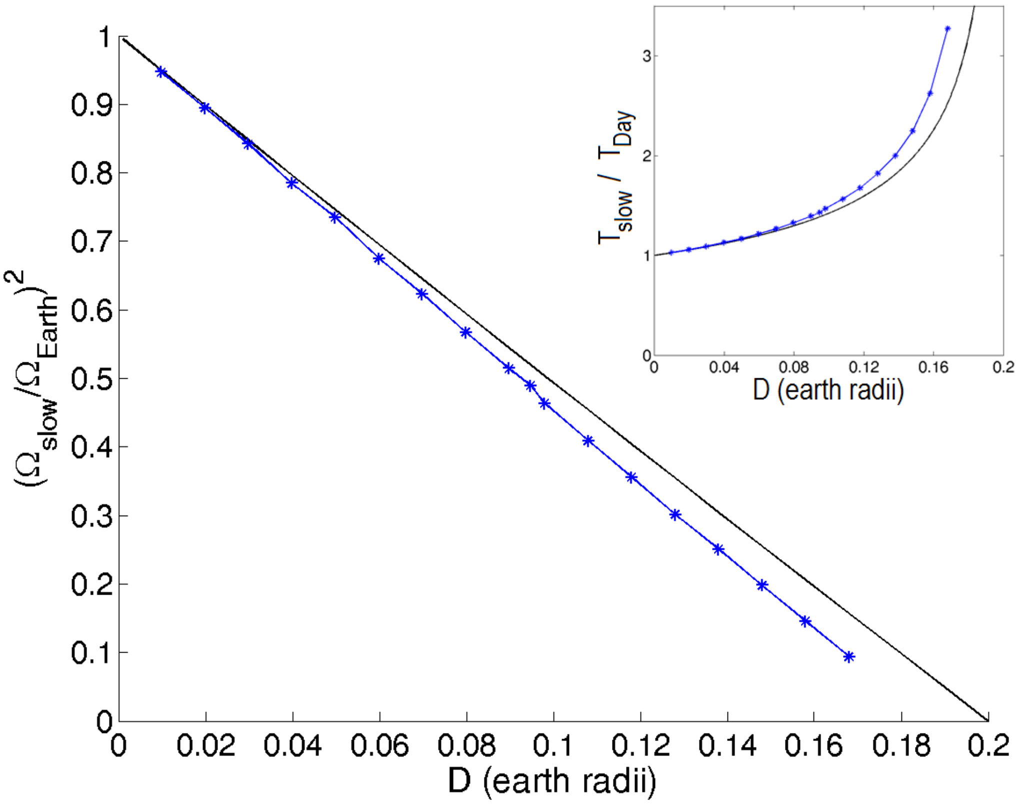

Fig. 5: Squared frequency of the slow mode seen in the dynamics of the RSE center of mass coordinates r_{cm} and θ_{cm} (the inset gives the mode time period in sidereal days). Here, $b = 0.16$ Earth radii, and $T_{RSE} = 3.52\,\text{min}$. Simulation results are indicated by the stars (connected by the blue line). We also display the corresponding analytic result (black line); see the appendix to this chapter, Eqs. (A22) and (A34), and the slow mode discussions after Eq. (A38). Both the simulations and the analytic result indicate vanishing of the soft mode frequency as the gap *D* approaches the critical value $D_{hopping} \cong 0.2$ Earth radii.

Above discussed fast and slow modes cause the RSE bottom and top small oscillations which go on within the equatorial plane, i.e., the (R_1, R_3) plane in Figs. 1(a) and 2. In addition, there are two other notable modes going out of this plane: i) a slow mode, with 1 sidereal day (exact) period (see the appendix), which is visible in the dynamics of the out-of-plane $(R_2)_{cm}$ coordinate of the RSE center of mass [see Fig. 3(d)], and ii) a fast mode visible in the dynamics of the out-of-plane tilt angle ϕ, i.e., the angle between the equatorial plane and the bottom-to-top direction [see Fig. 4(c)]. The angle ϕ (out-of-plane) oscillations have nearly the same time period $(\approx 79\,\text{min})$ and magnitude as the angle θ (in-plane) oscillations, see Fig. 4. The $\phi(t)$ and

$\theta(t)$ oscillations are however phase shifted with respect to each other by about 90^0. Due to this, over each 79 min the RSE bottom executes a small circle-like orbit a few kilometers in radius. We also note that out-of-plane RSE coordinates $(R_2)_{\text{cm}}$ and ϕ both exhibit nonzero time averages; see Figs. 3(d) and 4(c). So the RSE tilts out of equatorial plane. Such a small tilt was also seen in the tied RSE in Ch. 2 where we described its physical origin [see Fig. 7 of Ch. 2 and related discussions in Ch. 2].

In the appendix to this chapter, we will revisit the oscillations modes of the quasi-tied RSE by a simple analytic treatment which well captures many of the above results obtained in our simulations. This analytic calculation reproduces well the observed periods of the above described in-plane and out-of-plane slow and fast modes as well as the stability range of the quasi-tied RSE, $D < D_{hopping} \cong 0.2$ Earth radii. In this range, the oscillations of the angles ϕ and θ are small, i.e., the untied RSE "stands up" and its bottom remains close to the Earth surface. Motion of sliding climbers along such an untied RSE should not be very different from the motion of sliding climbers on the tied RSE studied in Ch. 2. This expectation is confirmed in by our simulations in Fig. 6 in which we display the motion of a sliding climber on the quasi-tied untied RSE with D=0.1564 Earth radii, $b = 0.16$ Earth radii, $T_{RSE} = 7.04\,\text{min}$. This motion is nearly the same as the motion of sliding climbers seen on the tied RSE [see Fig. 2 of Ch. 2].

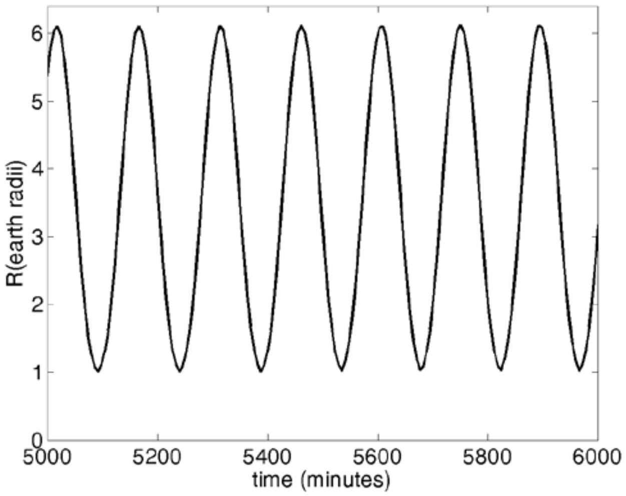

Fig. 6: The dynamics of the radial distance (from the Earth center) of a sliding climber on the quasi-tied untied RSE with D=0.1564 Earth radii, $b = 0.16$ Earth radii, $T_{RSE} = 7.04\,\text{min}$.

We now turn to discuss the untied RSE dynamics for the gap $D > D_{hopping} \cong 0.2$ Earth radii whence the quasi-tied state is unstable. From the simulations we find that the RSE exhibits highly anharmonic dynamics during which it significantly rises above the Earth. This is manifested by the dynamics of the center of mass coordinates $r_{cm}(t)$ and $\theta_{cm}(t)$ displayed in Fig. 7. See also the panels of Fig. 8, each corresponding to a different value of the gap *D*. Each panel of Fig. 8 gives a time sequence of RSE bottom and top projections onto the equatorial plane in the *inertial frame*, over the first 6000 min of time evolution. The RSE is conceptualized as an arrow with head being the RSE top and end of tail being the RSE bottom. There we see that for $D < D_{hopping} \cong 0.2$ Earth radii, the untied RSE is quasi-tied and nearly follows the Earth rotation. However, for $D > D_{hopping} \cong 0.2$, in Fig. 8 one can see that the untied RSE bottom *hops* away from the Earth surface. Details of this hopping are displayed in Fig. 7 in terms the center of mass coordinates $r_{cm}(t)$ and $\theta_{cm}(t)$. The hops appear like a train of "pulses" in $r_{cm}(t)$ separated by time intervals during which the RSE remains nearly at rest with respect to the rotating Earth. During a hop, the RSE top and bottom both raise up and then return back to their initial values while, concurrently, the angle $\theta_{cm}(t)$ undergoes a step-like change, see Fig. 7. Between two hops, the RSE bottom rests on the Earth (see Fig. 8) while the θ_{cm} is nearly constant (see Fig. 7), so the RSE is nearly at rest in the geosynchronous frame of the rotating Earth (recall of Fig. 2). The RSE position in this frame changes significantly only during the hops during which the RSE bottom displaces from one to another location on the Earth. For example, for the RSE with the gap $D = 0.3164$ Earth radii, by Fig. 7(b), the RSE bottom's geographical latitude changes by about 1.3 radians during a hop. From our simulations, for $D < 0.8$ Earth radii we find that this periodic like sequence of hops gets eventually interrupted after several hops (e.g., four hops for $D = 0.3164$, see Fig. 7). The interruption is marked by an event in which the RSE bottom significantly drops below the Earth surface after which the RSE transits into a more complex dynamical state. We will not discuss details about this state because in our model we did not attempt to include any interactions between the RSE and the Earth other than the attractive gravitational interaction. We also note that for $D > 1.3$ Earth radii, the RSE bottom typically misses to "dock" back onto the Earth surface after a hop. This happens because of a significant change of the RSE orientation encountered during long hops.

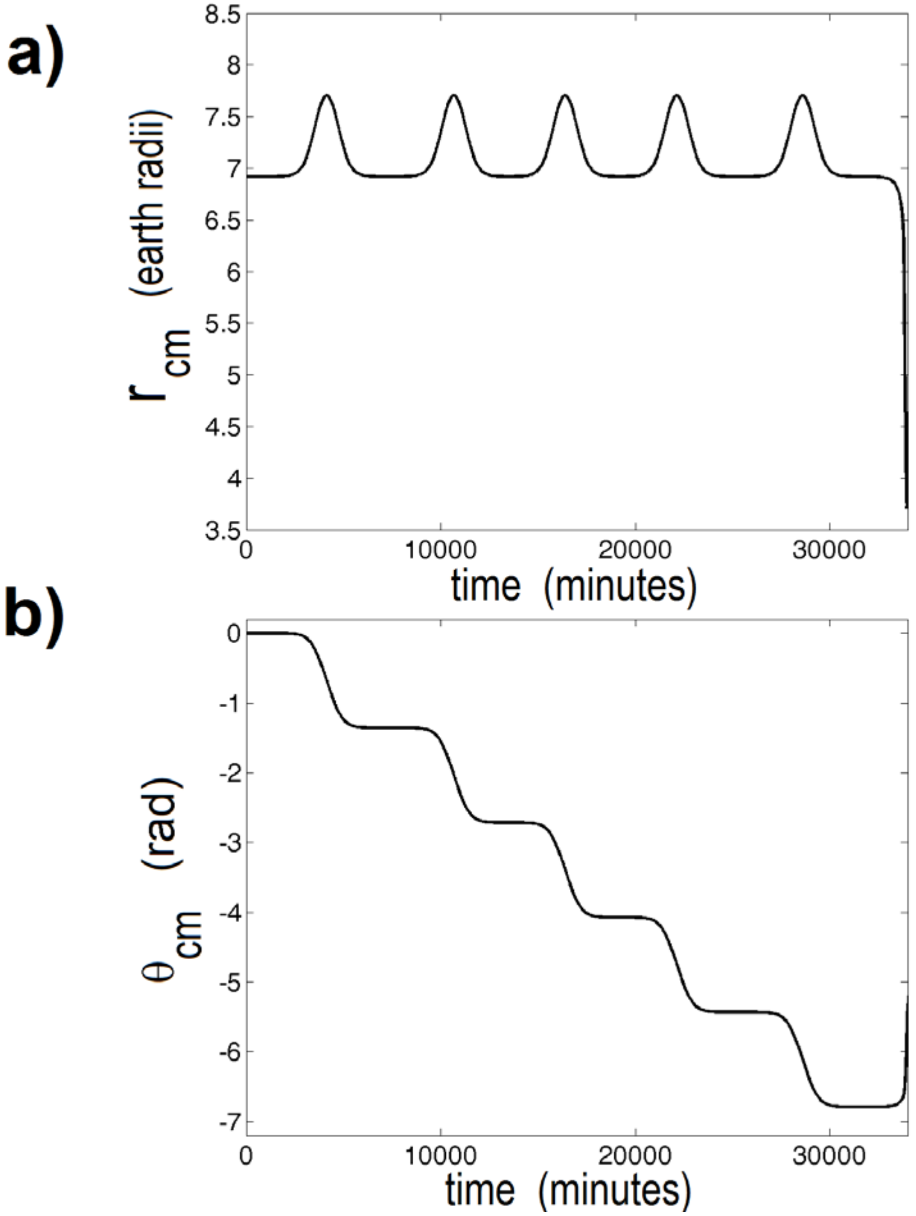

Fig. 7: The dynamics of the RSE center of mass in terms of its center of mass coordinates $r_{cm}(t)$ in (a) and $\theta_{cm}(t)$ in (b), for the hopping RSE with gap $D = 0.3164$ Earth radii, $b = 0.17$ Earth radii, $T_{RSE} = 7.04\min$.

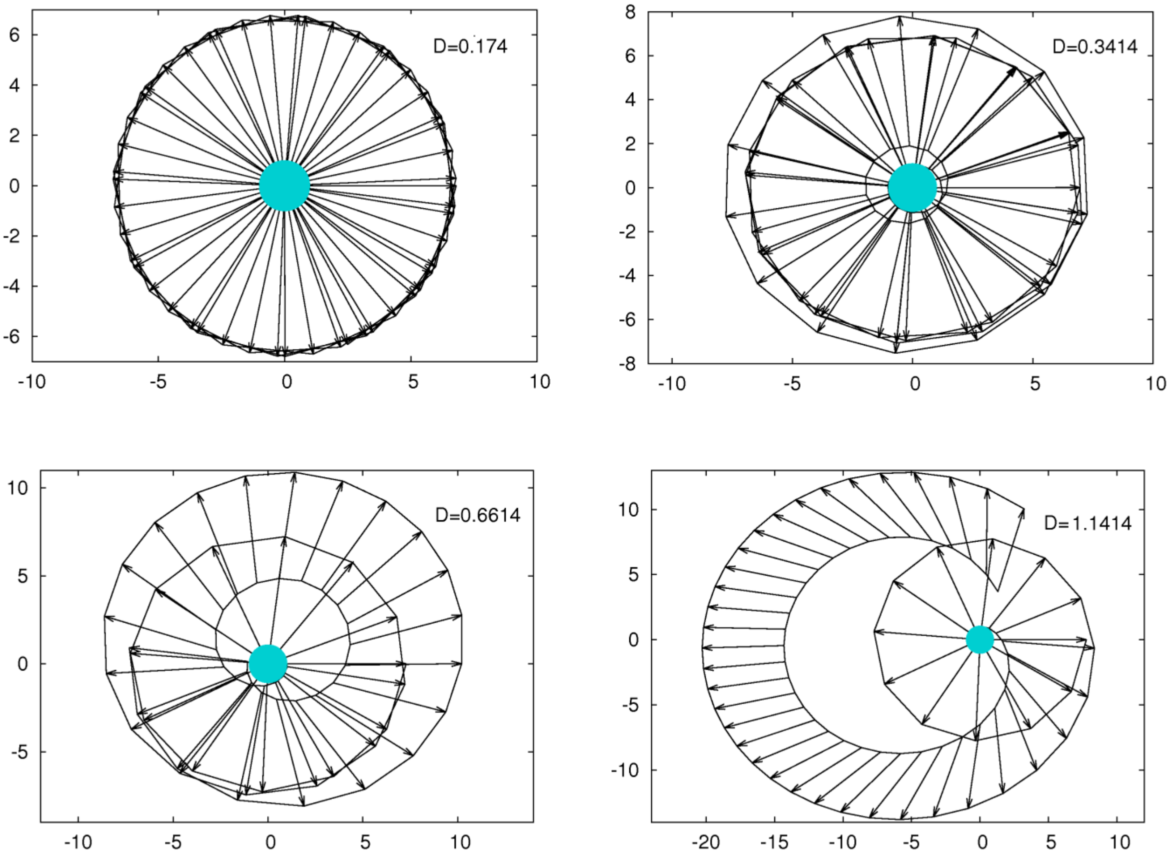

Fig. 8 (Part I): Each panel gives a time sequence of RSE bottom and top projections onto the equatorial plane in the *inertial frame*, over the first 6000 min of time evolution. Length unit used here is 1 Earth radius. In all panels $b = 0.17$ Earth radii, $T_{RSE} = 7.04\,\mathrm{min}$. The Earth is depicted as a small circle. The RSE is conceptualized as an arrow with head being the RSE top and end of tail being the RSE bottom. Displayed is one panel with $D < D_{hopping} \cong 0.2$ Earth radii, when the untied RSE is quasi-tied and nearly follows the Earth rotation. The remaining three panels are for the gaps D in the range between $D_{hopping} \cong 0.2$ Earth radii and $D_{unbinding} \cong 2.11$ Earth radii when the untied RSE exhibits a hopping motion. In the last example the hopping period is longer than the displayed 6000min evolution.

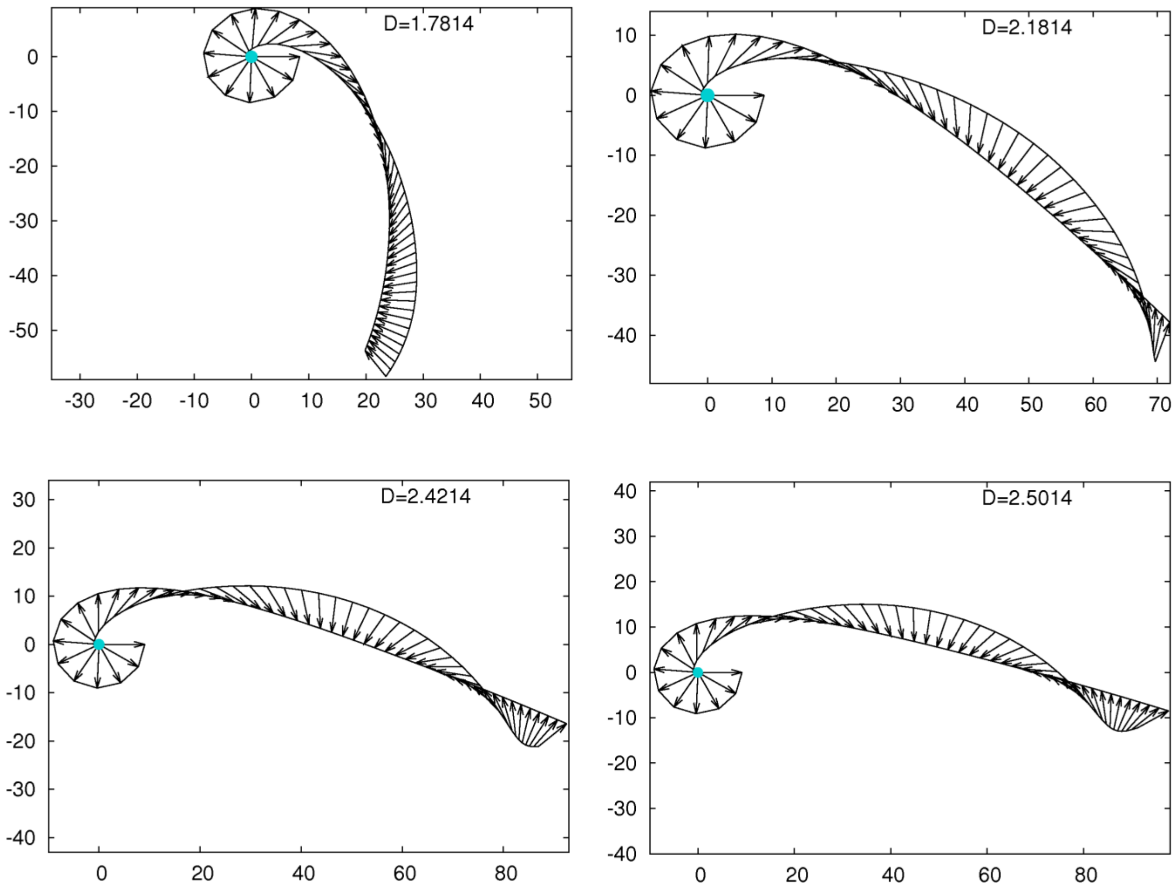

Fig. 8 (Part II): Each panel gives a time sequence of RSE bottom and top projections onto the equatorial plane in the *inertial frame*, over the first 6000 min of time evolution. Length unit used here is 1 Earth radius. In all panels $b = 0.17$ Earth radii, $T_{RSE} = 7.04\,\mathrm{min}$. The Earth is depicted as a small circle. The RSE is conceptualized as an arrow with head being the RSE top and end of tail being the RSE bottom. Displayed is one panel with the gap *D* in the range between $D_{hopping} \cong 0.2$ Earth radii and $D_{unbinding} \cong 2.11$ Earth radii when the untied RSE exhibits a hopping motion. In this example however the hopping period is significantly longer than the displayed 6000min evolution. The remaining three panels are for the gaps *D* in the range between $D > D_{unbinding} \cong 2.11$ Earth radii when the untied RSE escapes from the Earth to infinity.

From Fig. 8, it is manifest that the maximum height reached by the RSE during a hop significantly increases with increasing gap *D*. For example, for $D = 0.3164$ Earth radii [see Fig. 8

(part I)], the maximum radial distance of the RSE center of mass reached during the first hop $(r_{cm})_{\max} \approx 7.7$ Earth radii (see Fig. 7(a)), while for $D = 1.936$ Earth radii, we find that $(r_{cm})_{\max} \approx 153$ Earth radii. This dramatic increase of $(r_{cm})_{\max}$ signals another striking feature of the untied RSE: The $(r_{cm})_{\max}$ actually *diverges* at a critical value of the gap D we will label as $D_{unbinding}$. In the following, we will show that for any gap $D \geq D_{unbinding} \cong 2.11$ Earth radii, the ERSE unbinds from the Earth to infinity, much like an object with a speed above the second cosmic speed. On this route, in Fig. 9, we plot the ratio

$$Z(D) = \frac{r_{cm}(t=0)}{(r_{cm})_{\max}} \quad , \tag{1}$$

where $r_{cm}(t=0)$ is the initial value of the r_{cm} while the $(r_{cm})_{\max}$ is the first maximum value of r_{cm} reached for $t > 0$. Fig. 9 displays both our simulations results for the ratio *Z(D)* and our analytic result for this quantity discussed in the following sections. The figure 9 is to a large extent central to this Chapter as it elucidates all major interesting dynamical phenomena exhibited by untied RSE. Thus, for $D < D_{hopping} \cong 0.2$ Earth radii, we see that that $Z(D) \cong 1$. This is the signature of the quasi-tied motion of RSE (see Fig. 3(a)) which behaves as if is tied to the Earth. For $D > D_{hopping}$, the ratio *Z(D)* in Eq. (1) is visibly less than 1 which is the signature of the RSE exhibiting hopping motion (see Fig. 7(a)). With increasing gap *D,* the ratio *Z(D)* in Fig. 9 decreases and apparently goes to zero at a finite gap value $D_{unbinding} \cong 2.11$ Earth Radii at which $(r_{cm})_{\max}$ in Eq. (1) diverges and the RSE unbinds to infinity. Furthermore, we find from our simulations that for any gap $D \geq D_{unbinding} \cong 2.11$ Earth radii, the ERSE unbinds from the Earth to infinity, much like an object with a speed above the second cosmic speed. This is documented in Fig. 10 in which we plot the dynamics of the center of mass radial velocity, $\dot{r}_{cm} = dr_{cm}/dt$. By Fig. 10, for $D = D_{unbinding} \cong 2.11$, the radial velocity obeys the scaling law $\dot{r}_{cm}(t) \sim t^{-1/3}$ at long times. Thus, $r_{cm}(t) \sim t^{+2/3}$ at long times. This is the classical signature of an object being exactly at the unbinding threshold, like a spacecraft launched with the second cosmic speed that unbinds from the Earth with its radial distance increasing as $t^{2/3}$ at long times. In addition, from Fig. 10 we see that for $D > D_{unbinding} \cong 2.11$ Earth radii, the radial velocity $\dot{r}_{cm}(t)$ approaches a constant value (“escape velocity”) at long times. This is the classical signature of an object being above the unbinding threshold, like a spacecraft launched with a speed exceeding the second cosmic speed that unbinds from the Earth with its radial distance increasing linearly with time at long times. Beautiful views of the escaping RSE can be seen in the panels of Fig. 8 with $D > D_{unbinding} \cong 2.11$ Earth Radii.

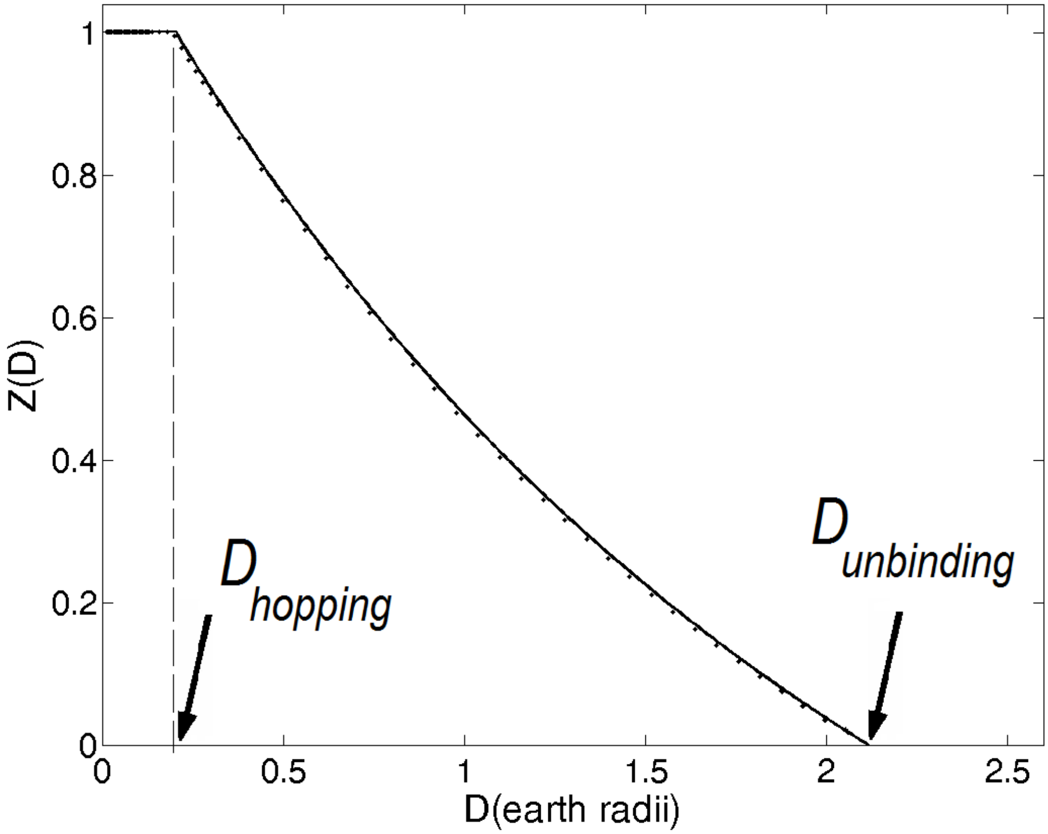

Fig. 9: The ratio *Z(D)* in Eq. (1): the results from our simulations (dots) versus analytic result (solid line) obtained by eq. (A29) of the appendix to this chapter. The simulations are done with $b = 0.17$ Earth radii, $T_{RSE} = 7.04\,\min$.

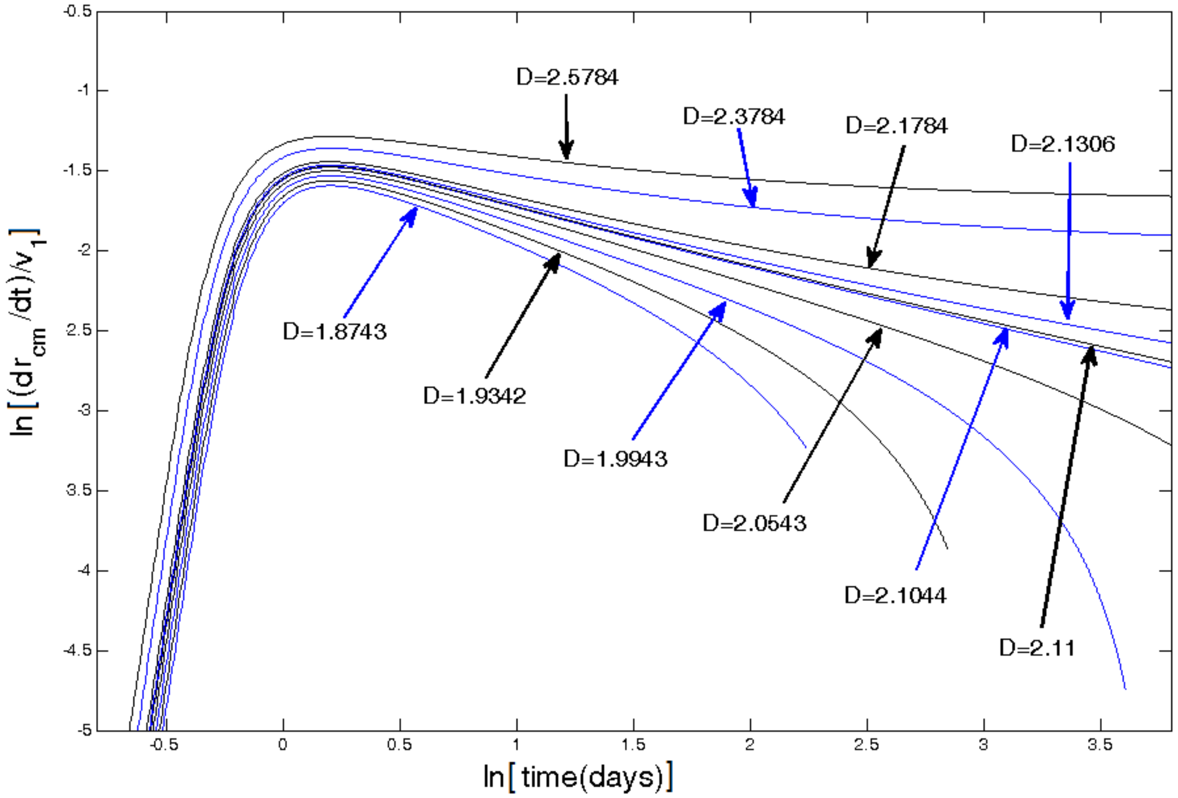

Fig. 10: Natural log of $\dot{r}_{cm}/v_1 = (dr_{cm}/dt)/v_1$ [with v_1, the first cosmic speed] versus the natural log of time (in days), for various values of the gap *D* around the unbinding threshold value $D_{unbinding} \cong 2.11$ Earth radii for which case the plot approaches the straight line with the slope -1/3, i.e. $\dot{r}_{cm} \sim t^{-1/3}$. Note that for $D > D_{unbinding} \cong 2.11$ Earth radii, the $\dot{r}_{cm}$ approaches at long times a constant value corresponding to escape velocity at infinity. The simulations are done with $b = 0.17$ Earth radii, $T_{RSE} = 7.04\,\mathrm{min}$.

In the appendix to this chapter, we will revisit the strongly nonlinear phenomena of the hopping and unbinding of the untied RSE, by a simple analytic treatment which well captures the results obtained in our simulations, such as the results in Fig. 9 and the value of $D_{unbinding}$.

3.3 Summary

If untied from the Earth, the RSE may still exhibit persistent shape and enduring double rotating motion while remaining close to the Earth. Under some conditions however we find that the untied RSE may undergo an instability leading it to a state in which it hops well above the Earth surface. With changing untied RSE parameters, the maximum hopping height may be made to diverge: The untied RSE unbinds from the Earth to infinity, i.e., to interplanetary space.

Appendix:

Simple analytically tractable model for the untied RSE dynamics

In this appendix we will analytically elucidate major results from our simulations. To this end, we recall that the RSE mass is largely concentrated in the two regions close to the RSE top and bottom, see Fig. 1(b). This motivates to model the RSE as a dumbbell comprised of two point masses, *M*, the mass of the RSE top and *m*, the mass of the RSE bottom. The length of the dumbbell *l*, corresponding to the top to bottom distance, will be assumed to be constant. The top-to-bottom distance indeed exhibits only very small changes (oscillations) in the quasi-tied regime, and relatively small changes in hopping/unbinding regimes (if the RSE is not too far from the Earth). Interestingly however, a simple dumb-bell model provides some *quantitatively* very accurate results not only for the RSE quasi-tied regime but also for the for the RSE unbinding regime, as we have already anticipated in fig. 9. Here we discuss in detail these analytic results.

The RSE quasi-tied state in fig. 1(a) corresponds to the dumbbell dynamical equilibrium state realized in the geo-synchronous frame, see fig. A1(a). For it, the total of centrifugal and gravitational forces (of the Earth) on the dumbbell vanishes,

$$0 = m\left(\Omega_E^2 R_E - \frac{GM_E}{R_E^2}\right) + M\left(\Omega_E^2 r_{M,eq} - \frac{GM_E}{r_{M,eq}^2}\right). \tag{A1}$$

Here, $M_E, R_E, \Omega_E = 2\pi / T_{day}$ (T_{day} =sidereal day) are respectively the mass, radius and the angular velocity of the Earth, while $r_{M,eq}$ is the equilibrium radial distance of the top with the mass *M*. The length of the dumb-bell is thus

$$l = r_{M,eq} - R_E\,. \tag{A2}$$

It should be noted (here and in the following) that eq. (A1) holds even if the bottom is above the surface of the earth, in which case R_E signifies the equilibrium radial distance of the bottom

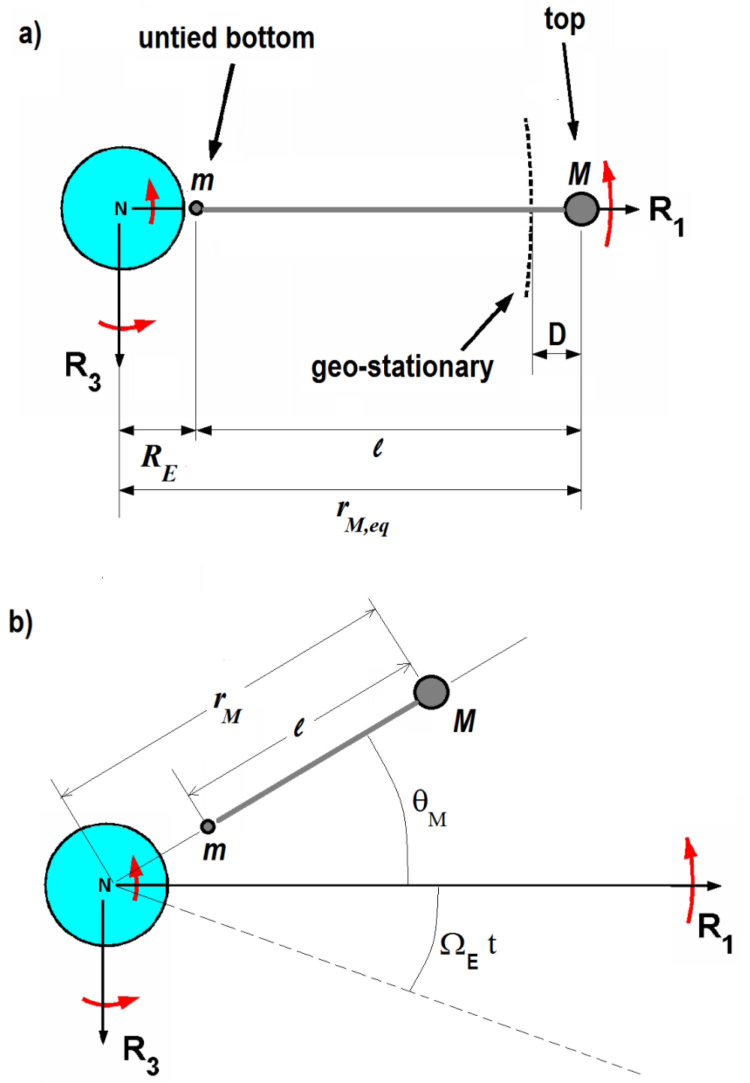

Fig. A1: (a) Dumbbell in the dynamical equilibrium state in geo-synchronous frame. The coordinate system (R_1, R_2, R_3) rotates together with the Earth around the R_2-axis (not shown) pointing through the north pole N. In (b), the degrees of freedom r_M and θ_M used in the Lagrangian in Eq. (A9). The dashed axis is static in the *inertial frame.*

with mass *m.* It is convenient to introduce the radius of the geo-synchronous satellite orbit, r_{geo}, satisfying the relation

$$GM_E = \Omega_E^2 r_{geo}^3 \ . \tag{A3}$$

By eqs. (A3) and (A1),

$$0 = m\left(R_E - \frac{r_{geo}^3}{R_E^2}\right) + M\left(r_{M,eq} - \frac{r_{geo}^3}{r_{M,eq}^2}\right). \tag{A4}$$

By eq. (A4), the dynamical equilibrium condition requires specially chosen value of the bottom to top mass ratio,

$$\frac{m}{M} = -\frac{r_{M,eq} - \dfrac{r_{geo}^3}{r_{M,eq}^2}}{R_E - \dfrac{r_{geo}^3}{R_E^2}} = \frac{r_{M,eq}R_E^2}{r_{geo}^3}\frac{1-\left(\dfrac{r_{geo}}{r_{M,eq}}\right)^3}{1-\left(\dfrac{R_E}{r_{geo}}\right)^3}. \tag{A5}$$

By Eq. (A5), positivity of the *m/M* ratio implies that $R_E < r_{geo} < r_{M,eq}$. In our case, r_{geo}=6.6108 Earth radii, so in the denominator of eq. (A5) one has the small quantity

$$\left(\frac{R_E}{r_{geo}}\right)^3 = 6.6108^{-3} = 3.46\times 10^{-3}, \tag{A6}$$

which is [in terms of Eq. (A1)] the ratio between the inertial (centrifugal) and gravitational force on the bottom with mass *m*. Ignoring this small quantity reduces eq. (A5) to,

$$\frac{m}{M} \cong \frac{r_{M,eq}R_E^2}{r_{geo}^3}\left[1-\left(\frac{r_{geo}}{r_{M,eq}}\right)^3\right] = \left(\frac{R_E}{r_{geo}}\right)^2\left(1+\frac{D}{r_{geo}}\right)\left[1-\left(1+\frac{D}{r_{geo}}\right)^{-3}\right] \tag{A7}$$

where we introduced the gap distance $D = r_{M,eq} - r_{geo}$; see fig. A1(a). For $D << r_{geo}$, by expanding terms in Eq. (A7),

$$\frac{m}{M} \cong 3\left(\frac{R_E}{r_{geo}}\right)^2\frac{D}{r_{geo}} = 3\left(\frac{R_E}{r_{geo}}\right)^3\frac{D}{R_E}. \tag{A8}$$

By recalling here that, for example, $D_{hopping}/R_E \cong 0.2$, in view of Eq. (A6), the bottom to top mass ratio is typically very small quantity in the presently studied systems.

The equations of motion of the dumbbell can be generated in a standard way, by using classical Lagrangian $L = KE - PE$, with kinetic and gravitational potential energy expressed in terms of suitable coordinates, such as the angles $\theta(t)$ and $\theta_{cm}(t)$ (defined in fig. 2), the center of mass distance, and the out of plane coordinates $\phi(t)$ and $(R_2)_{\mathrm{cm}}$ already introduced in sec. 2. We will outline some results of this general and rather complex approach after discussing a simple approach which however correctly illuminates all major aspects of the RSE dynamics, such as the RSE slow mode discussed in sec. 2, as well as the hopping and unbinding transitions. The approach is based on the same approximation as done in the transition from eq. (A5) to eq. (A7), which is to ignore inertial relative to gravitational effects of the bottom mass *m*. See Eq. (A6) and the above discussions. This is tantamount to ignoring the kinetic energy of the bottom mass while maintaining its gravitational potential energy in the Lagrangian. In addition, we will set the angle $\theta(t)$ in fig. 2 to be zero [as if the bottom is suspended from a *slowly* moving top], see fig. A1(b). This constraint is motivated by our simulations which indeed show that $\theta(t)$ is very small in quasi-tied states. Moreover, this angle remains small in the hopping state, at least while the RSE is relatively close to the Earth; see Fig. 8. With the above two assumptions, the resulting Lagrangian $L = KE - PE$ has the form

$$L(r_M, \dot{r}_M, \dot{\theta}_M) = \frac{M}{2}[(\dot{r}_M)^2 + r_M^2(\Omega_E + \dot{\theta}_M)^2] + \frac{GM_E M}{r_M} + \frac{GM_E m}{r_M - l}. \qquad \text{(A9)}$$

Here, as in fig. A1(b), the r_M is the radial distance of the top and θ_M is the azimuthal angle of the top in the *geo-synchronous* frame. The first two terms in the eq. (A1) are just the standard Lagrangian for the motion of the object of mass *M* (the top) in the Earth gravitational field, while the last term emerges from the gravitational potential energy of the bottom with the mass *m* which is at the radial distance = $r_M - l$ from the Earth center; see fig. A1(b). By eq. (A9), the main effect of the bottom presence is to modify the form of the central potential seen by the top with the mass *M*. The resulting Lagrangian dynamics is thus of a standard form, with a conserved angular momentum,

$$\frac{\partial L}{\partial \dot{\theta}_M} = Mr_M^2(t)[\Omega_E(t) + \dot{\theta}_M(t)] = Mr_M^2(0)[\Omega_E(0) + \dot{\theta}_M(0)], \qquad \text{(A10)}$$

and a conserved energy function,

$$\begin{aligned} E = KE + PE &= \frac{M}{2}[(\dot{r}_M)^2 + r_M^2(\Omega_E + \dot{\theta}_M)^2] - \frac{GM_E M}{r_M} - \frac{GM_E m}{r_M - l} \\ &= \frac{M}{2}(\dot{r}_M)^2 + U_{eff}(r_M) = \frac{M}{2}(\dot{r}_M(0))^2 + U_{eff}(r_M(0)) \end{aligned} , \tag{A11}$$

with the effective potential,

$$U_{eff}(r_M) = -\frac{GM_E M}{r_M} - \frac{GM_E m}{r_M - l} + \frac{Mr_M^4(0)[\Omega_E + \dot{\theta}_M(0)]^2}{2r_M^2}, \tag{A12}$$

or, by Eq. (A3),

$$U_{eff}(r_M) = M\Omega_E^2\left[-\frac{r_{geo}^3}{r_M} - \frac{r_{geo}^3}{r_M - l}\frac{m}{M} + \frac{r_M^4(0)[1 + \dot{\theta}_M(0)/\Omega_E]^2}{2r_M^2}\right] . \tag{A13}$$

By Eq. (A9), the Euler-Lagrange equation of motion for r_M has the form,

$$\begin{aligned} M\ddot{r}_M(t) &= -\frac{GM_E M}{r_M^2(t)} - \frac{GM_E m}{(r_M(t) - l)^2} + Mr_M(t)[\Omega_E(t) + \dot{\theta}_M(t)]^2 \\ &= -\left.\frac{\partial U_{eff}}{\partial r_M}\right|_{r_M = r_M(t)} = -\frac{GM_E M}{r_M^2(t)} - \frac{GM_E m}{(r_M(t) - l)^2} + \frac{Mr_M^4(0)[\Omega_E + \dot{\theta}_M(0)]^2}{r_M^3(t)} \end{aligned} \tag{A14}$$

Simplest solutions of eq. (A4) are dynamic equilibrium states which are circular orbits with constant $r_M(t) = r_M(0)$ and $\dot{\theta}_M(t) = \dot{\theta}_M(0)$. For them, by eq. (A14)

$$-\left.\frac{\partial U_{eff}}{\partial r_M}\right|_{r_M = r_M(0)} = -\frac{GM_E M}{r_M^2(0)} - \frac{GM_E m}{(r_M(0) - l)^2} + Mr_M(0)[\Omega_E(0) + \dot{\theta}_M(0)]^2 = 0, \tag{A15}$$

or, by eq. (A3),

$$-\frac{r_{geo}^3}{r_M^2(0)} - \frac{r_{geo}^3}{(r_M(0) - l)^2}\frac{m}{M} + r_M(0)[1 + \dot{\theta}_M(0)/\Omega_E]^2 = 0 \tag{A16}$$

A dumbbell in this dynamic equilibrium state will appear static in the geo-synchronous frame if $\dot{\theta}_M(0) = 0$. For this case, eq. (A16) yields the relation,

$$\frac{m}{M}=\frac{(r_M(0)-l)^2 r_M(0)}{r_{geo}^3}\left[1-\left(\frac{r_{geo}}{r_M(0)}\right)^3\right] \tag{A17}$$

which is identical to eq. (A7), by recalling eq. (A2), i.e.,

$$l=r_M(0)-R_E=r_{geo}+D-R_E\,. \tag{A18}$$

By eq. (A14), small harmonic oscillations, $\delta r_M(t)=r_M(t)-r_M(0)$ around this dynamic equilibrium state obey the linearized equation of motion

$$M\delta\ddot{r}_M(t)=-\left.\frac{\partial^2 U_{eff}}{\partial {r_M}^2}\right|_{r_M=r_M(0)}\delta r_M(t) \tag{A19}$$

By eq. (A19), angular frequency of these small oscillations obeys the relation

$$\Omega_{slow}^2=M^{-1}\left.\frac{\partial^2 U_{eff}}{\partial {r_M}^2}\right|_{r_M=r_M(0)}\,, \qquad \ldots \tag{A20}$$

which is by eq. (A13) [with $\dot{\theta}_M(0)=0$], and eqs. (A17) and (A18), found to be

$$\begin{aligned}\left(\frac{\Omega_{slow}}{\Omega_E}\right)^2 &=1-2\frac{r_M(0)-R_E}{R_E}\left[1-\left(\frac{r_{geo}}{r_M(0)}\right)^3\right]\\ &=1-2\frac{r_{geo}+D-R_E}{R_E}\left[1-\left(\frac{r_{geo}}{r_{geo}+D}\right)^3\right]\end{aligned}\,. \tag{A21}$$

These are the slow RSE oscillations discussed in the context of figs. 3 and 5 from our simulations of the floppy untied RSE. In fig. 5 we already presented theoretical result for Ω_{slow} of the dumb-bell model (see also the discussions after eq. (A38)). Notably from the figure, theoretical result closely follows the results from the simulations of the floppy untied RSE. By eq. (A21), $\Omega_{slow}\to\Omega_E$ for $D\to 0$. By eq. (A21) with $r_{geo}=6.6108R_E$, one finds that $\Omega_{slow}\to 0$ for $D\to D_{hopping}=0.20123R_E$ in accord with the observed softening of the slow mode from our RSE simulations seen in fig. 5. A notable feature of the theoretical result in fig. 5 is that ${\Omega_{slow}}^2$

appears as a nearly linear function of the gap *D*. In fact, our result in Eq. (A21) can be expanded in powers of the small parameter R_E / r_{geo} , with the result

$$\left(\frac{\Omega_{slow}}{\Omega_E}\right)^2 = 1 - 6\overline{D} + \frac{R_E}{r_{geo}}(6\overline{D} + 6\overline{D}^2) + \left(\frac{R_E}{r_{geo}}\right)^2 (-12\overline{D}^2 - 8\overline{D}^3) + O\left(\frac{R_E}{r_{geo}}\overline{D}\right)^3 \quad , \qquad \text{(A22)}$$

with

$$\overline{D} = \frac{D}{R_E} \quad . \qquad \text{(A23)}$$

Eq. (A22) can be iteratively solved to find the $\overline{D}_{hopping} = D_{hopping} / R_E$ for which $\Omega_{slow} \to 0$, with the result having the form of an expansion in powers of the small parameter R_E / r_{geo},

$$\overline{D}_{hopping} = \frac{D_{hopping}}{R_E} = \frac{1}{6} + \frac{7}{36}\frac{R_E}{r_{geo}} + \left(\frac{2}{3}\right)^4 \left(\frac{R_E}{r_{geo}}\right)^2 + O\left(\frac{R_E}{r_{geo}}\right)^3 \quad . \qquad \text{(A24)}$$

For $r_{geo} = 6.6108 R_E$, after truncating the $(R_E / r_{geo})^3$ term, eq. (A24) yields $\overline{D}_{hopping} = D_{hopping} / R_E = 0.20060$, versus the aforementioned result $\overline{D}_{hopping} = D_{hopping} / R_E = 0.20123$ obtained by numerically solving eq. (A21) with $\Omega_{slow} = 0$. It is interesting to note that, by Eq. (A24), in the limit of slowly rotating planets $R_E / r_{geo} \to 0$, the $\overline{D}_{hopping} = D_{hopping} / R_E$ has a finite universal value = 1/6. For $\overline{D} < \overline{D}_{hopping} < 1$, from the specific form of the expansion eq. (A22) [with higher order terms in $\overline{D}$ going with even higher order terms in R_E / r_{geo}] it is evident that the terms nonlinear in $\overline{D}$ give only a minor contribution for a small R_E / r_{geo}. Thus, to a good approximation for $\overline{D} < \overline{D}_{hopping}$,

$$\left(\frac{\Omega_{slow}}{\Omega_E}\right)^2 \approx 1 - 6\left(1 - \frac{R_E}{r_{geo}}\right)\overline{D} = 1 - \frac{\overline{D}}{\overline{D}_{hopping}} \quad , \qquad \text{(A25)}$$

i.e., the $\Omega_{slow}{}^2$ is nearly a linear function of the gap *D*, as evidenced from its plot in Fig. 5. By eq. (A25), $\overline{D}_{hopping} \approx 1/(6 - 6R_E / r_{geo})$, which for $r_{geo} = 6.6216 R_E$ yields a sound result

$\overline{D}_{hopping} \approx 0.19637$. This is however more off the exact result than the aforementioned result obtained by Eq. (A24). Later on in this section we will revisit the result for $\overline{D}_{hopping}$ within the exact dumbbell model going beyond the approximations involved in the theory based on the approximate Lagrangian eq. (A9). It turns out that the results in Eqs. (A22) and (A24) are actually *exact* to the second order in R_E / r_{geo}, as displayed in these two equations.

We now proceed to discuss the hopping and unbinding transitions within the approximate Lagrangian eq. (A9). By the energy conservation eq. (A11), in combination with the eq. (A13) [with $\dot{\theta}_M(0) = 0$], and eq. (A17), one finds, after a lengthy algebra,

$$\frac{1}{2}(\dot{r}_M)^2 - \frac{1}{2}(\dot{r}_M(0))^2 = -\frac{1}{M}[U_{eff}(r_M) - U_{eff}(r_M(0))], \tag{A26}$$

with,

$$\begin{aligned} &U_{eff}(r_M) - U_{eff}(r_M(0)) \\ &= M\Omega_E^2 \frac{r_M^2(0)l}{2} \cdot \frac{(r_M - r_M(0))^2}{r_M(r_M - l)} \cdot \left(\frac{Z}{r_M(0)} - \frac{1}{r_M} \right), \end{aligned} \tag{A27}$$

where

$$Z = \frac{r_M(0)}{l} - 2\left[1 - \left(\frac{r_{geo}}{r_M(0)}\right)^3\right], \tag{A28}$$

or, by Eq. (A18),

$$Z = Z(D) = \frac{r_{geo} + D}{r_{geo} + D - R_E} - 2\left[1 - \left(\frac{r_{geo}}{r_{geo} + D}\right)^3\right]. \tag{A29}$$

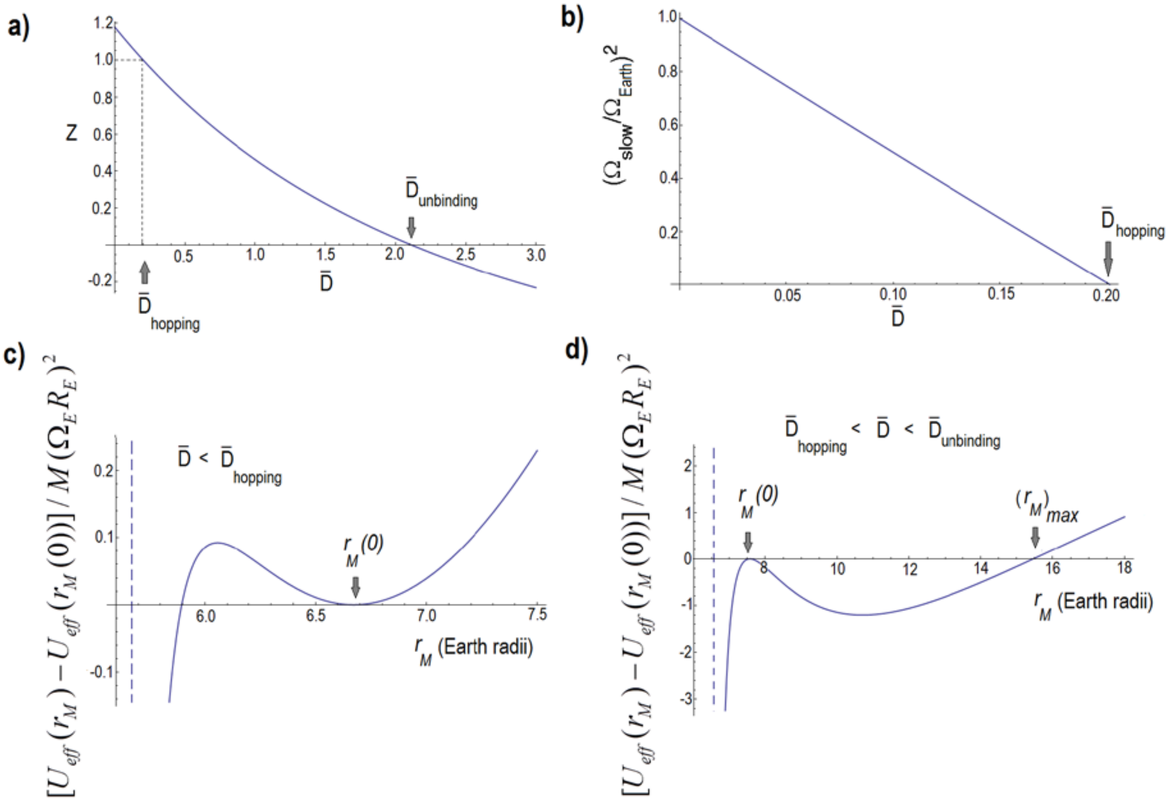

Fig. A2: (a) Function Z versus $\overline{D} = D / R_E$; see eq. (A29). (b) Slow mode angular frequency (squared) versus $\overline{D} = D / R_E$; see eqs. (A21) and (A30). (c) Case $\overline{D} < \overline{D}_{hopping}$: form of the effective potential eq. (A27) for $\overline{D} = 0.05$. (d) Case $\overline{D}_{hopping} < \overline{D} < \overline{D}_{unbinding}$: form of the effective potential eq. (A27) for $\overline{D} = 0.95$. In all panels, $r_{geo} = 6.6108 R_E$.

We plot the function $Z(D)$ in fig. A2(a), for the interesting case with $r_{geo} = 6.6108 R_E$. The implications of the results in eqs. (A26-A29) are best understood from the plots of the potential difference eq. (A27) displayed in the panels of fig. A2. Thus, in fig. A2(c) we see that for $D < D_{hopping}$ [whence $Z(D) > 1$] the potential $U_{eff}(r_M)$ has stable minimum at $r_M = r_M(0)$. This situation corresponds to the quasi-tied state with a stable slow mode which frequency is given by eq. (A21). This equation can be easily shown [by eq. (A29)] to be equivalent to

$$\left(\frac{\Omega_{slow}}{\Omega_E}\right)^2 = \frac{r_{geo} + D - R_E}{R_E} \cdot (Z(D) - 1) \tag{A30}$$

For $D \to D_{hopping}$, the $Z(D) \to 1$, so the slow mode completely softens in this limit; see figs. A2(a) and (b). By fig. A2(d), for $D > D_{hopping}$ [whence $Z(D) < 1$] the potential $U_{eff}(r_M)$ has unstable maximum at $r_M = r_M(0)$, corresponding, by Eq. (A30), to an unstable slow mode. This situation corresponds to the hopping RSE state seen in our simulations, with $r_M(t)$ rising above $r_M(0)$ all the way up to a turning point where momentarily $\dot{r}_M(t) = 0$. In our case $\dot{r}_M(0) \approx 0$, so by eqs. (A26) and (A27) [see also fig. A2(d)], at the turning point, the $r_M(t)$ reaches its maximum value given by

$$(r_M)_{\max} = \frac{r_M(0)}{Z(D)} = \frac{r_{geo} + D}{Z(D)}. \tag{A31}$$

Thus,

$$Z(D) = \frac{r_M(0)}{(r_M)_{\max}} \tag{A32}$$

From fig. A2 we see that $Z(D)$ crosses zero at a characteristic value of *D*. This corresponds to the unbinding transition point at which $(r_M)_{\max} \to \infty$ and the system approaches infinity. This transition happens at the characteristic *D* value solving the equation $Z(D_{unbinding}) = 0$. For example, for the interesting case with $r_{geo} = 6.6108 R_E$, one finds [numerically, by eq. (A29)] that $Z(D) \to 0$, i.e., $(r_M)_{\max} \to \infty$ for $D \to D_{unbinding} = 2.1123 R_E$. This value is in a very good agreement with our simulations of the floppy untied RSE which indicate that $D_{unbinding} \approx 2.11 R_E$; see fig. 9. In this figure, we employed the center of mass radial distance r_{cm} rather than the top radial distance r_M, yet the difference between the two is very small due to the small *m/M* ratio; see eq. (A8). Overall, from fig. 9, one can see that the ratio $r_{cm}(0)/(r_{cm})_{\max}$ from the simulations of RSE is strikingly well approximated by our function $Z(D)$ in eq. (A29).

For $D = D_{unbinding}$ [whence *Z=0*], the eqs. (A27) [with $\dot{r}_M(0) = 0$] and (A29) can be easily used to show that $\dot{r}_M(t) \sim t^{-1/3}$ at long times, in accord with our RSE simulations results displayed in fig. 10. For $D > D_{unbinding}$ [whence *Z(D) < 0*], the eqs. (A27) [with $\dot{r}_M(0) = 0$] and (A29) can be easily used to show that, at long times, $\dot{r}_M(t = \infty) \sim [-Z(D)]^{1/2} \sim \sqrt{D - D_{unbinding}}$ (for D slightly above $D_{unbinding}$). So the system reaches infinity with a finite escape velocity, in accord with our RSE simulations results displayed in fig. 10.

Finally, for completeness, we mention that the equation $Z(D_{unbinding}) = 0$ can be solved by an expansion in powers of the small parameter R_E / r_{geo}. We just quote the result truncated to the second order in R_E / r_{geo},

$$\frac{D_{unbinding}}{r_{geo}} = 2^{1/3} - 1 + \frac{1}{3}\frac{R_E}{r_{geo}} + \frac{2^{5/3}}{9}\left(\frac{R_E}{r_{geo}}\right)^2 + O\left(\frac{R_E}{r_{geo}}\right)^3 \quad . \tag{A33}$$

To this order, for $r_{geo} = 6.6108 R_E$, the truncated Eq. (A33) gives $D_{unbinding} \approx 2.1050 R_E$ in a reasonable agreement with the aforementioned exact numerical solution $D_{unbinding} = 2.1123 R_E$.

Thus far we confined our discussions within the framework of the simplified dumbbell Lagrangian eq. (A9). In the quasi-tied state, this model essentially freezes out the fast oscillations of the angles $\theta(t)$ and $\phi(t)$; see sec. 2 discussions and figs. 2 and 4. To discuss these fast modes, one must consider the exact equations of the dumbbell dynamics. They can be generated in a standard way, by using classical Lagrangian $L = KE - PE$, with kinetic and gravitational potential energy expressed in terms of suitable coordinates, such as the angles $\theta(t)$ and $\theta_{cm}(t)$ (defined in fig. 2), the center of mass distance, and the out of plane coordinates $\phi(t)$ and $(R_2)_{\mathrm{cm}}$ already introduced in sec. 2. The resulting equations of motion can be easily linearized around the dumbbell dynamical equilibrium state; recall of Eq. (A1). In this way, we found the frequencies of both slow and fast modes. There are two in-plane modes (proceeding within the Earth equatorial plane), and two out-of-plane modes (proceeding perpendicular to the equatorial plane); see fig. A3. Within the harmonic theory, two in-plane modes (slow and fast) are decoupled from the two out-of-plane modes (slow and fast). Frequencies of each pair of modes satisfy biquadratic equations that can be readily solved. Resulting expressions for the frequencies of these modes are rather cumbersome and a better physical insight is gained by representing them as expansions in powers of the small parameter R_E / r_{geo} (as we already did above with the frequency of the slow in-plane mode; recall of eq. A22). The solutions of the biquadratic equation for angular frequencies the in-plane modes are thus found in the form:

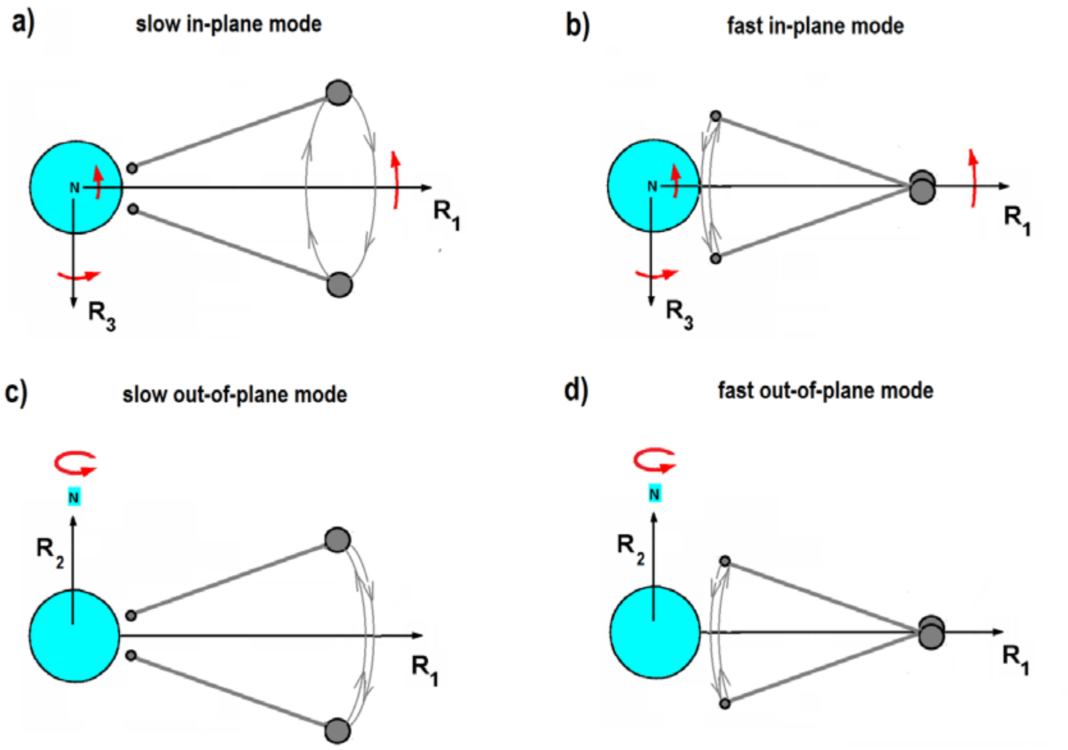

Fig. A3: Dumbbell modes: (a) Slow in-equatorial plane mode, best seen in the center of mass coordinates $\theta_{cm}(t) \approx \theta_M(t)$ and $r_{cm}(t) \approx r_M(t)$; see fig. 2. (b) Fast in-equatorial plane mode, best seen in the bottom dynamics or the angle $\theta(t)$; see fig. 2. (c) Slow out-of-equatorial plane mode, best seen in the center of mass R_2 coordinate. (d) Fast out-of-equatorial plane mode, best seen in the bottom R_2 coordinate or the angle $\phi(t)$.

$$\left(\frac{\Omega_{slow}^{in}}{\Omega_E}\right)^2$$

$$=1-6\overline{D}+\frac{R_E}{r_{geo}}(6\overline{D}+6\overline{D}^2)+\left(\frac{R_E}{r_{geo}}\right)^2(-12\overline{D}^2-8\overline{D}^3)+\left(\frac{R_E}{r_{geo}}\right)^3(-12\overline{D}+18\overline{D}^2+20\overline{D}^3+10\overline{D}^4)+\ldots \tag{A34}$$

for the slow in-plane mode (depicted in fig. A3(a)). For the fast in-plane mode (depicted in fig. A3(b)), we find

$$\left(\frac{\Omega_{fast}^{in}}{\Omega_m}\right)^2=1+\frac{R_E}{r_{geo}}+\left(\frac{R_E}{r_{geo}}\right)^2(1-\overline{D})+\left(\frac{R_E}{r_{geo}}\right)^3(-2\overline{D}+\overline{D}^2)+\ldots\ , \tag{A35}$$

with $\Omega_m=(GM_E/R_E^3)^{1/2}$, the angular velocity of a satellite in a circular orbit with the radius= R_E. For R_E= 1 Earth radius, $\Omega_m=2\pi/T_m$, with $T_m=84.49\,\text{min}$. It turns out that all terms in the ellipses in eqs. (A34) and (A35) vanish in the limit $\overline{D}=D/R_E\to 0$; so in this limit,

$$\left(\frac{\Omega_{slow}^{in}}{\Omega_m}\right)^2\to 1, \tag{A34′}$$

$$\left(\frac{\Omega_{fast}^{in}}{\Omega_m}\right)^2\to 1+\frac{R_E}{r_{geo}}+\left(\frac{R_E}{r_{geo}}\right)^2\ . \tag{A35′}$$

On the other side, the solutions of the biquadratic equation for the angular frequencies of the out-of-plane modes are found in the form:

$$\left(\frac{\Omega_{slow}^{out}}{\Omega_E}\right)^2=1,\qquad \text{(exact)} \tag{A36}$$

for the slow out-of-plane mode (depicted in fig. A3(c)). For the fast out-of-plane mode (depicted in fig. A3(d)), we find,

$$\left(\frac{\Omega_{fast}^{out}}{\Omega_m}\right)^2 = 1 + \frac{R_E}{r_{geo}} + \left(\frac{R_E}{r_{geo}}\right)^2 (1-\overline{D}) + \left(\frac{R_E}{r_{geo}}\right)^3 (1-\overline{D}^2) + \ldots \tag{A37}$$

It turns out that all terms in the ellipses in eq. (A37) vanish in the limit $\overline{D} = D / R_E \to 0$; so in this limit,

$$\left(\frac{\Omega_{fast}^{out}}{\Omega_m}\right)^2 \to 1 + \frac{R_E}{r_{geo}} + \left(\frac{R_E}{r_{geo}}\right)^2 + \left(\frac{R_E}{r_{geo}}\right)^3 \tag{A37′}$$

The most notable feature of the above results is a separation of time scales. The time periods of both slow modes have time scale $\sim 2\pi / \Omega_E = T_{day} = 1\, \textit{sidereal day}$. In contrast to this, the time periods of both fast modes have time scale $\sim 2\pi / \Omega_m = T_m = 84.49 \min$. Note that,

$$\frac{T_m}{T_E} = \frac{\Omega_E}{\Omega_m} = \left(\frac{R_E}{r_{geo}}\right)^{3/2} = 0.05883\ldots \quad ; \tag{A38}$$

so the separation of time scales emerges due to the smallness of the parameter R_E / r_{geo}, which obviously plays a fundamental role in most of our discussions in this section.

The slow in-plane mode was already discussed in this section within the simplified dumbbell model eq. (A9) yielding its frequency as in eq. (A22). By comparing it with the exact result in eq. (A34), we see that the simplified model captures this frequency correctly to the second order in R_E / r_{geo}. As depicted in fig A3(a), the in-plane slow mode primarily involves the oscillation of the center mass coordinates $\theta_{cm}(t) \approx \theta_M(t)$ and $r_{cm}(t) \approx r_M(t)$ [which are coupled by the conservation law in eq. (A10) effectuating an elliptical orbit of the top seen in fig. A3(a)]. For this mode, the oscillations of $\theta\,(t)$ are much smaller than the oscillations in $\theta_{cm}(t)$ [by a factor $\sim (R_E / r_{geo})^3$], so the bottom appears as suspended from the slowly oscillating top, as depicted in fig. A3(a). In fig. 5 we compared the slow mode frequency from our RSE simulations [see, e.g., figs. 3(a-c)] with our analytic results for dumbbell model. In this figure, we plotted the result in eq. (A34) truncated to the third order in R_E / r_{geo}. [It is virtually indistinguishable, within the thickness of the solid line in fig. 5, from result numerically obtained by solving the biquadratic equation.]. We also note that eq. (A34) can be used to calculate the $\overline{D}_{hopping} = D_{hopping} / R_E$ at which the slow mode frequency vanishes. By truncating the expansion (A35) to the third order in $R_E / r_{geo} = 1/6.6108$ we find $\overline{D}_{hopping} = D_{hopping} / R_E = 0.20003$. On the other hand, by using the biquadratic equation result for the slow mode frequency (which is the exact approach), we find $\overline{D}_{hopping} = D_{hopping} / R_E = 0.20043$. We also note that Eq. (A34) can be iteratively solved to find the $\overline{D}_{hopping} = D_{hopping} / R_E$ for which $\Omega_{slow} \to 0$, with the result having the form of an expansion in powers of the small parameter R_E / r_{geo},

$$\overline{D}_{hopping} = \frac{D_{hopping}}{R_E} = \frac{1}{6} + \frac{7}{36}\frac{R_E}{r_{geo}} + \left(\frac{2}{3}\right)^4 \left(\frac{R_E}{r_{geo}}\right)^2 - \frac{1}{12}\left(\frac{R_E}{r_{geo}}\right)^3 + O\left(\frac{R_E}{r_{geo}}\right)^4 . \tag{A39}$$

For $r_{geo} = 6.6108 R_E$, after truncating the $(R_E / r_{geo})^4$ term, eq. (A39) yields $\overline{D}_{hopping} = D_{hopping} / R_E = 0.20031$, in a very good agreement with the above mentioned exact result $\overline{D}_{hopping} = D_{hopping} / R_E = 0.20043$. Finally, we note that, by eq. (A39), the result in eq. (A24) is exact to the second order in R_E / r_{geo}.

In addition to the above in-plane slow mode, the system exhibits also the out-of-equatorial plane slow mode depicted in fig. A3(c). Its period is exactly 1 day long, as noted in eq. (A37). The origin of this result is in the rotational symmetry of the gravitational potential: tilting (out of plane) system's circular orbit (in the *inertial frame*) produces another orbit solving the equations of motion. In the *geo-synchronous frame*, this tilted orbit is seen as an oscillation about the equatorial plane with the period exactly equal one sidereal day. This mode is best seen by looking at the RSE center of mass R_2 coordinate; see fig. 3(d) from our RSE simulations.

Next, we turn to discuss the two fast modes with frequencies in eqs. (A35) and (A37). These modes are depicted in figs. A3(b) and (d): For these modes, the center of mass and the top are nearly immobile while the bottom executes pendular motion. For the fast in-plane mode, the bottom swings along the equator with the frequency as in eq. (A35). This mode is best seen in the dynamics of the angle $\theta(t)$; see fig. A3(b). For the fast out-of-plane mode, the bottom swings along the north-south axis with the frequency as in eq. (A37). This mode is best seen in the dynamics of the angle $\phi(t)$; see fig. A3(d). By eqs. (A35) and (A37) one can see that these two modes have nearly the same frequency – the difference appears only in the small terms $\sim (R_E / r_{geo})^3$. Moreover, these two frequencies change only little bit (by about -0.23%, for $r_{geo} = 6.6108 R_E$) as *D* changes from *0* to $D_{hopping}$. Thus, to a good approximation, one can well approximate these two frequencies by their values at *D=0* stated in eqs. (A35′) and (A37′). Thus we find for the time periods of the two fast modes,

$$T_{fast}^{out}(D) \approx T_{fast}^{in}(D) \cong T_{fast}^{in}(0) = \frac{T_m}{\sqrt{1 + \frac{R_E}{r_{geo}} + \left(\frac{R_E}{r_{geo}}\right)^2}} \cong 78\,\mathrm{min} \quad . \tag{A40}$$

The above analytic results (for the dumbbell model) are in agreement with our simulations results for the fast modes seen in the RSE dynamics of the angles $\theta(t)$ and $\phi(t)$; see Fig. 4 and the discussions in sec 2. These two angles were indeed found to oscillate with nearly the same time period $\approx 79\,\mathrm{min}$ which does not appreciably change as *D* changes from *0* to $D_{hopping}$.

Thesis summary and discussions

In summary, we have explored classical and statistical mechanics of Rotating Space Elevators which are double rotating floppy strings reaching outer space. Main feature of the RSEs is that objects sliding along the RSE string (sliding climbers) do not require internal engines or propulsion to be transported from the Earth's surface to extraterrestrial locations. Our RSE concept thus solves a major problem in space elevator science which is how to supply energy to the climbers moving along space elevator strings.

RSE’s action generically facilitates truly fundamental physical phenomena -- gravitation and inertial forces. The RSE loopy shape is stabilized by an approximate equilibrium between the gravitational and inertial forces acting in a double rotating frame associated with the RSE. This dynamical equilibrium is achieved by a special form of the RSE mass line density derived in this paper. We have shown that satellites and spaceships carried by sliding climbers can be released (launched) along RSEs. RSE strings can host space stations and research posts. Sliding climbers can be then used to transport useful loads and humans from the Earth to these outer space locations. The RSE exhibits a variety of interesting dynamical phenomena explored here by numerical simulations. Thanks to its special design, the RSE exhibits persistent shape and enduring double rotating motion. Under some conditions however we find that the RSE may undergo a morphological transition to a chaotic state reminiscent of fluctuating directed polymers encountered in the statistical physics of strings and membranes. If untied from the Earth, the RSE may still exhibit persistent shape and enduring double rotating motion while remaining close to the Earth. Under some conditions however we find that the untied RSE may undergo an instability leading it to a state in which it hops well above the Earth surface. With changing untied RSE parameters, the maximum hopping height may be made to diverge, i.e. the untied RSE unbinds from the Earth to infinity, i.e., to interplanetary space.

This is the first study ever to address the RSE concept, hence the model used in our simulations was chosen to be as simple as possible. Thus, the RSE string is modeled as an extensible polymer-like chain of beads connected by stiff Hookean springs (see the Appendix C to Ch.2). So the stretching elasticity was included in our modeling. The model however did not include the elastic resistance to bending, that is, the RSE string was assumed to be floppy. The bending elastic energy is proportional to the square of local string curvature. This energy density cost is known to be small if local radius of curvature is much larger than the local diameter of the string cross-section. This condition is actually realized in the case of the celestial scale RSE, with local radii of curvature comparable to the planet size (see Fig. 1 of Ch. 2) while any sensible scale for the diameter of the string cross-section would be certainly much smaller. Hence the role of bending elastic energy is secondary for elucidating major RSE features (with celestial scale strings). Yet, in future studies, it would be certainly interesting to include bending elasticity effects. For example, the bending elasticity would certainly oppose the RSE morphological narrowing transition and extend the range of the stable RSE double rotating motion in the RSE parameter space. This would be certainly good news for the RSE concept.

We note that the simulation results displayed in this thesis were done with a string model free of any dissipation of mechanical energy. Not discussed in this thesis are our unpublished investigations of a string model with internal friction. This dissipative string model was obtained by generalizing the Hookean spring model discussed in the Appendix C of Ch. 2 to include (in addition to the usual central spring force between adjacent beads) also a central frictional force proportional to relative radial velocity of adjacent beads. Our studies of the internal friction effects were however not extensive. In future studies, it would be certainly interesting to explore these effects more systematically, for example, how they modify the locations of kinetic phase transitions discussed in this thesis.

Also interesting would be to take into account heat production due to aforementioned internal friction, as well as heat diffusion along the RSE and (Stefan-Boltzmann) radiation into surrounding space, in combination with the energy (and momentum) absorbed by RSE from solar radiation. It would be then also interesting to study thermo-mechanical effects such as thermally induced strains along the RSE string. Making a thermo-mechanical finite element model [generalizing our mechanical finite element model of Appendix C to Ch.2] which would include all these interesting effects is conceivable and may be subject of future studies.

We also recall that our modeling did not include the effects of external friction such as air resistance acting more prominently on RSE sections close to its bottom at the Earth surface. There, the RSE speed is fortunately not large yet energy losses would certainly occur and affect the RSE internal rotation. To make up for this, one can apply local external torque acting close to the RSE bottom at the Earth surface. It would be interesting to simulate this compensation scheme by a simple extension of the current modeling which would include air drag forces on lower RSE string sections cutting through the air.

Related to this, we would like to note that the most realistic possible realization of RSE may be on dwarf planets such as the largest asteroid Ceres which has no atmosphere (hence no air resistance). More importantly, Ceres (which has size of Texas) has a relatively small mass and radius hence tensile stress in RSE strings would be much smaller than in the case of the Earth. [This can be verified by applying our analytic results for tensile stress derived in Ch. 2 to the case of, say, elliptic RSE on Ceres.] This is the most desirable feature from the point of view of a future RSE technology which will be limited by finite tensile strength of modern day strong materials such as carbon nanotubes and diamond nano-threads. Additional advantage of the RSE on Ceres (over the RSE on Earth) is that this dwarf planet does not have large natural satellites (moons) which would perturb the RSE motion. An investigation of the RSE perturbations by moons orbiting planets with installed RSEs is left for future studies. Also interesting would be to investigate the effects of nonsphericity of planets. In this respect we note that for weakly nonspherical planets (such as the Earth and Ceres as well) the nonsphericity would manifest itself (in the double rotating frame) as a small perturbation entering the residual acceleration term in Eq. (4) of Ch. 2. Hence the major RSE behavior may not be affected significantly. In addition, the presence of the Sun has been ignored in the present study. This may be a less serious drawback (than ignoring moons) since the gravitational attraction of the Sun on RSE is counteracted by centrifugal force acting in the frame following the planet around the Sun.

We also note that sliding climbers in our simulations move without sliding (kinetic) friction over RSE strings, as if the friction is eliminated, say, by magnetic levitation. Neither did we take into account air drag force on the climber which acts more prominently on RSE sections close to its bottom at the Earth surface. There, the climber speed may not be large (since its velocity approaches zero at turning point) yet energy losses would certainly occur and affect the motion of sliding climbers. Both air resistance and sliding friction can be included into the algorithm discussed in Appendix F, but we did not do it for the purposes of this thesis. Yet, some of the friction effects are easy to infer on analytic grounds even without numerical modeling, and in Ch. 2 we did comment on the motion of sliding climbers in the presence of sliding friction: See the note in Fig. 2 caption (in Ch. 2) and related discussions in the last two paragraphs of the Sec. 2.6 on launching satellites from RSE. In view of those discussions, it may be sometimes favorable to have some sliding friction present, depending on the actual purpose of RSE.

There is a long (if not infinite) list of other effects that may be addressed in future studies. For example, in the case of planets having some significant magnetic fields such as the Earth (but not Mars) it would be interesting to model induction effects of these fields on RSE, especially if the RSE string is made out of a conducting material. In this respect it is worthwhile to note that, among the candidate materials, carbon nanotubes are indeed conducting (metallic or semiconducting) while diamond nano-threads are non-conducting (like diamond, which is one of the best insulators).

Having said this, we would still like to voice our support for continuing further RSE modeling by using the simple modeling approach applied in this study. Indeed, “all inclusive” models that would include all the effects discussed above may easily yield exceedingly slow computer codes. This is a big disadvantage especially if one desires to optimize the RSE by changing its basic geometrical and mechanical parameters discussed in this thesis. For such optimizations, one independently runs in parallel RSE & climbers systems with different parameters on different processors of a computational cluster, and then searches for the best system according to some criterion. Even with our present simple computational model the processing is relatively slow [about one month for 400,000 min RSE time evolution]. With “all inclusive models” one may end up with codes running for years or longer. To make up for this, one may apply parallel algorithms, with communicating processors. This would however reduce the number of simulated RSE systems with different parameters and thus hamper the RSE optimization. In view of this, a simple modeling scheme like the one used in this study may be the most efficient choice for optimization purposes. An example would be a search for a good practical way to give the RSE its initial spin. It may require searching over many different ways (histories) of applying external forces and torques (produced by local rocket propulsions) which would drive RSE loops to open and start rotating.

One may also think of other (than rocket propulsion) ways of deploying RSE. For example, one can attach arrays of electrically charged objects (say, positively charged rubber balls) along two initially parallel straight strings, i.e., two linear space elevators linked at their end points (top and bottom). The electrostatic repulsion between the charged objects will spontaneously initiate (at least modest) RSE loop opening. Next, applying local external torque close to the RSE bottom at the Earth can be used to initiate loop spinning and further loop opening. I and Dr. Golubovic would be excited to pursue modeling of this approach to deploying RSE. Importantly, it should be obvious that the same approach can also be used to "rejuvenate" a narrowed RSE state (discussed in Ch. 2) and turn it back into the double rotating state with opened RSE loop. Complex problem on how to deploy or rejuvenate the RSE is left for future studies that may be done by applying the simple mechanical model used in our study.